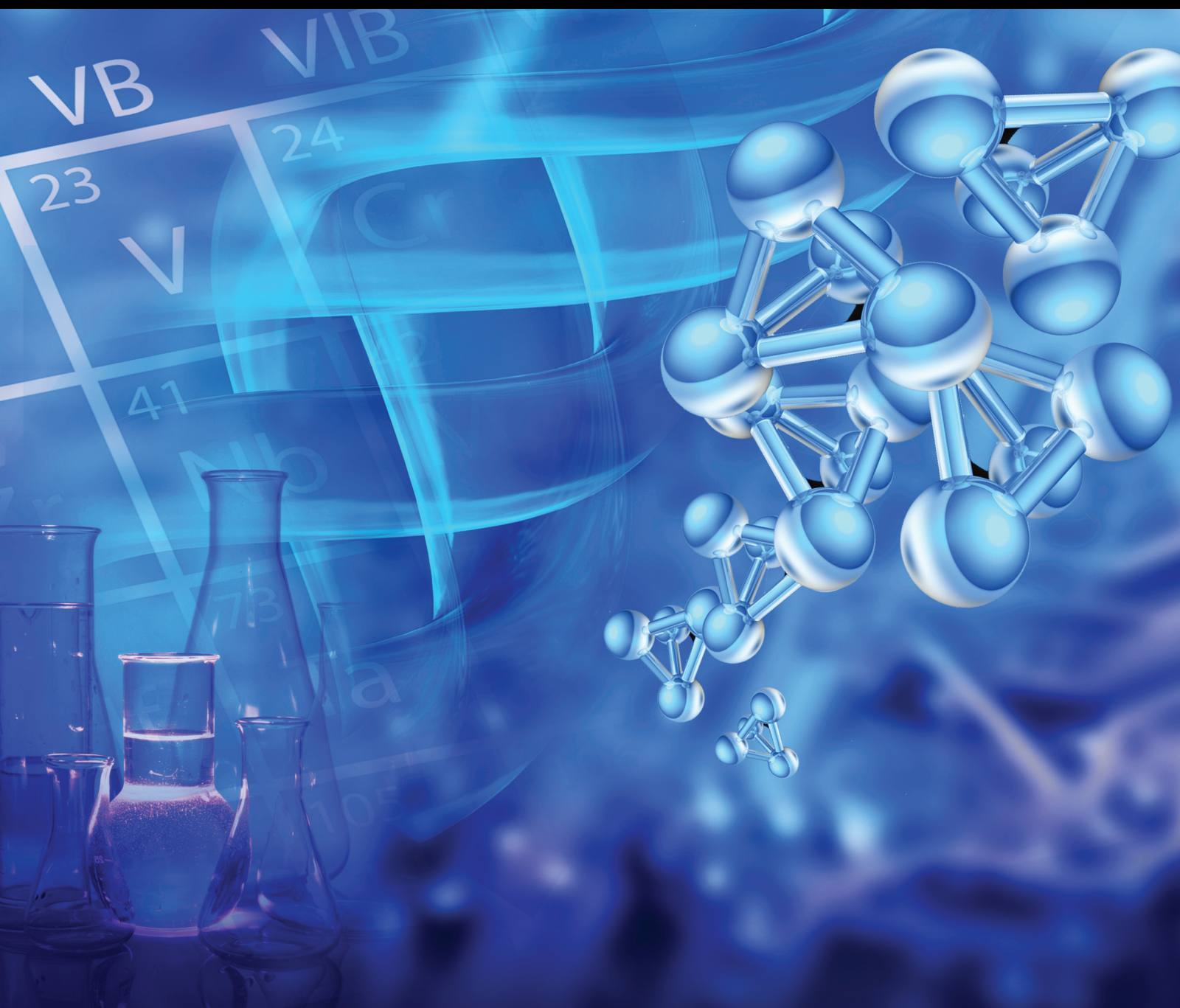


Metals in the Environment: Toxic Metals Removal

Lead Guest Editor: Muataz A. Atieh

Guest Editors: Yun Ji and Viktor Kochkodan





Metals in the Environment: Toxic Metals Removal

Bioinorganic Chemistry and Applications

**Metals in the Environment:
Toxic Metals Removal**

Lead Guest Editor: Muataz A. Atieh

Guest Editors: Yun Ji and Viktor Kochkodan



Copyright © 2017 Hindawi. All rights reserved.

This is a special issue published in "Bioinorganic Chemistry and Applications." All articles are open access articles distributed under the Creative Commons Attribution License, which permits unrestricted use, distribution, and reproduction in any medium, provided the original work is properly cited.

Editorial Board

P. J. Bednarski, Germany
V. Brabec, Czech Republic
Ian S. Butler, Canada
Luigi Casella, Italy
Zhe-Sheng Chen, USA
Francesco P. Fanizzi, Italy
A. Keramidas, Cyprus
C. López, Spain

G. Mendoza-Diaz, Mexico
A. Messerschmidt, Germany
Elena R. Milaeva, Russia
Demetrio Milea, Italy
Virtudes Moreno, Spain
Giovanni Natile, Italy
M. F. Peana, Italy
Spyros P. Perlepes, Greece

Claudio Pettinari, Italy
Enrico Rizzarelli, Italy
J. Sgrignani, Switzerland
Imre Sovago, Hungary
M. Stiborova, Czech Republic
Konstantinos Tsipis, Greece

Contents

Metals in the Environment: Toxic Metals Removal

Muataz A. Atieh, Yun Ji, and Viktor Kochkodan
Volume 2017, Article ID 4309198, 2 pages

Cadmium Removal from Contaminated Water Using Polyelectrolyte-Coated Industrial Waste Fly Ash

Fatai A. Olabemiwo, Bassam S. Tawabini, Faheemuddin Patel, Tajudeen A. Oyehan, Mazen Khaled,
and Tahar Laoui
Volume 2017, Article ID 7298351, 13 pages

Enhanced Adsorption of Selenium Ions from Aqueous Solution Using Iron Oxide Impregnated Carbon Nanotubes

Omer Y. Bakather, Ahmad Kayvani Fard, Ihsanullah, Majeda Khraisheh, Mustafa S. Nasser,
and Muataz Ali Atieh
Volume 2017, Article ID 4323619, 12 pages

A Comparative Study of Raw and Metal Oxide Impregnated Carbon Nanotubes for the Adsorption of Hexavalent Chromium from Aqueous Solution

Muhammad I. Qureshi, Faheemuddin Patel, Nadhir Al-Baghli, Basim Abussaud, Bassam S. Tawabini,
and Tahar Laoui
Volume 2017, Article ID 1624243, 10 pages

Removal of Zinc from Aqueous Solution by Optimized Oil Palm Empty Fruit Bunches Biochar as Low Cost Adsorbent

Seyed Ali Zamani, Robiah Yunus, A. W. Samsuri, M. A. Mohd Salleh, and Bahareh Asady
Volume 2017, Article ID 7914714, 9 pages

Adsorption of Toluene and Paraxylene from Aqueous Solution Using Pure and Iron Oxide Impregnated Carbon Nanotubes: Kinetics and Isotherms Study

Aamir Abbas, Basim Ahmed Abussaud, Ihsanullah, Nadhir A. H. Al-Baghli, and Halim Hamid Redhwi
Volume 2017, Article ID 2853925, 11 pages

Hazardous Effects of Titanium Dioxide Nanoparticles in Ecosystem

Syed Niaz Ali Shah, Zahir Shah, Muzammal Hussain, and Muzaffar Khan
Volume 2017, Article ID 4101735, 12 pages

Editorial

Metals in the Environment: Toxic Metals Removal

Muataz A. Atieh,^{1,2} Yun Ji,³ and Viktor Kochkodan¹

¹*Qatar Environment and Energy Research Institute (QEERI), Hamad Bin Khalifa University (HBKU), Qatar Foundation, Doha, Qatar*

²*College of Science and Engineering, Hamad Bin Khalifa University, Qatar Foundation, P.O. Box 5825, Doha, Qatar*

³*Chemical Engineering Department, College of Engineering & Mines (CEM), University of North Dakota, Grand Forks, ND, USA*

Correspondence should be addressed to Muataz A. Atieh; mhussien@qf.org.qa

Received 19 June 2017; Accepted 19 June 2017; Published 16 July 2017

Copyright © 2017 Muataz A. Atieh et al. This is an open access article distributed under the Creative Commons Attribution License, which permits unrestricted use, distribution, and reproduction in any medium, provided the original work is properly cited.

Faced with more and more stringent environmental regulations, nowadays heavy metals are the priority pollutants of surface and ground waters. Water contamination with these compounds is becoming one of the most serious environmental problems because of the toxic nature of the heavy metal ions, even at low trace levels. With the rapid development of industries such as metal plating facilities, mining operations, tanneries, fertilisers, and paper industries, heavy metals wastewaters are directly or indirectly discharged into the environment increasingly. Unlike organic contaminants, heavy metals are not biodegradable and tend to accumulate in living organisms. Many heavy metal ions, such as mercury, cadmium, lead, nickel, and chromium, are known to be very toxic or carcinogenic. Due to the noxious effects of heavy metals, there are growing public health concerns about environmental pollution with heavy metals. Thus, it is imperative to remove or reduce heavy metal contamination in water in order to prevent or reduce contaminating the environment and the possibility of uptake in the food web. This issue contains original research studies on removal of heavy metals from water by different treatment methods including adsorption, membranes, and coagulation.

The paper by F. A. Olabemiwo et al. investigated the potential ability of raw fly ash (RFA) and polyelectrolyte-coated fly ash (PEFA) to remove cadmium (Cd) from polluted water and described the removal of cadmium (Cd) ions from polluted water using raw fly ash (RFA) and polyelectrolyte-coated fly ash (PEFA). They revealed that a 4.0 g/L dosage of PEFA removed around 99% of 2.0 mg/L of Cd in 15 min at 150 rpm compared to only 27% Cd removal achieved by RFA under the same conditions. A comparative study of

raw and metal oxide impregnated carbon nanotubes for the adsorption of hexavalent chromium from aqueous solution was carried out by M. I. Qureshi et al. They reported the use of raw, iron oxide, and aluminum oxide impregnated carbon nanotubes (CNTs) for the adsorption of hexavalent chromium (Cr(VI)) ions from aqueous solution. They showed that impregnated CNTs achieved significant increase in the removal efficiency of Cr(VI) ions compared to raw CNTs. In fact, both CNTs impregnated with 10% loading of iron and aluminum oxides were able to remove up to 100% of Cr(VI) ions from aqueous solution. While O. Y. Bakather et al. studied the removal of selenium ions from aqueous solution using iron oxide impregnated carbon nanotubes (CNTs). Total removal of 1 ppm Se ions from water was achieved when 25 mg of CNTs impregnated with 20 wt.% of iron oxide nanoparticles is used. Maximum adsorption capacity of the Fe₂O₃ impregnated CNTs, predicted by Langmuir isotherm model, was found to be 111 mg/g. Also using Fe₂O₃ impregnated CNTs have shown an efficient removal of hazardous organic components such as toluene and paraxylene (p-xylene) from aqueous solution as reported by A. Abbas et al. Batch adsorption experiments show that iron oxide impregnated CNTs have higher degree of removal of p-xylene (i.e., 90%) compared with toluene (i.e., 70%), for soaking time 2 h, with pollutant initial concentration of 100 ppm, at pH 6 and shaking speed of 200 rpm at 25°C. This new finding might revolutionize the adsorption treatment process and application by introducing a new type of nanoadsorbent that has super adsorption capacity towards heavy metals ions and organic pollutants from water. In addition, S. N. A. Shah et al. cover the chemical as well as the biological concerns about

nanoparticles (NPs) particularly titanium dioxide (TiO_2) NPs and emphasize the toxicological profile of TiO_2 at the molecular level in both in vitro and in vivo systems. Although nanoparticles (NPs) have made incredible progress in the field of nanotechnology and biomedical research and their applications are demanded throughout industrial world particularly over the past decades, little is known about the fate of nanoparticles in ecosystem. Concerning the biosafety of nanotechnology, nanotoxicity is going to be the second most priority of nanotechnology that needs to be properly addressed.

Another study was carried out by S. A. Zamani et al., to produce optimized biochar from oil palm empty fruit bunches (OPEFB), as a green, low cost adsorbent for uptake of zinc from aqueous solution. High removal of zinc was achieved by this green bioactive carbon material.

We hope that this special issue would shed light on many important aspects related to removal of heavy metals from water and attract attention by the scientific community to pursue further investigations in this field.

Acknowledgments

We would like to express our appreciation to all the authors for their informative contributions and the reviewers for their support and constructive critiques in making this special issue possible.

Muataz A. Atieh
Yun Ji
Viktor Kochkodan

Research Article

Cadmium Removal from Contaminated Water Using Polyelectrolyte-Coated Industrial Waste Fly Ash

Fatai A. Olabemiwo,¹ Bassam S. Tawabini,¹ Faheemuddin Patel,² Tajudeen A. Oyehan,¹ Mazen Khaled,³ and Tahar Laoui²

¹Geosciences Department, College of Petroleum & Geosciences, King Fahd University of Petroleum & Minerals (KFUPM), Dhahran 31261, Saudi Arabia

²Mechanical Engineering Department, KFUPM, Dhahran 31261, Saudi Arabia

³Chemistry Department, KFUPM, Dhahran 31261, Saudi Arabia

Correspondence should be addressed to Bassam S. Tawabini; bassamst@kfupm.edu.sa and Tahar Laoui; laoui@kfupm.edu.sa

Received 13 February 2017; Revised 10 April 2017; Accepted 4 May 2017; Published 7 June 2017

Academic Editor: Viktor Kochkodan

Copyright © 2017 Fatai A. Olabemiwo et al. This is an open access article distributed under the Creative Commons Attribution License, which permits unrestricted use, distribution, and reproduction in any medium, provided the original work is properly cited.

Fly ash (FA) is a major industrial waste generated from power stations that add extra cost for proper disposal. Recent research efforts have consequently focused on developing ways to make use of FA in environmentally sound applications. This study, therefore, investigates the potential ability of raw fly ash (RFA) and polyelectrolyte-coated fly ash (PEFA) to remove cadmium (Cd) from polluted water. Using layer-by-layer approach, functionalized fly ash was coated with 20 layers from 0.03% (v/v) of cationic poly(diallyldimethylammonium chloride) (PDADMAC) and anionic polystyrene sulfonate (PSS) solutions. Both surface morphology and chemical composition of the adsorbent (PEFA) were characterized using Field-Emission Scanning Electron Microscope (FE-SEM), X-Ray Diffraction (XRD), Fourier-Transform Infrared (FTIR), and X-Ray Fluorescence (XRF) techniques. The effects of pH, adsorbent dosage, contact time, initial contaminant concentration, and mixing rate of the adsorption of Cd were also studied in batch mode experiments. Results of the study revealed that a 4.0 g/L dosage of PEFA removed around 99% of 2.0 mg/L of Cd in 15 min at 150 rpm compared to only 27% Cd removal achieved by RFA under the same conditions. Results also showed that adsorption by PEFA followed both Langmuir and Freundlich models with correlation coefficients of 98% and 99%, respectively.

1. Introduction

In today's world, one issue of major concern is water pollution as the quality of water available for consumption greatly affects the health and wellbeing of humans and animals. Factors like industrialization, agricultural activities, urbanization, and population increase among others are likely reasons for water quality depreciation [1, 2]. The constant discharge of different pollutants such as organic compounds and heavy metals into the environment is causing growing concern to the entire world. Unlike most organic contaminants, heavy metals are mainly problematic because they accumulate in the tissues of living organisms and do not biodegrade, thereby leading to countless threats to the ecological environments and wellbeing of humans at large [3]. Majorly known heavy

metals primarily consist of cadmium, chromium, mercury, lead, cobalt, nickel, and so forth; these metallic ions are toxic and pose severe effects on human health.

Cadmium (Cd) which is a deadly heavy metal of work-related and environmental worry has been recognized as a substance that is teratogenic and carcinogenic to human. The allowable limit for Cd in drinking water is set at 3.0 ppb by World Health Organization (WHO) [4]. If ingested beyond the limit, it would affect the kidney or probably damage it. Common ways via which Cd get leached to the environment include industrial processes like smelting, alloy manufacturing, and pesticide and anthropogenic activities such as improper disposal of cigarette, unused paints, fertilizers, and Ni/Cd batteries [5]. Therefore, the removal of this heavy metal from contaminated water has become a task of

paramount importance. For that, numerous methods such as membrane separation, ion exchange, coagulation, softening, solvent extraction, and adsorption have been employed [6]. Some of these techniques are effective but are not widely applicable to different pollutants and also generate chemical waste. Application of these techniques relies on cadmium concentration and associated costs [7]. Mahvi & Bazrafshan (2007) applied electrocoagulation to remediate cadmium using Al electrode. Simulated wastewater of different concentrations of cadmium was filled in a tank and their removal was measured at different pH (3, 7, and 10) and at electric potential range of 20, 30, and 40 volts. Their investigation showed that initial pH was lower than the final pH value [8]. Numerous studies have used the adsorption mechanism for heavy metals removal using activated carbon owing to its very good adsorption features but with comparatively high operating cost [9, 10]. Therefore, the need to develop low-cost adsorbents for heavy metals removal from aqueous solution has greatly increased. Adsorbents such as *Setaria* grass [11], sawdust [12], zeolite [13], clay [9], biomass [14, 15], and fly ash [6, 16–19] have been used.

Fly ash (FA) is one of the major wastes from power stations that cannot be cheaply disposed of. Recent research efforts have consequently focused on developing ways to make use of FA in applications that are friendly to the environment. Apart from its limited applications in cement and concrete industries, fly ash alternative use/reuse in environmental study takes advantage of its reasonable adsorptive property for some water pollutants. Al-Khalidi et al. conducted a comparative study on Cd adsorption using activated carbon, CNT, CNF, and fly ash. They found out that, at pH 7 in 120 min with 50 mg and 150 rpm, percent removal of 95, 27, 34, and 38% was attained for fly ash, CNT, CNF, and activated carbon, respectively [7]. However, the efficiency of the FA for removing water pollutants was limited in a few previous studies and, therefore, there is a need to improve its adsorption efficiency [18]. One way to achieve this objective could be to coat the surface with polyelectrolytes which enhanced the adsorptive capacity of several adsorbent materials [18]. Literature search showed that no work has been conducted to assess the efficiency of FA to remove Cd from water after being coated with layers of polyelectrolytes which is the main aim of this work. As fly ash is cheaper compared to other adsorbent materials, any improvement in the efficiency of polyelectrolyte-coated fly ash in the removal of heavy metal ions from water gives it an advantage over other adsorbent materials.

Polyelectrolytes are charged organic polymers, which are soluble in water and are formed from monomers of different kinds. These polymers could be cationic or anionic depending on the functional ionic group. They are used in many applications such as water purification and paper production [20]. Examples of polyelectrolytes include poly(diallyldimethylammonium chloride) (PDADMAC), polystyrene sulfonate (PSS), and polyethylenimine (PEI). Studies had been made to modify adsorbents with polyelectrolytes. Zhang et al. [21] modified multiwalled CNT with PDADMAC for chromium adsorption of which 32% removal was achieved at pH 6. Huang et al. [22] successfully applied silica-coated Fe_3O_4

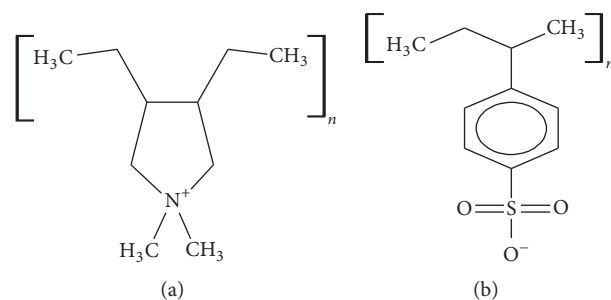


FIGURE 1: Chemical structures of (a) poly(diallyldimethylammonium chloride) (PDADMAC) and (b) polystyrene sulfonate (PSS).

functionalized with *c*-mercaptopropyltrimethoxysilane for extraction of Cu^{2+} , Hg^{2+} , Cd^{2+} , and Pb^{2+} in a varied pH range and even in the presence of foreign ions acting as interferences such as Al^{3+} , Fe^{3+} , and Cl^- . Stanton et al. [23] showed that alternating polyelectrolyte deposition on porous supports can yield nanofiltration membranes allowing high water flux along with selective ion transport by using pairs of poly(styrene sulfonate)/poly(allylamine hydrochloride) on porous alumina.

The aim of this study is to explore the potential efficiency of fly ash to remove Cd ions from contaminated water and to evaluate the effect of acid treatment and polyelectrolyte coating of fly ash on removal efficiency. Moreover, the effects of experimental parameters such as adsorbent dose, contact time, pH, mixing rate, initial concentration, and temperature on the Cd ion removal efficiency were also deduced. Thermodynamic parameters like enthalpy, entropy, and Gibbs free energy were also investigated. The acid treatment of fly ash was done using HNO_3 and the polyelectrolyte coating of fly ash is done by layer-by-layer (LBL) deposition of two electrolytes, namely, PDADMAC and PSS, solutions on acid-treated fly ash (AFA). The Cd ion removal efficiency of adsorbents was measured using batch adsorption experiments. The sorption kinetics of Cd on the adsorbents were investigated using Langmuir and Freundlich isotherm models. Figure 1 shows the chemical structures of PSS and PDADMAC.

2. Materials and Methods

2.1. Chemicals/Stock Solution. All chemicals and solvents used were of analytical grade. PDADMAC (Mw: 200,000–350,000 kg/mol.) and PSS (Mw: 70,000 kg/mol.) were commercially acquired and used. Deionized (DI) water was generated in real time from Milli-Q Ultrapure water system (Millipore). Working standard solutions were prepared from stock Cadmium ICP Standard Solution supplied by ULTRA Scientific (USA) by serial progressive dilutions with deionized water. The prepared solutions were stirred for 30 mins with a magnetic stirrer to ensure homogeneity. The pH of the solutions was adjusted using either 0.1 M HNO_3 or 0.1 M NaOH solution. Buffer solutions were added as required in order to keep constant pH during the experiment.

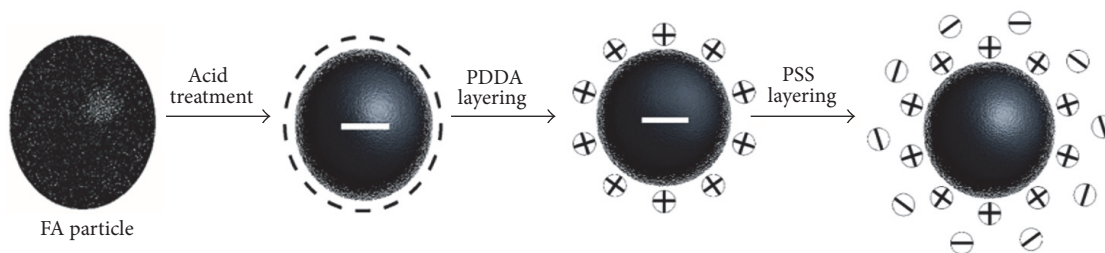


FIGURE 2: Schematic illustration of acid treatment and polyelectrolytes coating of fly ash (FA).

2.2. Adsorbent Preparation. The fly ash used in this study was obtained from a local power plant in the Eastern Province of Saudi Arabia. In this plant, raw fly ash is generated from the combustion of heavy liquid fuel and collected by electrostatic precipitation technique. This raw fly ash (RFA) was processed further to produce acid-treated fly ash (AFA) and polyelectrolyte-coated fly ash (PEFA).

2.2.1. Acid Treatment of Fly Ash. 150 g of fly ash materials was soaked in 1000 mL DI water and stirred for 2 h. After stirring, the mixture was allowed to settle for 10 min before the water was decanted and the procedure was repeated 3 times which gives a slurry phase, which was subsequently dried in the oven at 80°C temperature for 12 h and stored until used for the batch treatment experiments. 100 g of washed fly ash was soaked in 300 mL of 1 M HNO₃. The mixture was refluxed at 110°C temperature for 24 h. The acid was allowed to evaporate at 60°C, after which the reaction mixture was diluted with 500 mL DI water until the pH of the filtrate becomes neutral. The residue was then dried in the oven at 105°C for 72 h [24–29].

2.2.2. Layer-by-Layer Deposition (Polyelectrolyte Coating of Fly Ash). Polyelectrolyte coating of fly ash (PEFA) was prepared by coating the acid-treated fly ash (AFA) with polyelectrolyte (PE) using modified procedure of layer-by-layer method described by Li et al. [30]. Succinctly, the solutions used were prepared by dissolving 3 mL of poly(diallyldimethylammonium chloride) (PDADMAC) or polystyrene sulfonate (PSS) in 1000 mL of water; the solutions were stirred with a stirrer to ensure a homogenous mixture. The layering then followed Li et al.'s [30] procedure but without the addition of NaCl to ensure the formation of thinly coated PE layers as illustrated in Figure 2. The procedure was repeated until the desired number of layers was attained, that is (PDADMAC/PSS-FA)_n, where *n* could be 1, 2, 3, 4, 5, . . . , 20.

2.3. Characterization of FA Adsorbents. Characterization of adsorbents (RFA, AFA, and PEFA) surface morphology was conducted to understand elemental, mineralogical, and functional group composition. Scanning electron microscopy (SEM) micrographs were documented using FESEM (JSM-5900LV) fitted with an energy disperse X-ray spectroscopy (EDX) detector model X-max. Functional groups were determined using a Perkin-Elmer 16 FPC FTIR spectrometer with

the aid of KBr pellets and spectra were generated in the region of 600–4000 cm⁻¹ wavenumber. Thermogravimetric analysis (TGA) was carried out using thermal analyzer (STA 449 F3 Jupiter) by Netzsch, Germany. The analysis was conducted in air at a distinct temperature ramped at 10°C per min to 900°C [6]. Phase analysis of the adsorbents was evaluated using D8 ADVANCE X-ray Diffractometer manufactured by BRUKER (Germany).

2.4. Batch Adsorption Studies. Batch mode adsorption studies were conducted at room temperature in 100 mL Erlenmeyer flasks covered with aluminum foil to avoid contamination. Effects of pH, contact time, adsorbent dosage, mixing rate, initial concentration, and temperature were investigated. Analysis of initial and final concentration of Cd ions was conducted using Optima 8000® ICP-OES Spectrometer (Perkin-Elmer, USA). The percent removal, as well as adsorption capacity of metal ions, was calculated with the following equations:

$$\% \text{ removal} = \frac{C_i - C_e}{C_i} \times 100 \quad (1)$$

$$\text{adsorption capacity, } q_e \text{ (mg/g)} = \frac{C_i - C_e}{M_s} \times V,$$

where *C_i* is the metal ion initial concentration in solution (mg/L), *C_e* is the final concentration of adsorbate ion in solution (mg/L), *V* is the total volume of solution (L), and *M_s* is adsorbent dosage.

Mean values of 5 replicates were used for data analysis to ensure reproducibility; relative standard deviation (RSD) was in the range of ±3–5%. The precision of the standard solution for analysis was better than 3%.

2.5. Adsorption Isotherm Model. The descriptions of adsorption behaviors are usually provided by mathematical models known as the adsorption isotherm models [6]. The distribution of adsorbate molecules between the liquid phase and a solid phase at equilibrium state can be indicated by the adsorption isotherm [25]. In this study, Langmuir and Freundlich isotherm models were employed to assess the adsorption behavior of polyelectrolyte-coated fly ash (PEFA) for Cd ion removal in an aqueous medium. Langmuir isotherm model explains the monolayer adsorption, suggesting that adsorbent materials have finite capacity, considered as the equilibrium state beyond which no further adsorption

takes place [31]. The existence of specific homogeneous sites within the adsorbent at which adsorption occurs is the main assumption of this model. The Freundlich isotherm model also explains the adsorptive behavior of the adsorbent material. Adsorption on a heterogeneous surface with the interaction between adsorbate molecules is the main application of this model. The Langmuir and Freundlich isotherms are expressed by the following equation:

$$Q_e = \frac{Q_{\max} K_L C_e}{1 + K_L C_e} \quad (2)$$

The above equation can be linearized to

$$\frac{1}{Q_e} = \frac{1}{Q_{\max} K_L C_e} + \frac{1}{Q_{\max}} \quad (3)$$

From (2), C_e is the equilibrium of Cd concentration (mg/L); Q_e is the amount of Cd (mg) adsorbed per gram of the adsorbent at equilibrium (mg/g); Q_{\max} is the theoretical maximum adsorption capacity (mg/g); and K_L is the Langmuir isotherm constant (L/mg). A linear plot of $1/Q_e$ versus $1/C_e$ can be used to obtain the values of Q_{\max} and K_L from slope and intercept, respectively.

$$Q_e = K_f C_e^{1/n} \quad (4)$$

The above equation can be linearized to

$$\ln Q_e = \ln K_f + \frac{1}{n} \ln C_e \quad (5)$$

From the equation above, K_f is the Freundlich adsorption constant related to the adsorption capacity [(mg/g) (L/mg)], while the remaining parameters (Q_e and C_e) were described above. A linear plot of $\ln Q_e$ versus $\ln C_e$ can be used to obtain the values of K_f and n from intercept and slope, respectively.

2.6. Kinetic Modelling Studies. The adsorption of Cd (II) was analyzed using different kinetic models like pseudo-first-order model, pseudo-second-order model, and Weber intraparticle diffusion expressed in the following equations:

$$\log \frac{(q_e - q_t)}{q_e} = \frac{-K_L t}{2.303} \quad (6)$$

$$\frac{1}{(q_e - q_t)} = \frac{1}{q_e + Kt} \quad (7)$$

$$\frac{t}{q_t} = \frac{1}{(2K_s q_e^2)} + \frac{t}{q_e} \quad (8)$$

$$q_t = K_{id} t^{1/2} + C \quad (9)$$

In the equations above, q_e and q_t are amounts of Cd adsorbed (mg/g) at equilibrium and at a given time, t (min), respectively. K_L is the pseudo-first-order rate constant sorption (min^{-1}). K_s and K are pseudo-second-order and second-order adsorption rate constants ($\text{g}\cdot\text{mg}^{-1}\cdot\text{min}^{-1}$). K_{id} , $t^{1/2}$, and C are intraparticle diffusion rate constant ($\text{mg}/\text{g}\cdot\text{min}^{-1}$),

square root of time ($\text{min}^{1/2}$), and intercept, respectively. The constants (K_L , K_s , and K) can be determined from the slopes of linear plots of $\log(q_e - q_t)$ against t , t/q_t against t , and $1/(q_e - q_t)$ against t , where q_e can be determined from the intercept data of pseudo-second-order and second-order rate equations.

3. Results and Discussions

3.1. Material Characterization

3.1.1. Surface Morphology. Surface morphology of raw fly ash (RFA), acid-treated FA (AFA), and polyelectrolyte-coated FA (PEFA) was examined with the aid of Field-Emission Scanning Electron Microscopy (FESEM) and energy disperse X-ray spectrometry (EDX). The surface morphologies of the RFA, AFA, and PEFA are presented in Figures 3, 4, and 5, respectively.

Figure 3(a) shows that the RFA has sizes that range from 50 to 500 microns. Elemental composition revealed by EDX spectra in Figure 3(b) shows that carbon (C) has 72%, oxygen has 16.6%, and the remaining elements, silicon (Si), copper (Cu), vanadium (V), aluminium (Al), and sulphur (S), were found to have 0.2, 6.0, 0.7, 2.0, and 2.8% composition, respectively.

When RFA was treated with nitric acid (HNO_3), most of the heavy metals impurities present in the as-received raw fly ash were removed as shown in the EDX spectrum in Figure 4(b). Moreover, it was observed that more pores were visible as a result of the treatment with nitric acid as shown in Figure 4(a) compared to raw fly ash shown in Figure 3(a). The spectrum in Figure 4(b) reveals that the carbon content increased from 72 to 92% and also reveals an increase in the silicon content from 0.2 to 0.4.

Figure 5(a) shows the morphology of polyelectrolyte-coated fly ash (PEFA) along with its elemental composition in Figure 5(b). The SEM image shows that a thin pore linen was coated with PDADMAC-PSS and the EDX spectrum shows an increase in the sulphur content (2.77–5.03%) of the fly ash upon coating with polyelectrolyte which might be due to the component of the polymer that has a polystyrene sulfonate compound (i.e., PSS) in its composition.

3.1.2. Elemental Analysis by X-Ray Fluorescence (XRF) Analysis. XRF analysis was carried out to determine the actual elemental composition of the RFA, AFA, and PEFA adsorbents. The results, as summarised in Table 1, identified the presence of some trace metals like vanadium, manganese, iron, nickel, zinc, and molybdenum with their percentage compositions. It was observed that RFA has no silicon content but has high sulphur content of 51% composition which could be attributed to the fact that the fly ash used in this study is an oil fly ash, received from local power plants operating on liquid fuel. This type of fly ash is usually characterized by low silicon and aluminium contents [32, 33]. As could be inferred from the EDX spectrum, the fly ash has a high carbonaceous content which is not commonly found at that rate in coal fly ash with high silicon and aluminium contents [32, 34]. After treatment with acid (AFA), the fly ash trace metal content was

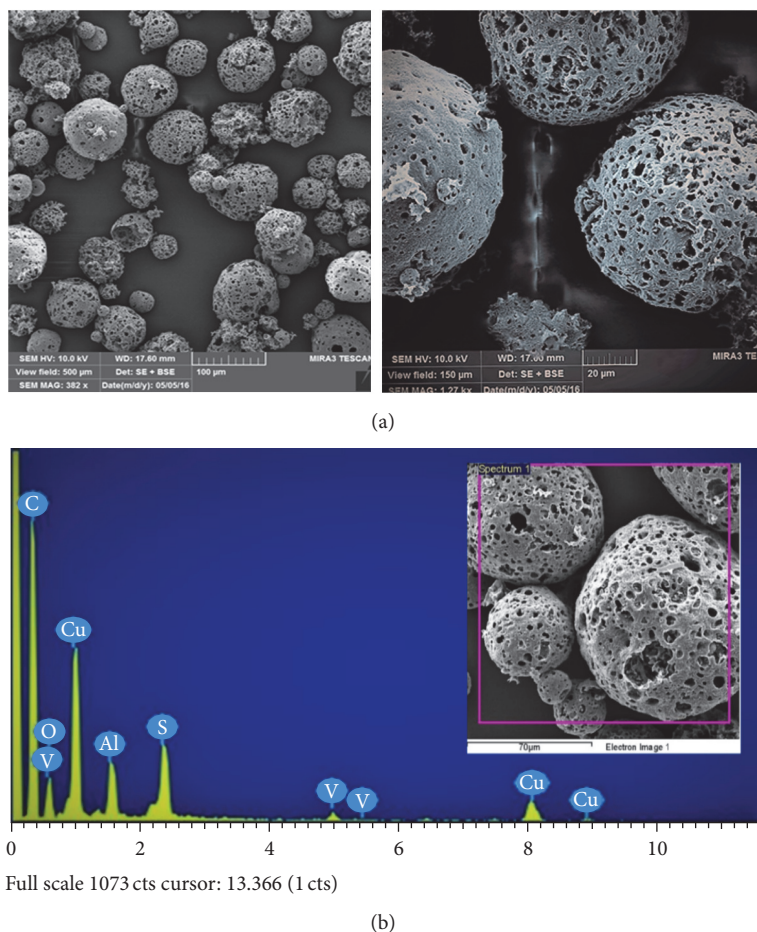


FIGURE 3: Raw FA (a) SEM micrographs (view field: 500 and 150 μm; voltage: 10 kV; resolution: 382x and 1.27 kx); (b) EDX spectrum.

reduced to a nonsignificant value, whereas sulphur content increased from 51% to 86% as shown in Table 1. In PEFA, trace metals were either absent or not present in detectable quantity but sulphur content increased to 92.5% which might be a result of additional sulphate group present in the polymer used for coating.

3.1.3. FTIR (Fourier-Transform Infrared) Spectroscopy Analysis. FTIR technique was used to ascertain the functional groups present in RFA, AFA, and PEFA surface. The samples were scanned from 500 to 4000 cm^{-1} and the intensity of peaks in the IR spectra was observed. Figure 6 shows FTIR spectra for RFA, AFA, and PEFA. The raw fly ash shows a mildly prominent peak at 604 cm^{-1} as a result of the naturally occurring C-S bond [35]. There was a prominent peak at 1367 cm^{-1} as a result of skeletal vibration of a C-C bond [26]. A peak was observed at 1628 cm^{-1} , which indicates the presence of C=C functional group of an alkene [28, 36]. A sharp peak at 1711 cm^{-1} represents C=O in ester group as noted by Shawabkeh et al. [27]. A broad trough was observed at 3436 cm^{-1} as a result of O-H stretching of alcoholic groups [27, 37]. However, after treatment with an acid (HNO_3), peaks were only seen at lower and higher region of the spectra; this might be a result of the bond breaking due to reactions

TABLE 1: Elemental composition of RFA, AFA, and PEFA as revealed by XRF.

Atomic number	Elements	RFA	AFA	PEFA
14	Silicon (Si)	0	0.76	0.00
15	Phosphorus (P)	1.09	0.66	1.18
16	Sulphur (S)	51.44	86.25	92.50
20	Calcium (Ca)	1.91	2.16	2.23
23	Vanadium (V)	20.22	5.10	1.09
25	Manganese (Mn)	0.1	0.00	0.00
26	Iron (Fe)	11.34	2.10	1.29
28	Nickel (Ni)	13.46	2.95	1.70
30	Zinc (Zn)	0.42	0.00	0.00
42	Molybdenum (Mo)	0.02	0.006	0.005
	Loss on Ignition (LOI)	0.009	0.014	0.005
	<i>Total</i>	<i>100</i>	<i>100</i>	<i>100</i>

between the acid and fly ash particles. After coating the AFA with polyelectrolytes (PDADMAC and PSS), a more prominent and sharp peak was observed at 607 cm^{-1} of PEFA which is evident of the presence of more C-S functional groups. The peak of C=C reappeared at 1635 cm^{-1} [29,

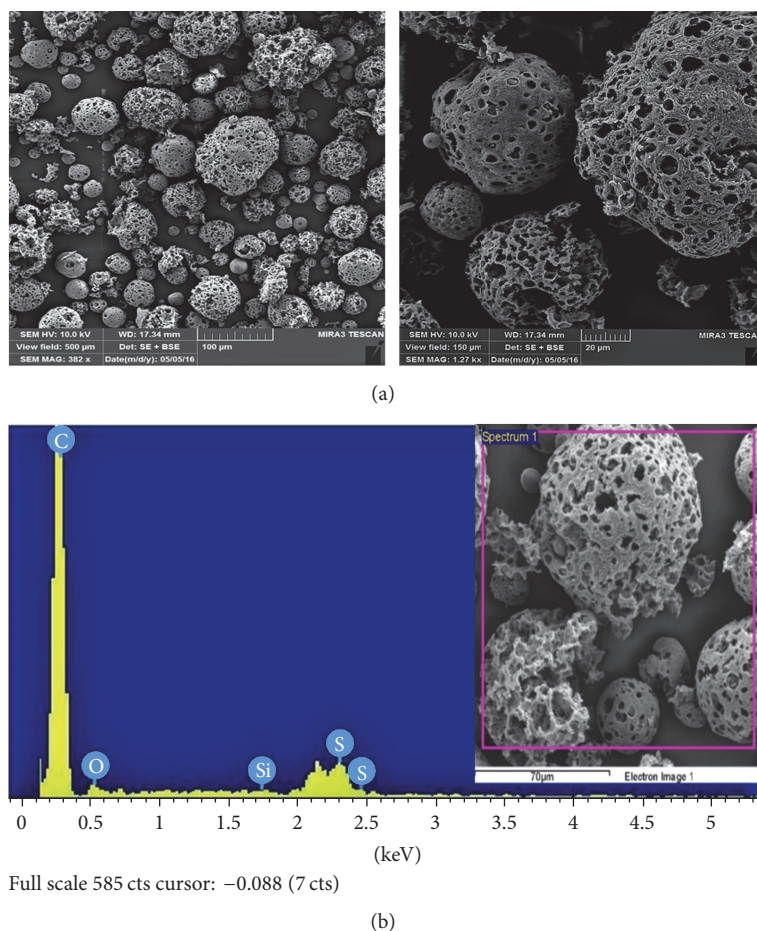


FIGURE 4: Acid-treated FA (a) SEM micrographs (view field: 500 and 150 μm ; voltage: 10 kV; resolution: 382x and 1.27 kx); (b) EDX spectrum.

38]. Additionally, there was C-N peak at 2386 cm^{-1} , which indicates the presence of the polyelectrolytes PDADAMAC on the fly ash [39, 40]. The peaks observed at 3442 and 3451 cm^{-1} of the RFA and AFA spectra, respectively, were also observed at 3454 cm^{-1} in PEFA indicating the presence of carboxylic acid O-H functional groups.

3.1.4. Phase Identification by X-Ray Diffraction (XRD). The mineralogical compositions of RFA, AFA, and PEFA were studied using X-ray diffractometer. Overall, the XRD spectra shown in Figure 7 show the presence of carbon, sulphur, α -quartz (low quartz content), β -quartz (high quartz content), and cristobalite. A prominent peak was observed at $21.6^\circ 2\theta$; this confirms the presence of highly concentrated carbon. The amorphous phase between 22° and $28^\circ 2\theta$ contains sulphur and quartz, respectively. A small peak of cristobalite at $31.4^\circ 2\theta$ was observed. Carbon was very prominent through the prepared adsorbents (RFA, AFA, and PEFA). One significant observation was the presence of β -quartz at $27.4^\circ 2\theta$ in both AFA and PEFA, respectively. No significant peaks were observed after $40^\circ 2\theta$, indicating the presence of amorphous carbon. The XRD pattern of this material can be attributed to that of carbon black or oil fly ash which are both amorphous. Also, the crystalline structure of oil fly ash is known to consist

of carbon and metallic sulphur in the amorphous state [41]. Hence, the fly ash used to prepare PEFA in this study can be referred to as oil fly ash as confirmed from the XRD spectrum.

3.1.5. Thermogravimetric Analysis (TGA). Thermogravimetric analysis was performed to measure the thermal stability and purity of adsorbents. Figure 8 displays the thermograms of RFA, AFA, and PEFA. All samples analyzed exhibit similar curves and do not contain adsorbed water. Due to volatilization/decomposition of organic or inorganic substances, a 2% weight loss was observed between 100 and 470°C in RFA. Dramatic weight losses of 84% for RFA between 470 and 600°C , 80% for AFA at temperature range of 580 – 630°C , and 97% for PEFA between 580 and 670°C can be attributed to the phenomenon of gas generation (CO_2 and CO) upon pyrolysis [42]. Among the three adsorbents, AFA seems to be more thermally stable than the rest with a residual of approximately 5%. Other samples burn off almost completely before the maximum set temperature of 900°C .

3.2. Removal of Cadmium

3.2.1. Effect of pH. Generally, metal adsorption consists of a multifaceted mechanism of ion exchange, metal chelating

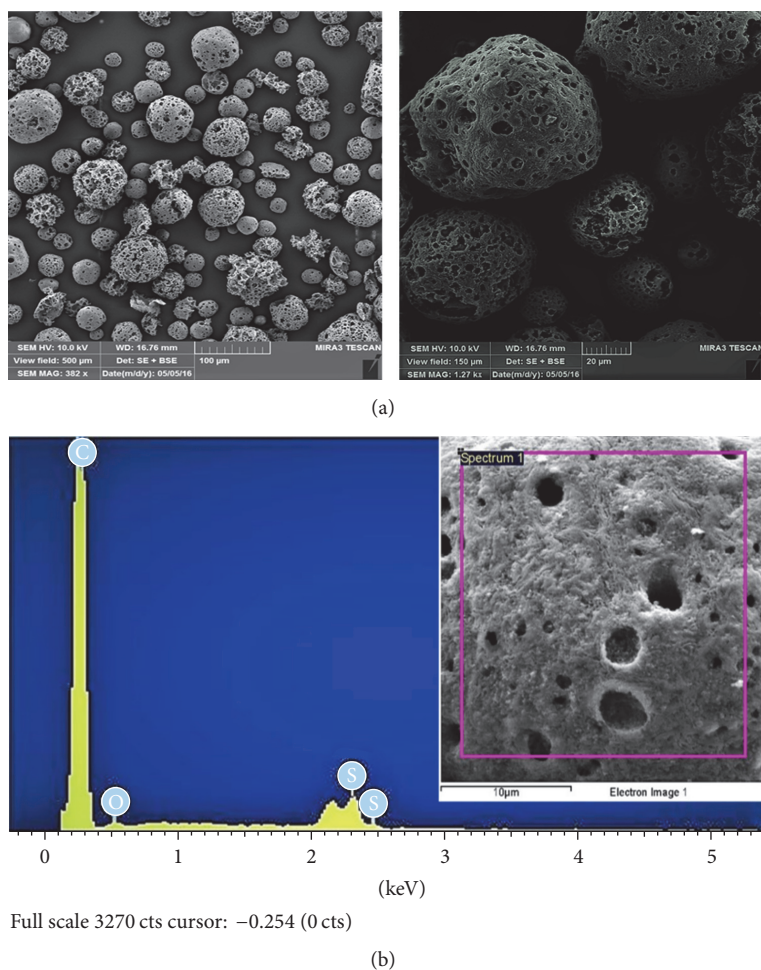


FIGURE 5: Polyelectrolyte-coated FA (a) SEM micrographs (view field: 500 and 150 μm ; voltage: 10 kV; resolution: 382x and 1.27 kx); (b) EDX spectrum.

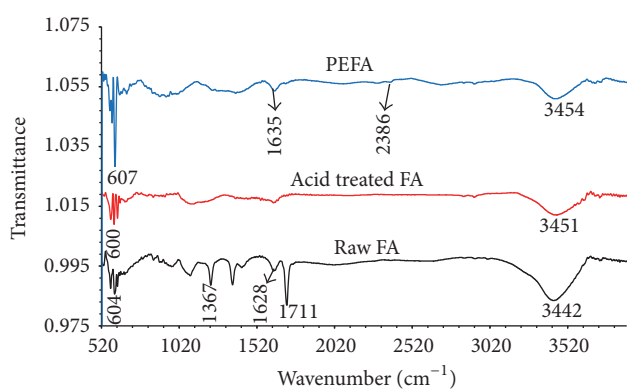


FIGURE 6: IR spectra of RFA, AFA, and PEFA.

with numerous anionic functional groups, physical forces sorption, and trapping of ions in the interior sphere of adsorbents architectural network [9]. Different forms of Cd species occur in deionized water as Cd^{2+} , $\text{Cd}(\text{OH})_{2(s)}$, and $\text{Cd}(\text{OH})^+$ [43]. pH was a leading factor affecting Cd (II)

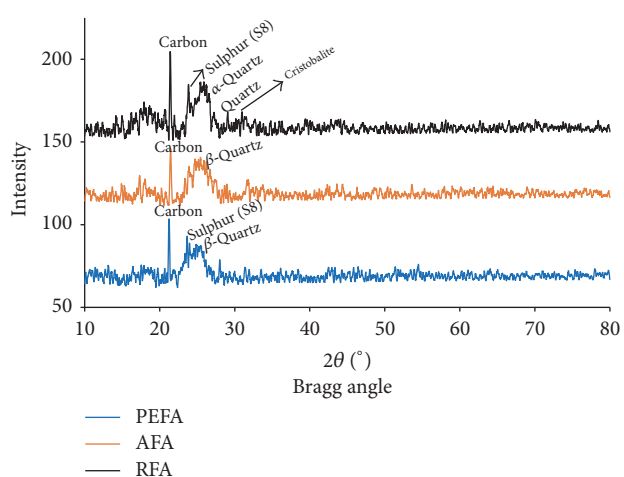


FIGURE 7: XRD spectra of RFA, AFA, and PEFA.

ion removal under the investigated conditions. Nonetheless, Cd^{2+} often exists as a complex $[\text{Cd}(\text{H}_2\text{O})_6]^{2+}$ at low pH and also as prevailing species [44]. With a specific focus on PEFA,

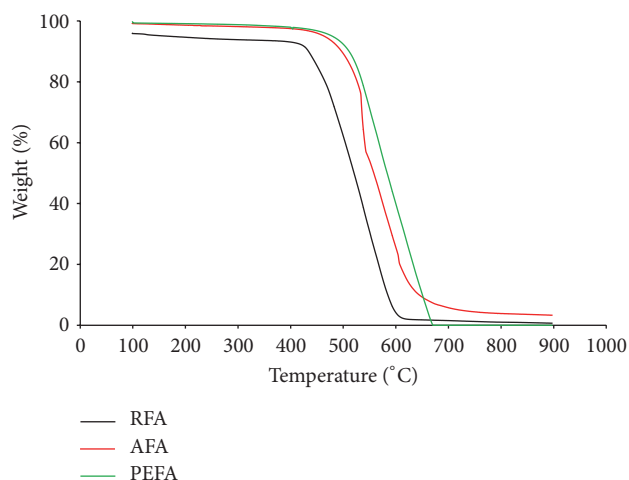


FIGURE 8: Thermogravimetric (TG) measurements of RFA, AFA, and PEFA.

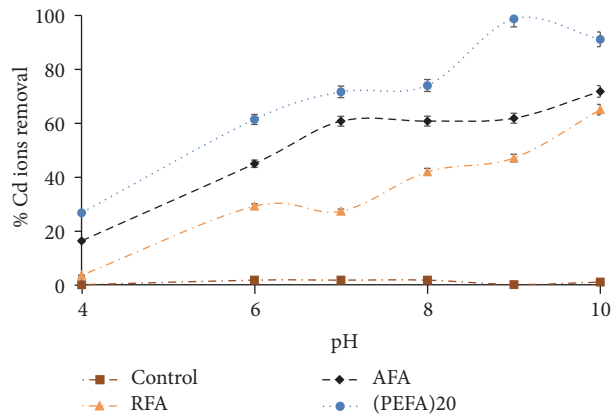


FIGURE 9: The influence of pH on the removal efficiency of Cd (II) ions on FA based adsorbents (RFA, AFA, and PEFA) as a function of 2 mg/L metal ion concentration, 4 g/L adsorbent dosage, 50 mL volume of aqueous solution, mixing rate of 150 rpm, 15 min contact time, and 298 K temperature.

the adsorption of Cd (II) ions by RFA, AFA, and PEFA was investigated at pH 4–10 to fix the optimum pH removal. Figure 9 illustrates an increase in Cd (II) removal efficiency with increased pH in aqueous solution with other parameters fixed at 2 mg/L of metal ion concentration, 4 g/L of adsorbent dosage, 50 mL volume of aqueous solution, mixing rate of 150 rpm, contact time of 15 min, and temperature of 298 K. Maximum sorption of Cd ion was attained at pH 9 due to the fact that in acidic medium Cd (II) ion sorption is low as a result of available large number of hydrogen ions (H^+) which outcompete Cd ions for active sites. However, as the pH increases, the number of positively charged ions available for active sites reduces with a rise in negatively charged ion for binding [38]. Moreover, the sudden increase and decrease in the removal efficiency as observed in Figure 9 suggest an elaborate process of exchanging ions, sorption driven by physical forces, metal chelation, and trapping of

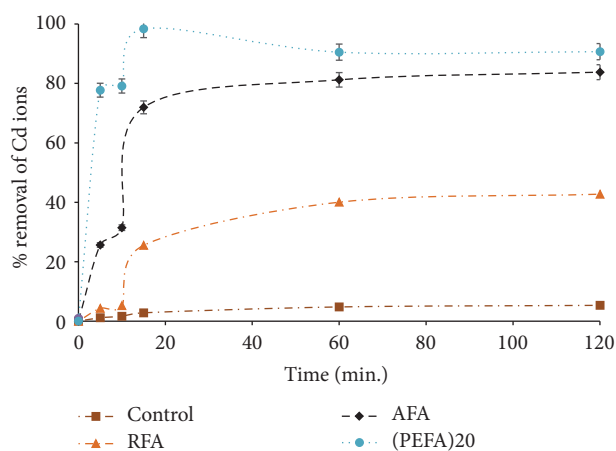


FIGURE 10: The influence of contact time on the removal efficiency of Cd (II) ions on FA based adsorbents (RFA, AFA, and PEFA) as a function of pH value of 9, 2 mg/L metal ion concentration, 4 g/L adsorbent dosage, mixing rate of 150 rpm, 50 mL volume of aqueous solution, and 298 K temperature.

ions in the internal sphere of the structural arrangement of the adsorbents [45].

3.2.2. Effect of Contact Time. Contact time is the time required for equilibrium to be attained in the process of adsorption when no substantial variations are detected in adsorptive concentration after a definite period of time [38]. It hinges on the surface features of the adsorbent in question. To find the optimum contact time for Cd (II) ions uptake, varying contact times from 5 min to 2 h were studied from aqueous solutions of 2 mg/L Cd (II) ions concentration, adsorbent mass of 4 g/L, pH value of 9, mixing rate of 150 rpm, and 298 K temperature. The results obtained indicated that at first there was rapid adsorption of Cd (II) ions for PEFA with 98% removal and a gradual decrease to attain equilibrium in 2 h as shown in Figure 10. Initial fast adsorption for this adsorbent might be a result of rich active sites on the adsorbent surface which become filled up with increasing time and turn out to be saturated [9, 38, 46]. Moreover, the decline in the removal efficiency could be attributed to the presence of metal impurities (V, Mn, Fe, Ni, Mo, and Zn) as revealed by XRF in Table 1, which might have occupied the active site needed for sorption. For this study, optimum contact time was chosen to be 15 min as maximum Cd ions removal was reached at this time. Percent removal for RFA and AFA was 25 and 72%, respectively, at the chosen optimum contact time.

3.2.3. Effect of Adsorbent Dosage. The mass of adsorbent has an effect on the active site available for binding of Cd (II) ions in aqueous solution [25, 46]. In this study, batch mode experiments were conducted by applying varying quantities of RFA, AFA, and PEFA from 1 to 6 g/L at pH value of 9, 2 mg/L metal ion concentration, 150 rpm mixing rate, 15 min contact time, 50 mL volume aqueous solution, and 298 K temperature. As illustrated in Figure 11, Cd (II) ion

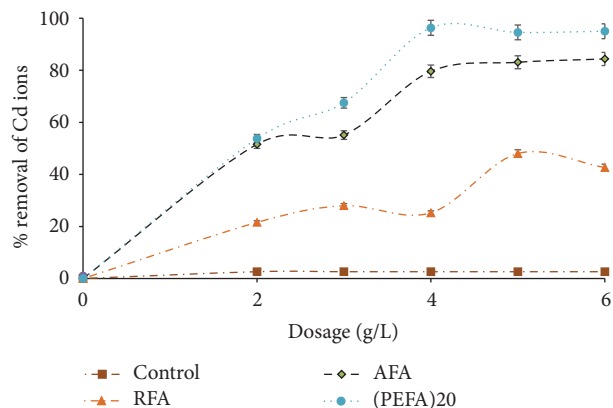


FIGURE 11: The influence of Adsorbent dose on the removal efficiency of Cd (II) ions on FA based adsorbents (RFA, AFA, and PEFA) as a function of pH value of 9, 2 mg/L metal ion concentration, 15 min contact time, mixing rate of 150 rpm, 50 mL volume of aqueous solution, and 298 K temperature.

sorption rises with an increase in dose of adsorbents up till 4 g/L and there was little or no significant adsorption for remaining dosage. Sorption increase with an increase in dose of adsorbent could be attributed to surface area increase, the rise in the exchange site ability of the ion, and an increase in active sites [18, 19, 38, 47]. PEFA reaches optimum at 4 g/L unlike RFA and AFA with 5 g/L and 6 g/L as well as removal efficiency of 48 and 84%, respectively. Incomplete adsorbent aggregation which leads to a decline in Cd ion uptake active surface area may be the reason for the drop in removal efficiency at higher concentration for RFA. 4 g/L adsorbent dose was used for other investigations.

3.2.4. Effect of Mixing Rate. The mixing rate ensures that Cd (II) ions are transferred to the active sites by supporting the contact between Cd ions in aqueous solution and adsorbent binding sites [47]. The optimum removal of Cd (II) at pH value of 9 was used to investigate the effect of mixing rate on the adsorption of Cd (II) ion for RFA, AFA, and PEFA. Figure 12 indicates that the removal of Cd ion increases with mixing rate increase from 50 to 150 rpm. Maximum removal of over 96% was achieved for PEFA, 77% for AFA, and 27% for RFA at 150 rpm with 2 mg/L metal ion concentration, 50 mL volume of aqueous solution, 4 g/L dose of adsorbents, pH value of 9, contact time of 15 min, and 298 K temperature. Afterwards, there was no significant removal achieved above this mixing rate under similar conditions. This observation could be ascribed to improved interaction between the sorption-active sites and Cd ions in aqueous solution with an increase mixing rate [25]. The value of 150 rpm was chosen as optimum mixing rate.

3.2.5. Effect of Initial Concentrations. Investigating the initial concentration of metal ion is essential in the sorption studies because water and wastewaters contamination does have diverse metal ion concentrations; hence, knowledge of its influence is required for an elaborate sorption

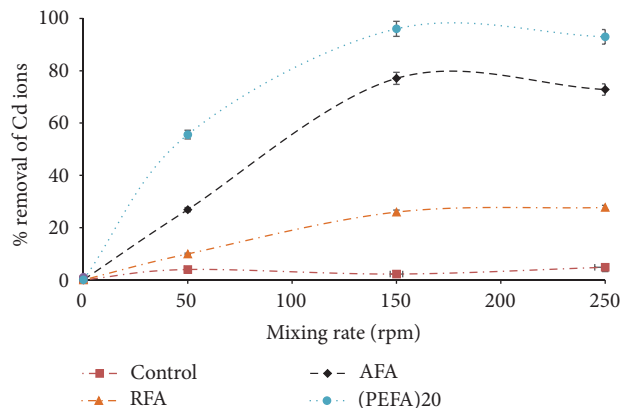


FIGURE 12: The influence of mixing rate on the removal efficiency of Cd (II) ions on FA based adsorbents (RFA, AFA, and PEFA) as a function of pH value of 9, 2 mg/L metal ion concentration, contact time of 15 min, 4 g/L adsorbent dosage, 50 mL volume of aqueous solution, and 298 K temperature.

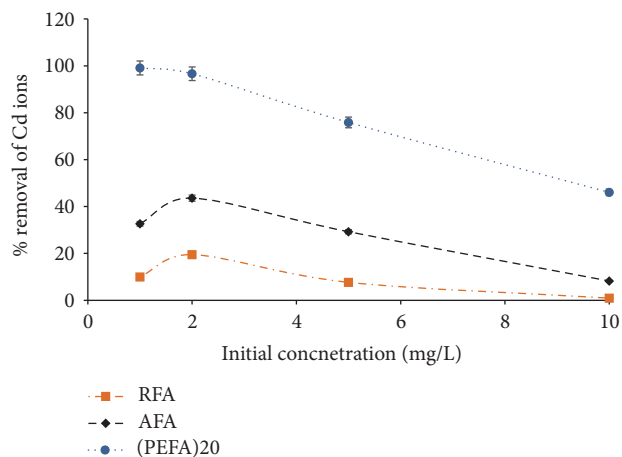


FIGURE 13: The influence of initial concentration on the removal efficiency of Cd (II) ions on FA based adsorbents (RFA, AFA, and PEFA) as a function of pH value of 9, 150 rpm mixing rate, contact time of 15 min, 4 g/L adsorbent dosage, 50 mL volume of aqueous solution, and 298 K temperature.

investigation [9]. The effect of Cd ion concentration in aqueous solution on its sorption by RFA, AFA, and PEFA was conducted with 4 g/L dose of adsorbent, pH value of 9, 150 rpm mixing rate, 15 min contact time, and 298 K temperature. Initial Cd ions concentrations investigated were varied from 1 to 10 mg/L and their effects on the removal efficiency were established. In Figure 13, it was observed that increasing the initial concentration of Cd (II) ions in solution could cause a decline in the removal efficiency of RFA, AFA, and PEFA. This can be ascribed to bulky quantities of Cd (II) ion with inadequate active sites on the surface of the adsorbents which resulted in increased concentration of Cd (II) ion in the greater part of the aqueous solution and as a result decreasing Cd ion removal efficiency [9, 25].

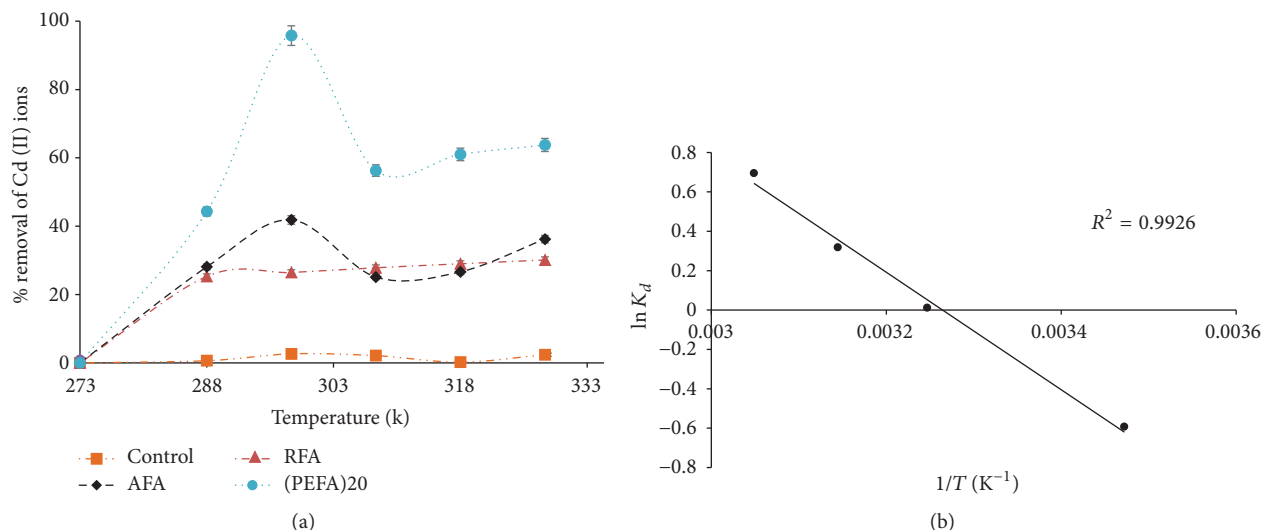


FIGURE 14: (a) The influence of temperature on the removal efficiency of Cd (II) ions on FA based adsorbents (RFA, AFA, and PEFA) as a function of pH value of 9, 2 mg/L metal ion concentration, 150 rpm mixing rate, contact time of 15 min, 4 g/L adsorbent dosage, and 50 mL volume of aqueous solution. (b) Van Hoff plot for Cd ion sorption at pH value of 9, 2 mg/L metal ion concentration, 150 rpm mixing rate, PEFA, contact time of 15 min, 4 g/L adsorbent dosage, and 50 mL volume of aqueous solution.

3.2.6. Effect of Temperature. Figure 14(a) illustrates Cd ion sorption on RFA, AFA, and PEFA at different temperatures. It can be deduced from the graph that an initial rise in temperature brings about a sharp increase in Cd (II) sorption from 273 to 298 K [38, 48]. This observation could be attributed to the fact that more chemical sites were present as temperature rises from 288 to 298 K to surface component dissociation on PEFA. This also suggests that the adsorption mechanism of Cd (II) ion on PEFA could be chemical sorption in addition to physical sorption as observed for RFA in which sorption increases with an increase in temperature. After a drop in removal efficiency at 308 K, there was a steady increase up till 328 K, suggesting that a high temperature might be a favorable factor in the sorption process as well and indicating that the adsorption is endothermic [9, 38].

To assess the feasibility and spontaneity of sorption process, thermodynamic parameters like ΔG° (free energy change), ΔH° (enthalpy change), and ΔS° (entropy change) were determined as shown in Table 2. Gibbs free energy change of sorption was calculated from the following equation:

$$\Delta G^\circ = -RT \ln K_d, \quad (10)$$

where R is 8.314 J/mol·K, T (K) is the absolute temperature, and K_d is the distribution coefficient expressed as $K_d = q_e/C_e$, where q_e is the amount of Cd ion adsorbed at equilibrium and C_e is the concentration of Cd ion in aqueous solution at equilibrium.

$$\ln K_d = -\frac{\Delta G^\circ}{RT} \quad (11)$$

$$\ln K_d = -\frac{\Delta H^\circ}{RT} + \frac{\Delta S^\circ}{R}. \quad (12)$$

TABLE 2: Thermodynamic parameters for Cd (II) ions adsorption by polyelectrolyte-coated fly ash (PEFA).

T (K)	K_d	ΔG° (KJ/mol)	ΔH° (KJ/mol)	ΔS° (J/mol/K)
288	0.55306	1.41818	24.80814	80.98418
298	4.12617	-3.5116		
308	1.01149	-0.0293		
318	1.37544	-0.8428		
328	2.00362	-1.8951		

Equation (12) is known as the Van Hoff equation; the values of ΔH° and ΔS° were calculated from slope and intercept of the plot of $\ln K_d$ against T^{-1} (K⁻¹) as indicated in Figure 14(b).

3.3. Isotherm and Kinetic Studies

3.3.1. Langmuir and Freundlich Isotherm Models. In order to determine the maximum sorption capacities of PEFA, data gotten at equilibrium for sorption experiment were employed. Figures 15(a) and 15(b) illustrate Langmuir and Freundlich isotherm models for Cd (II) at optimum pH (9). The maximum sorption capacity and adsorption intensity values were calculated from the slope and intercept of the plots between $1/q_e$ and $1/C_e$ for Langmuir as in q_m and K_L [31] and between $\ln q_e$ and $\ln C_e$ for Freundlich as in K_f and n [49], respectively. Table 3 shows the correlation coefficient values (R^2) for both Langmuir and Freundlich as well as other parameters. This implies that both models fitted well for the experimental data. Nonetheless, the important features of Langmuir parameters can be applied to further forecast the interaction between the adsorbate and adsorbent

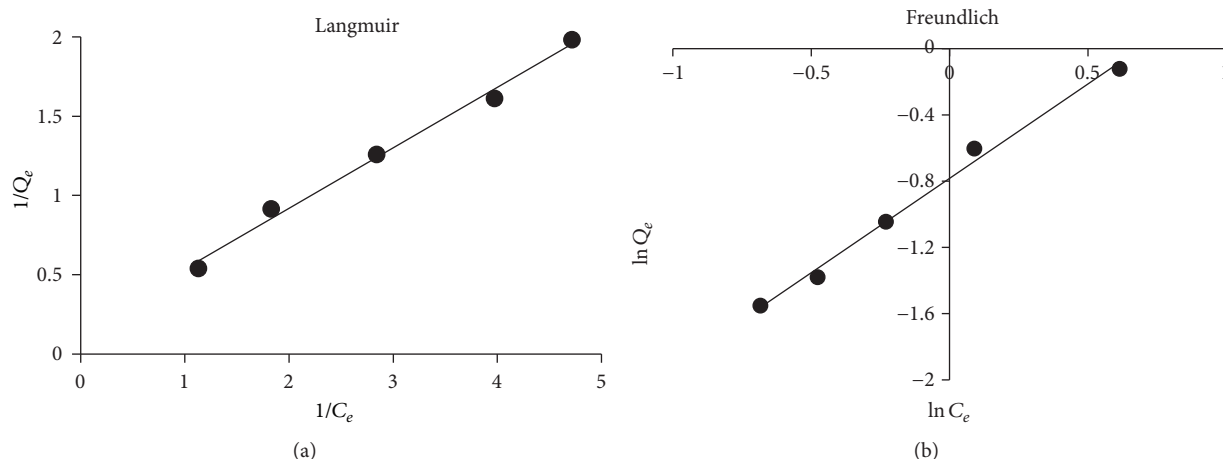


FIGURE 15: (a) Langmuir adsorption isotherm model. (b) Freundlich adsorption isotherm model.

TABLE 3: Langmuir and Freundlich constants for Cd (II) ion uptake.

	Langmuir constants					Freundlich constants		
	R^2	K_L	Q_{max}	R_L	θ	R^2	K_f	$1/n$
PEFA	0.9918	0.4101	6.3939	0.4714	0.5286	0.9924	0.4568	0.878

TABLE 4: Sorption kinetics parameters for Cd (II) ion adsorption by PEFA.

	Pseudo-1st-order			Pseudo-2nd-order			Intraparticle diffusion		
	q_e	K_1	R^2	q_e	K_2	R^2	K_i	C	R^2
PEFA	148.9	0.0619	0.9802	0.6052	4.2983	0.999	0.0046	0.8413	0.8365

with the aid of dimensionless separation parameters (R_L) as indicated in the following equation:

$$R_L = \frac{1}{1 + K_L C_i}, \quad (13)$$

where K_L is Langmuir constant and C_i is Cd (II) ions initial concentration. R_L value gives essential information on sorption nature. R_L value for this study as shown in Table 3 indicates a favorable adsorption process ($R_L < 1$) for 2 mg/L Cd (II) ion concentration [9, 38, 49]. Adsorption of PEFA can also be explained in terms of surface area coverage in contrast to initial concentration of Cd ion [38]. Langmuir model for surface area coverage of adsorbent surface can be illustrated with aid of the following equation:

$$K_L C_i = \frac{\theta}{1 - \theta}, \quad (14)$$

where θ is the surface area coverage of adsorbent surface as indicated in Table 3.

3.3.2. Kinetic Studies of Adsorption. As indicated in (7), (8), and (9), kinetic studies of sorption data were evaluated by different kinetic models like pseudo-1st-order model, pseudo-2nd-order model, and intraparticle diffusion [43, 49, 50]. Sorption of cadmium ions was supervised at different period of time. Sorption of Cd (II) ions was calculated

from data acquired. To determine the appropriate kinetic model, Cd (II) ion adsorption was plotted against time. These data were fitted into pseudo-1st-order, pseudo-2nd-order, and Weber intraparticle diffusion equations [43]. Table 4 shows that values of q_e and K_i were calculated from K_i (Slope) and $\ln q_e$ (intercept) of plot $\ln(q_e - q_t)$ versus t . The correlation coefficient value ($R^2 = 0.9802$) for pseudo-1st-order model was lower than that of pseudo-2nd-order model. This could be linked to the fact that sorption kinetics take place chemically and involve forces of valency via ions sharing or electron exchange between adsorbent and the adsorbed ions on PEFA [46, 51]. Values of q_e and K_2 were calculated from q_e and $1/q_e$ (slope) and $1/K_2 q_e^2$ (intercept) of the plot. The correlation ($R^2 = 0.9999$) for pseudo-2nd-order model was very strong, pointing towards the fact that sorption of cadmium ions occurred on a monolayer mode, with the assumption that the rate limiting factor could be chemical sorption [38]. This indicated that the cadmium ions were chemically bonded to definite active sites on the surface of PEFA. Weber and Morris' intraparticle diffusion equation was also plotted for q_t against $t^{1/2}$ [50]. Values of K_i and C were calculated from K_i (slope) and C (intercept) as shown in Table 4. Its correlation value ($R^2 = 0.8365$) was the lowest and the plot intercept did not pass through the origin pointing towards some control of boundary layers and suggesting that intraparticle pore diffusion is not the only rate limiting factor [38]. The intraparticle diffusion

equation plot highlights multilinearity, indicating a three-stage process. The initial sharper part is linked to the diffusion of Cd (II) ions via the solution to the external surface of PEFA or boundary layer diffusion of solid molecules [38]. The second part gives description of ion phase, where intraparticle diffusion is a rate limiting factor. The third part is ascribed to the final equilibrium phase. Nonetheless, the intercept of the plot (not shown) fails to pass through the origin, which may be attributed to the difference in the rate of mass transfer in the initial and final phases of sorption [52].

4. Conclusion

This study has demonstrated that polyelectrolyte-coated fly ash (PEFA) performed as an excellent adsorbent for Cd (II) ion in aqueous solution. Adsorption of Cd (II) on PEFA surface was dependent on the dosage of adsorbent, pH of the aqueous solution, contact time, Cd (II) initial concentration, and temperature. Optimum conditions for Cd ions removal were found to be at an adsorbent dose of 4 g/L, pH value of 9, 15 min contact time, mixing rate of 150 rpm, 2 mg/L Cd initial concentration, and 298 K temperature. The maximum sorption capacity of PEFA was achieved at 6.40 mg/g with the experimental data fitting well to both Langmuir and Freundlich isotherm models and following pseudo-2nd-order kinetics. The investigation of thermodynamic parameters suggested that the adsorption of Cd (II) ions interaction with PEFA was endothermic and spontaneous and was increasing disorderliness of solute solution interface. This research highlights that fly ash material, a hazardous industrial waste, has a great potential in water treatment application.

Conflicts of Interest

The authors declare that there are no conflicts of interest regarding the publication of this paper.

Acknowledgments

The authors would like to acknowledge the support provided by King Abdulaziz City for Science and Technology (KACST) through Science & Technology Unit at King Fahd University of Petroleum & Minerals (KFUPM) for funding this work through Project no. 13-ADV161-04 as part of the National Science Technology and Innovation Plan (NSTIP).

References

- [1] M. N. Chong, B. Jin, C. W. K. Chow, and C. Saint, "Recent developments in photocatalytic water treatment technology: a review," *Water Research*, vol. 44, no. 10, pp. 2997–3027, 2010.
- [2] G.-M. Zeng, X. Li, J.-H. Huang et al., "Micellar-enhanced ultrafiltration of cadmium and methylene blue in synthetic wastewater using SDS," *Journal of Hazardous Materials*, vol. 185, no. 2-3, pp. 1304–1310, 2011.
- [3] S. O. Lesmana, N. Febriana, F. E. Soetaredjo, J. Sunarso, and S. Ismadji, "Studies on potential applications of biomass for the separation of heavy metals from water and wastewater," *Biochemical Engineering Journal*, vol. 44, no. 1, pp. 19–41, 2009.
- [4] WHO, "Guidelines for the safe use of wastewater, excreta and greywater," *World Health Organization*, vol. I, p. 95, 2006.
- [5] K. Rao, M. Mohapatra, S. Anand, and P. Venkateswarlu, "Review on cadmium removal from aqueous solutions," *International Journal of Engineering, Science and Technology*, vol. 2, no. 7, pp. 81–103, 2010.
- [6] F. A. Al-Khaldi, B. Abu-Sharkh, A. M. Abulkibash, and M. A. Atieh, "Cadmium removal by activated carbon, carbon nanotubes, carbon nanofibers, and carbon fly ash: a comparative study," *Desalination and Water Treatment*, vol. 53, no. 5, pp. 1417–1429, 2015.
- [7] R. Han, H. Li, Y. Li, J. Zhang, H. Xiao, and J. Shi, "Biosorption of copper and lead ions by waste beer yeast," *Journal of Hazardous Materials*, vol. 137, no. 3, pp. 1569–1576, 2006.
- [8] A. H. Mahvi and E. Bazrafshan, "Removal of Cadmium from Industrial effluents by electrocoagulation process using aluminum electrodes," vol. 2, no. 1, pp. 34–39, 2007.
- [9] K. G. Akpomie, F. A. Dawodu, and K. O. Adebowale, "Mechanism on the sorption of heavy metals from binary-solution by a low cost montmorillonite and its desorption potential," *Alexandria Engineering Journal*, vol. 54, no. 3, pp. 757–767, 2015.
- [10] M. Imamoglu and O. Tekir, "Removal of copper (II) and lead (II) ions from aqueous solutions by adsorption on activated carbon from a new precursor hazelnut husks," *Desalination*, vol. 228, no. 1-3, pp. 108–113, 2008.
- [11] T. Vidhyadevi, A. Murugesan, S. S. Kalaivani et al., "Optimization of the process parameters for the removal of reactive yellow dye by the low cost *Setaria verticillata* carbon using response surface methodology: thermodynamic, kinetic, and equilibrium studies," *Environmental Progress & Sustainable Energy*, vol. 33, no. 3, pp. 855–865, 2014.
- [12] S. Larous, A.-H. Meniai, and M. Bencheikh Lehocine, "Experimental study of the removal of copper from aqueous solutions by adsorption using sawdust," *Desalination*, vol. 185, no. 1-3, pp. 483–490, 2005.
- [13] E. Erdem, N. Karapinar, and R. Donat, "The removal of heavy metal cations by natural zeolites," *Journal of Colloid and Interface Science*, vol. 280, no. 2, pp. 309–314, 2004.
- [14] W. E. Marshall and E. T. Champagne, "Agricultural byproducts as adsorbents for metal ions in laboratory prepared solutions and in manufacturing wastewater," *Journal of Environmental Science and Health. Part A: Environmental Science and Engineering and Toxicology*, vol. 30, no. 2, pp. 241–261, 1995.
- [15] H. Aydin, Y. Bulut, and Ç. Yerlikaya, "Removal of copper (II) from aqueous solution by adsorption onto low-cost adsorbents," *Journal of Environmental Management*, vol. 87, no. 1, pp. 37–45, 2008.
- [16] A. Papandreou, C. J. Stournaras, and D. Panias, "Copper and cadmium adsorption on pellets made from fired coal fly ash," *Journal of Hazardous Materials*, vol. 148, no. 3, pp. 538–547, 2007.
- [17] M. Visa and A. Duta, "Cadmium and nickel removal from wastewater using modified fly ash?: Thermodynamic and kinetic study," *Sci. Stu. and Res*, vol. IX, no. 1, pp. 73–82, 2008.
- [18] G. Gupta and N. Torres, "Use of fly ash in reducing toxicity of and heavy metals in wastewater effluent," *Journal of Hazardous Materials*, vol. 57, no. 1-3, pp. 243–248, 1998.
- [19] F. A. Olabemiwo, "The Potential Capacity of Polyelectrolyte coated Carbon Fly Ash in Removing Cadmium from Contaminated water," *King Fahd University of Petroleum and Minerals*, 2017.
- [20] B. Bolto and J. Gregory, "Organic polyelectrolytes in water treatment," *Water Research*, vol. 41, no. 11, pp. 2301–2324, 2007.

- [21] X. Zhang, M. Chen, Y. Yu, T. Yang, and J. Wang, "Polyelectrolyte-modified multi-walled carbon nanotubes for the adsorption of chromium(vi)," *Analytical Methods*, vol. 3, no. 2, pp. 457–462, 2011.
- [22] D.-L. Huang, G.-M. Zeng, C.-L. Feng et al., "Degradation of lead-contaminated lignocellulosic waste by *Phanerochaete chrysosporium* and the reduction of lead toxicity," *Environmental Science and Technology*, vol. 42, no. 13, pp. 4946–4951, 2008.
- [23] B. W. Stanton, J. J. Harris, M. D. Miller, and M. L. Bruening, "Ultrathin, multilayered polyelectrolyte films as nanofiltration membranes," *Langmuir*, vol. 19, no. 17, pp. 7038–7042, 2003.
- [24] I. Y. El-Sherif and N. A. Fathy, "Modification of adsorptive properties of bagasse fly ash for uptaking cadmium from aqueous solution," *Environmental Research, Engineering and Management*, vol. 2, no. 2, pp. 19–28, 2013.
- [25] H. A. Asmaly, Ihsanullah, B. Abussaud et al., "Adsorption of phenol on aluminum oxide impregnated fly ash," *Desalination and Water Treatment*, vol. 57, no. 15, pp. 6801–6808, 2016.
- [26] M. Anwar Parvez, H. I. Al-Abdul Wahhab, R. A. Shawabkeh, and I. A. Hussein, "Asphalt modification using acid treated waste oil fly ash," *Construction and Building Materials*, vol. 70, pp. 201–209, 2014.
- [27] R. Shawabkeh, M. J. Khan, A. A. Al-Juhani, H. I. Al-Abdul Wahhab, and I. A. Hussein, "Enhancement of surface properties of oil fly ash by chemical treatment," *Applied Surface Science*, vol. 258, no. 5, pp. 1643–1650, 2011.
- [28] R. Shawabkeh, O. Khashman, and S. Tarawneh, "Synthesis of activated carbon from spent lubricating oil and application for adsorption of cadmium and lead ions from aqueous solution," *Combined and Hybrid Adsorbents, J.M. Loure*, pp. 195–200, 2006.
- [29] F. A. Abuilawi, T. Laoui, M. Al-Harthi, and M. A. Atieh, "Modification and functionalization of multiwalled carbon nanotube (MWCNT) via fischer esterification," *The Arabian Journal for Science and Engineering*, vol. 35, no. 1, pp. 37–48, 2010.
- [30] Q. Li, B. Wang, C. Li, J. Pang, and J. Zhai, "Synthesis of fly-ash cenospheres coated with polypyrrole using a layer-by-layer method," *Journal of Physics D: Applied Physics*, vol. 44, no. 44, Article ID 445301, 2011.
- [31] I. Langmuir, "The adsorption of gases on plane surfaces of glass, mica and platinum," *The Journal of the American Chemical Society*, vol. 40, no. 9, pp. 1361–1403, 1918.
- [32] Y. S. Al-Degs, A. Ghir, H. Khoury, G. M. Walker, M. Sunjuk, and M. A. Al-Ghouti, "Characterization and utilization of fly ash of heavy fuel oil generated in power stations," *Fuel Processing Technology*, vol. 123, pp. 41–46, 2014.
- [33] S. Vitolo, M. Seggiani, S. Filippi, and C. Brocchini, "Recovery of vanadium from heavy oil and Orimulsion fly ashes," *Hydrometallurgy*, vol. 57, no. 2, pp. 141–149, 2000.
- [34] M. Pires and X. Querol, "Characterization of Candiota (South Brazil) coal and combustion by-product," *International Journal of Coal Geology*, vol. 60, no. 1, pp. 57–72, 2004.
- [35] J. Coates, "Interpretation of infrared spectra, a practical approach interpretation of infrared spectra, a practical approach," *Encycl. Anal. Chem*, pp. 10815–10837, 2000.
- [36] R. Shawabkeh, M. J. Khan, A. A. Al-Juhani, H. I. Al-Abdul Wahhab, and I. A. Hussein, "Enhancement of surface properties of waste oil fly ash by chemical treatment," pp. 1–8, Proceedings of the 3rd International Conference on Industrial and hazardous waste management (CRETE'12), 2012.
- [37] Yaofa Jiang, E. R. Elswick, and M. Mastalerz, "Progression in sulfur isotopic compositions from coal to fly ash: Examples from single-source combustion in Indiana," *International Journal of Coal Geology*, vol. 73, no. 3–4, pp. 273–284, 2008.
- [38] V. Rathod, H. Pansare, S. A. Bhalerao, and S. D. Maind, "Adsorption and Desorption Studies of Cadmium (II) ions from aqueous solutions onto Tur pod (*Cajanus cajan*)," *Int. J. Adv. Chem. Res*, vol. 4, no. 5, pp. 30–38, 2015.
- [39] B. Wang, Q. Li, J. Kang, J. Pang, W. Wang, and J. Zhai, "Preparation and characterization of polypyrrole coating on fly ash cenospheres: role of the organosilane treatment," *Journal of Physics D: Applied Physics*, vol. 44, no. 41, Article ID 415301, 2011.
- [40] C. Guo, L. Zhou, and J. Lv, "Effects of expandable graphite and modified ammonium polyphosphate on the flame-retardant and mechanical properties of wood flour-polypropylene composites," *Polymers and Polymer Composites*, vol. 21, no. 7, pp. 449–456, 2013.
- [41] W. T. Kwon, D. H. Kim, and Y. P. Kim, "Characterization of heavy oil fly ash generated from a power plant," *Azo J. Mater. online*, pp. 1–10, 2005.
- [42] J. Zou, Y. Dai, X. Wang et al., "Structure and adsorption properties of sewage sludge-derived carbon with removal of inorganic impurities and high porosity," *Bioresource Technology*, vol. 142, pp. 209–217, 2013.
- [43] R. Leyva-Ramos, J. R. Rangel-Mendez, J. Mendoza-Barron, L. Fuentes-Rubio, and R. M. Guerrero-Coronado, "Adsorption of cadmium(II) from aqueous solution onto activated carbon," *Water Sci. Technol*, vol. 35, no. 7, pp. 205–211, 1997.
- [44] Ihsanullah, F. A. Al-Khalidi, B. Abusharkh et al., "Adsorptive removal of cadmium(II) ions from liquid phase using acid modified carbon-based adsorbents," *Journal of Molecular Liquids*, vol. 204, pp. 255–263, 2015.
- [45] G. H. Pino, L. M. Souza De Mesquita, M. L. Torem, and G. A. S. Pinto, "Biosorption of cadmium by green coconut shell powder," *Minerals Engineering*, vol. 19, no. 5, pp. 380–387, 2006.
- [46] K. Akpomie and F. Dawodu, "Physicochemical analysis of automobile effluent before and after treatment with an alkaline-activated montmorillonite," *Journal of Taibah University for Science*, vol. 9, no. 4, pp. 465–476, 2015.
- [47] M. A. Atieh, "Removal of phenol from water different types of carbon – a comparative analysis," *Procedia - Soc. Behav. Sci.*, vol. 10, pp. 136–141, 2014.
- [48] G. C. Catena and F. V. Bright, "Thermodynamic study on the effects of β -cyclodextrin inclusion with anilino-naphthalenesulfonates," *Analytical Chemistry*, vol. 61, no. 8, pp. 905–909, 1989.
- [49] G. McKay, Y. S. Ho, and J. C. Y. Ng, "Biosorption of copper from waste waters: A review," *Separation and Purification Methods*, vol. 28, no. 1, pp. 87–125, 1999.
- [50] W. J. Weber, *Physicochemical processes for water quality control*, Wiley-Interscience, New York, NY, USA, 1972.
- [51] C. Septhum, S. Rattanaphani, J. B. Bremner, and V. Rattanaphani, "An adsorption study of Al(III) ions onto chitosan," *Journal of Hazardous Materials*, vol. 148, no. 1–2, pp. 185–191, 2007.
- [52] G. Prasad, K. K. Pandey, and V. N. Singh, "Mixed adsorbents for Cu(II) removal from aqueous solutions," *Environmental Technology Letters*, vol. 7, no. 1–12, pp. 547–554, 1986.

Research Article

Enhanced Adsorption of Selenium Ions from Aqueous Solution Using Iron Oxide Impregnated Carbon Nanotubes

Omer Y. Bakather,^{1,2} Ahmad Kayvani Fard,^{3,4} Ihsanullah,⁵ Majeda Khraisheh,⁶ Mustafa S. Nasser,⁷ and Muataz Ali Atieh^{3,4}

¹Department of Chemical Engineering, Jazan University, P.O. Box 706, Jazan 45142, Saudi Arabia

²Department of Chemical Engineering, Hadhramout University, Hadhramout, Yemen

³Qatar Environment and Energy Research Institute, Hamad Bin Khalifa University, Qatar Foundation, P.O. Box 5825, Doha, Qatar

⁴College of Science and Engineering, Hamad Bin Khalifa University, Qatar Foundation, P.O. Box 5825, Doha, Qatar

⁵Department of Chemical Engineering, King Fahd University of Petroleum & Minerals, Dhahran 31261, Saudi Arabia

⁶Chemical Engineering Department, Qatar University, P.O. Box 2713, Doha, Qatar

⁷Gas Processing Centre, College of Engineering, Qatar University, P.O. Box 2713, Doha, Qatar

Correspondence should be addressed to Muataz Ali Atieh; mhussien@hbku.edu.qa

Received 5 February 2017; Revised 12 March 2017; Accepted 28 March 2017; Published 7 May 2017

Academic Editor: Spyros P. Perlepes

Copyright © 2017 Omer Y. Bakather et al. This is an open access article distributed under the Creative Commons Attribution License, which permits unrestricted use, distribution, and reproduction in any medium, provided the original work is properly cited.

The aim of this research was to investigate the potential of raw and iron oxide impregnated carbon nanotubes (CNTs) as adsorbents for the removal of selenium (Se) ions from wastewater. The original and modified CNTs with different loadings of Fe₂O₃ nanoparticles were characterized using high resolution transmission electron microscopy (HRTEM), scanning electron microscopy (SEM), X-ray diffractometer (XRD), Brunauer, Emmett, and Teller (BET) surface area analyzer, thermogravimetric analysis (TGA), zeta potential, and energy dispersive X-ray spectroscopy (EDS). The adsorption parameters of the selenium ions from water using raw CNTs and iron oxide impregnated carbon nanotubes (CNT-Fe₂O₃) were optimized. Total removal of 1 ppm Se ions from water was achieved when 25 mg of CNTs impregnated with 20 wt.% of iron oxide nanoparticles is used. Freundlich and Langmuir isotherm models were used to study the nature of the adsorption process. Pseudo-first and pseudo-second-order models were employed to study the kinetics of selenium ions adsorption onto the surface of iron oxide impregnated CNTs. Maximum adsorption capacity of the Fe₂O₃ impregnated CNTs, predicted by Langmuir isotherm model, was found to be 111 mg/g. This new finding might revolutionize the adsorption treatment process and application by introducing a new type of nanoadsorbent that has super adsorption capacity towards Se ions.

1. Introduction

Selenium (Se) is unique nonmetal chemical element with five known oxidative states under the form of elemental selenium Se⁰, namely, 0, -1, -2, +4, and +6 [1]. Although it is an important trace element for many organisms, exceeding homeostatic levels is considered toxic. Se is typically found on the earth's crust, rocks, and sedimentary soils [2]. Recent reports state that a significant amount of Se emissions into the atmosphere and aquatic environment is related to industrial and mining activities in addition to agricultural drainage run-off [3–5].

Tan et al. [6], in a recent extensive review, reported the different types of organic and inorganic Se species available. The inorganic form of Se is typically found in surface and ground water in a number of reported forms such as Se⁻² (selenide), SeO₃⁻² (selenite), SeO₄⁻² (selenate), and Se⁰, which is the species nonsoluble form. If found in high concentration levels in waste or surface water, Se can cause serious environmental problems [7, 8]. The maximum level for Se in surface water was set at 5.0 µg/L by the United States Environmental Protection Agency (USEPA) in 1999. Therefore, due to the increased interest in Se treatment and the more

stringent environmental consent levels for its concentration in surface water, the value set in 1999 is being updated by USEPA in 2014 [1, 5, 9]. Furthermore, there is variation in the maximum allowable levels of Se in drinking water worldwide. According to the World Health Organization [10] the value is set at 40 $\mu\text{g/L}$, while the European Union (EU) sets the Se levels at a much lower value of 10 $\mu\text{g/L}$ [11]. In order to meet the drinking water standards for Se in addition to treating industrial, mining wastewaters and agricultural run-offs, a varied number of treatment processes are reported in the open literature with various degrees of complexity and advancement. Comprehensive reviews conducted by Robberecht and Van Grieken [4] and Tan et al. [6] offer an excellent overview of all current known treatments used for Se. It can be seen from the two recent reviews that although a great variety of biological [12–14], chemical [15–20], and physical treatments technologies [9, 21, 22] were developed in recent years, no single treatment offers a complete and cost effective scheme for treating Se from waste or drinking water. While biological treatments stand as one of the best options for treating Se, challenges related to long-term stability of the biogenic selenium and the predicting of the fate of the bio-reduced Se in the environment are two major concerns. On the other hand, adsorption has been reported as an effective lower cost treatment technology for Se removal [23]. Varied adsorbents have been tested including low cost alternative materials [4], activated carbons, and other metal-oxide-enhanced materials. Of the latter, metal-oxide-enhanced materials with ferrihydrite have been reported as the most promising materials for the treatment of water containing SeO_3^{-2} ions [16]. Reports showed that the strong affinity of SeO_3^{-2} to iron hydroxide surfaces resulted in around 99% removal rate for a wide pH range (3–8). In contrast, the process was not effective for SO_4^{-2} and its presence acted as a competitor for the desorption sites causing suppressed removal rates [20]. The inadequate SO_4^{-2} removal was also related to interacting between the various Se species and the surface of the adsorbent. While SeO_3^{-2} was reported to form inner-sphere adsorption on iron hydroxide adsorbents, SO_4^{-2} , on the other hand, was adsorbed in an outer sphere manner resulting in an ineffective removal [16]. Accordingly, the development of a process to remove effectively most of the possible inorganic forms of Se is still required. With this in mind and due to their high surface areas, recent studies reported the use of various nanomaterials for the removal of the Se oxyanions. Example such as hydrophilic magnetic nanoparticle-graphene oxide composite was reported recently by Fu et al. [16]. A two-step reaction was used in the preparation of the adsorbents in addition to deposition of iron oxide nanoparticles at high temperatures. The authors reported a maximum removal of 95% of Se (VI) ions at pH \sim 2. While it is not easy to compare the maximum capacity of an adsorbent for the Se removal given the varied preparation methods, costs, and experimental condition, a recent study using a new iron oxide nanoparticles reported a higher removal rates compared with literature reported values [18]. Having said that, the values are still small and the search for other adsorbents is still required for cost effective Se removal from water.

Accordingly, this study is focused on developing multi-walled carbon nanotubes based novel materials for effective removal of Se from aqueous solutions. In recent years, multiwalled carbon nanotubes (CNTs) have been explored widely due to their unique properties [24–26] and have been extensively used in nanotechnology, optics, electronics, material science, and water treatment [27]. CNTs were also reported for the adsorption of heavy metal ions [28–32] and organic compounds [33–36]. Despite the most recent comprehensive review articles and to the best of our knowledge, no studies were reported on the use of multiwalled carbon nanotubes for Se removal. In this work, iron oxide impregnated CNTs were employed for the adsorption of the selenium ions from water. The effect of iron oxide loading, pH, dosage of CNTs, contact time, and initial concentration were studied on the removal of selenium. The raw CNTs and impregnated CNTs were characterized using field emission scanning electron microscopy (FE-SEM), high transmission electron microscopy (HR-TEM), thermogravimetric analysis (TGA), X-ray diffractometer (XRD), energy dispersive X-ray spectroscopy (EDS), Brunauer, Emmett, and Teller (BET) nitrogen adsorption technique, and zeta potential. The adsorption equilibrium data were correlated by the Langmuir and Freundlich isotherms and the kinetic data were analyzed using two kinetic models.

2. Experimental

2.1. Materials. All solvents used in this study were of analytical grade and purchased from Sigma-Aldrich Co. Ltd. Ethanol liquid (98%, purity) was used as a solvent and iron (III) nitrate as a precursor of iron nanoparticles and selenium dioxide (SeO_2) was used as source of selenium ions in the water.

2.2. Production of Carbon Nanotubes. Floating catalyst chemical vapor deposition reactor was used for the production of CNTs. The experimental setup used and reaction conditions are reported previously by Fard et al. [26]. Briefly, injected vertical chemical vapor deposition (FC-CVD) with quartz tube 100 mm in diameter and 1200 mm in length with flanges fixed at both ends was used to synthesis CNTs. Xylene was used as source of hydrocarbon and the argon gas was used to flush the air from the system, while the hydrogen gas was used as a carrier and reacting gas. Purity of CNTs produced was $>96\%$.

2.3. Impregnation of CNTs. The iron oxide nanoparticles were impregnated on the surface of CNTs by a wet impregnation method. For 5% iron oxide loadings, 361 mg of Iron (III) nitrate nonahydrate and 1 g of CNTs were dissolved separately in ethanol solution and sonicated for 30 minutes to ensure uniform mixing. Upon further mixing of the two solutions and further sonication, the solution was kept in a furnace at 80°C overnight to evaporate the ethanol. Finally, the product was calcined at 350°C for 3 hours in the convection oven to ensure effective attachment of the iron oxide particles onto the surface of CNTs. After cooling, the composite of CNTs

with 5% iron oxide NP is synthesized. To produce CNTs with 10% and 20% iron oxide loading, 722 mg and 1.44 g Iron (III) nitrate nonahydrate are mixed with 1 g of CNTs, respectively. Details of the preparation are found elsewhere [37].

2.4. Characterization of Carbon Nanotubes

2.4.1. Crystal Structure. Powder X-ray diffraction (XRD) patterns were recorded using a Rigaku MiniFlex-600. The X-ray diffractometer with Cu K α radiation $\lambda = 1.54 \text{ \AA}$ at a rate of 0.4% over Bragg angles ranging from 10 to 90° was used for the analysis. The operating voltage and current were maintained at 40 kV and 15 mA, respectively.

2.4.2. Surface Structure. Scanning electron microscopy (SEM) was performed using FEI Quanta 200 Environmental Scanning Electron Microscope (ESEM) with a resolution of 5 nm and magnification 200K to observe the morphology and structure of the material. Also, the morphological and structural analysis of CNTs was conducted using transmission electron microscopy (TEM) (CM12, Philips).

2.4.3. Point of Zero Charge. To measure the surface charge and zeta potential Zetasizer (Nano ZS 90, Malvern Instruments Ltd., Malvern, UK) equipped with a 4.0 mW internal laser was used. The Zetasizer works on the principle of dynamic light scattering (DLS). The measurements were performed at room temperature (25°C) with a scattering angle of 90°.

2.4.4. Other Chemical Properties and Surface Area. To analyze physical and chemical properties of CNTs with respect to temperature, the thermogravimetric analyses were performed using a TGA analyzer (SDT, Q600) at a heating rate of 10°C/min in air. The surface areas of CNTs were measured by N₂ adsorption at 77 K using BET surface area analyzer (Micromeritics ASAP 2020).

2.5. Preparation of the Selenium Stock Solution. Specific amount of SeO₂ was dissolved in deionized water to prepare the stock solution. SeO₂ dissolves in water to form selenous acid (SeO₂⁻³). The pH of the stock solution was adjusted by using 0.1 M NaOH or 0.1 M HNO₃ and maintained by the addition of buffer solutions.

2.6. Se Sorption Experiments. In order to assess the effectiveness of the new adsorbent, batch adsorption experiments were conducted at room temperature in 1 L glass beakers. 50 mL of selenium solution of required concentration was placed in the flasks, covered, and mounted on the mechanical rotary shaker (MPI Lab Shaker) to ensure adequate mixing. Different experimental runs were conducted to study the effect of solution pH, contact time, CNTs dosage, and initial Se (IV) ions concentration on the adsorption of Se ions. Inductively coupled plasma mass spectroscopy (ICP-MS) was employed to analyze the concentrations of the samples. The

adsorption capacity (Q) and removal efficiency (RE) were calculated as follows [37]:

$$Q = \frac{(C_i - C_f) \times V}{W_g} \quad (1)$$

$$RE (\%) = \frac{(C_i - C_f)}{C_i} \times 100,$$

where C_i (mg/L) is the initial concentration of selenium in the water, C_f (mg/L) is the final concentration of the selenium in the water, V (L) is the volume of the water, and W_g is the mass of CNTs.

2.7. Adsorption Isotherms Models. The Langmuir and Freundlich isotherms were used to study the adsorption performance and to determine the adsorption capacity for the adsorbent [37]. The Langmuir adsorption isotherm is expressed as follows:

$$Q_e = \frac{q_m K_L C_e}{1 + K_L C_e}, \quad (2)$$

where Q_e (mg/g) and q_m (mg/g) are the amount adsorbed at equilibrium and the maximum adsorption capacity, respectively, while C_e (mg/L) is the equilibrium adsorbate concentration and K_L is Langmuir constant.

Equation (2) can be linearized as follows:

$$\frac{C_e}{Q_e} = \frac{C_e}{q_m} + \frac{1}{K_L q_m}. \quad (3)$$

Freundlich isotherm is expressed as follows:

$$Q_e = K_f C_e^{1/n}. \quad (4)$$

Equation (4) can be linearized as follows:

$$\log Q_e = \frac{1}{n} \log C_e + \log K_f, \quad (5)$$

where n and K_f are the empirical constants.

2.8. Adsorption Kinetics. In order to find the maximum selenium removal by CNTs and to model the experimental data, two well-known kinetic models, pseudo-first-order and pseudo-second-order models, were used in this study.

The Lagergren pseudo-first-order model proposes that the rate of sorption is proportional to the number of sites unoccupied by the adsorbate [37]. The linear form of the pseudo-first-order equation can be expressed as follows:

$$\ln(Q_e - Q_t) = \ln Q_e - k_1 t, \quad (6)$$

where Q_t is the sorption capacity (mg/g) at any preset time interval (t) and k_1 is the pseudo-first-order rate constant (min^{-1}). A graph of $\ln(Q_e - Q_t)$ versus time is plotted and the constant is found. Additionally, the adsorption data

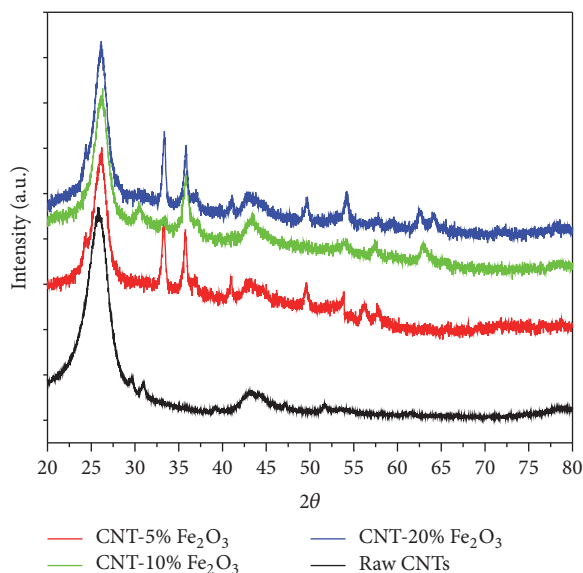


FIGURE 1: XRD analysis of raw CNTs, and CNT-5% iron oxide, CNT-10% iron oxide, and CNT-20% iron oxide.

were modeled to the pseudo-second-order kinetic model [37] where its linear form is expressed as follows:

$$\frac{t}{Q_t} = \frac{1}{k_2 Q_e^2} + \frac{t}{Q_e}, \quad (7)$$

where k_2 is the pseudo-second-order rate constant (g/mg·min). By plotting t/Q_t versus time, straight lines were obtained and the constants, k_2 and Q_e , were found.

3. Results and Discussion

3.1. Characterization of Carbon Nanotubes. Figure 1 shows the X-ray diffraction patterns of CNTs and impregnated CNTs with Fe_2O_3 nanoparticles. The XRD diffraction pattern of pure $\alpha\text{-Fe}_2\text{O}_3$ is similar to that of CNTs impregnated Fe_2O_3 nanoparticles confirming the presence of $\alpha\text{-Fe}_2\text{O}_3$ crystal nanoparticles on the surfaces of CNTs. The distinct peaks of $\alpha\text{-Fe}_2\text{O}_3$ crystalline structure are found at 2θ of 34, 36, 42, 50, 54, 63, 65, 72, and 75. The characteristic peak of CNTs was observed at 2θ of 27 which corresponds to C (002) and indicative of proper and undamaged graphite structure of the CNTs. The other characteristic diffraction peaks of graphite are at 2θ of 43°, 45°, and 77° and associated with C (100), C (101), and C (110) diffractions of graphite, respectively. Peaks indexed at C (002), C (100), and C (101) are indication of hexagonal structure of CNTs and the presence of C (002) peak in the XRD data confirms the multiwalled nature of the carbon nanotubes [42].

The sharp peak at the 2θ of 25.5° of the raw and impregnated CNTs is indicative of undamaged (no impurities in lattice) and developed graphite structure. Defects would have been observed in the CNTs if the 2θ peak of 25.5° was broader and a shift of the peak diffraction towards lower angles was detected. Peaks at 31, 44, and 52.5 are indicative of the multiwalled nature of the carbon nanotubes. The results

observed by the peaks in Figure 1 are a clear testament to the highly crystalline, uniform, highly ordered, and pure CNTs. The results here are further confirmed by SEM and TEM images.

In addition to XRD, the raw and impregnated CNTs were characterized further using field-scanning electron microscopy (FE-SEM), high resolution transmission electron microscopy (HR-TEM), thermogravimetry (TGA) techniques, XRD, BET surface area, and zeta potential.

The morphologies of these samples were obtained by SEM as shown in Figure 2. The diameter of the CNTs, with sponge-like structure, varied from 20 to 50 nm with an average diameter of 25 nm. The surface of CNTs after impregnation with Fe_2O_3 showed no surface changes and appeared to be agglomerated and untangled.

High resolution transmission electron microscopy (HR-TEM) was carried out to characterize the size, structure, and purity of the iron oxide nanoparticles doped and virgin CNTs. The raw CNTs TEM image presented in Figure 3 clearly indicates a highly ordered CNTs crystalline structure with diameter ranging from 10 to 30 nm and length from 10 to 30 μm . In addition, it can be noted that the clear fringes of the graphitic sheets are well separated by 0.35 nm and are aligned with a tilted angle of about 2° toward the tube axis. The TEM images of CNTs doped with Fe_2O_3 nanoparticles are presented in Figures 3(b)–3(d) in order to substantiate the presence of iron oxide nanoparticle on the surfaces of CNTs. The white iron oxide nanoparticles with some spherical and irregular shapes are shown in the TEM images. The size of Fe_2O_3 nanoparticles is estimated to be around 1–5 nm which are somehow distributed evenly and on some locations agglomerated slightly causing increase in the nanoparticle size.

To confirm the presence of iron oxide and also to experimentally find out the percentage of iron oxide nanoparticles on surface of CNTs, EDS analysis was conducted and the results are shown in Table 1.

The Fe_2O_3 content of the impregnated CNTs was also investigated using TGA. The experiment was carried out using air at a heating rate of 10°C/min. The thermograms are shown in Figure 4. Under this operating condition, the raw CNTs decomposed and oxidized completely as verified by the TGA curve in Figure 4. As Fe_2O_3 content on surface of CNTs increased, higher residual yield was found which corresponded to the presence of iron oxide NPs on the surface of CNT [37]. TGA provides an accurate estimate of the loading of iron oxide NPs doped on surface of CNTs by comparing the residues for the complete oxidation of the raw and impregnated CNTs. Therefore, CNTs with 1%, 10%, and 20% Fe_2O_3 loading had residual yields of 6 wt.%, 8 wt.%, and 17 wt.%, respectively. Moreover it can be noted that the increase in Fe_2O_3 NP loading resulted in a decrease of the decomposition temperature. It can also be inferred, from the TGA analysis shown in Figure 4, that raw CNTs start to decompose at 540°C while the 5%, 10%, and 20% loaded CNTs with Fe_2O_3 decomposed at lower temperatures (450, 430, and 410°C, resp.). According to Chiang et al. [43] the earlier decomposition of CNTs impregnated with metallic NPs can be explained by reduction of the thermal stability of CNTs by

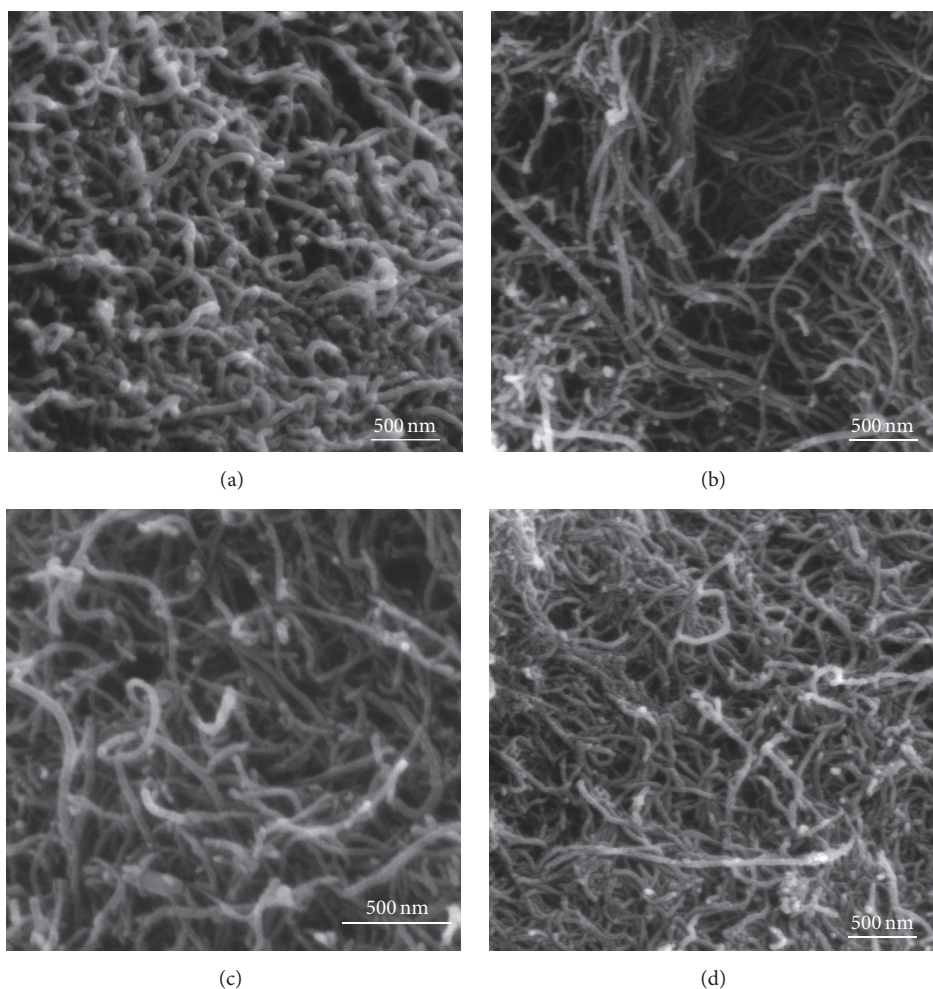


FIGURE 2: SEM images of (a) raw CNTs, (b) CNT-5% iron oxide, (c) CNT-10% iron oxide, and (d) CNT-20% iron oxide.

catalyzing the low-temperature oxidation of CNTs. Therefore, it can be inferred that the presence of nanosized iron oxide particles with high surface area altered the thermal stability of the CNTs and catalyzed oxidation of impregnated CNTs under the air compared to the pristine CNTs. The nanosized metallic particles might act as a heating accelerant that progresses the heat transfer to the surface of the CNTs and enhance the oxidation process.

The surface area of raw CNTs and impregnated CNTs was measured using BET surface area analyzer. As shown in Figure 5, the surface area of raw CNTs and CNTs impregnated with 5%, 10%, and 20% iron oxide nanoparticles was found to be 137.7, 226.6, 295.4, and 360 m²/g, respectively. The presence of the nanosized iron oxide particles doubled the surface area upon using 20 wt.% iron oxide nanoparticles. Increasing the surface area inherently increases the number of adsorption sites available for the removal of selenium and therefore results in higher adsorption capacity.

Finally, the surface charge of the CNTs and impregnated CNTs with iron oxide nanoparticles was measured and the results are illustrated in Figure 6. When the Fe₂O₃ nanoparticles were loaded onto the surface of CNTs the negative

sign of zeta potential on the surface of carbon nanotubes decreased due to neutralizing the repulsive effects of the electrical double layers. However, selenium (SeO₃²⁻) has very large negative zeta potential (-0.37 V). As the negative sign of zeta potential decreases, the electrostatic attraction would make and attachment between CNTs and selenium ions more likely [38]. Thus, it is important to decrease the electrostatic repulsion barrier between the selenium ions and CNTs to further improve the adsorption process. It is clear from the zeta potential measurements in Figure 6 that increasing the percentage of Fe₂O₃ nanoparticles onto the surface of CNTs caused a reduction in the negative sign of zeta potential. The trends obtained here are in good agreement with the adsorption measurements carried out in this work, where increasing the loading of Fe₂O₃ nanoparticle onto the surface of CNTs enhanced the removal of the selenium ions from the water. On the other hand, loading Fe₂O₃ NPs onto the surface of CNTs alters the point of zero charge (PZC) of the composite. PZC is a pH value at which material has zero zeta potential. Raw CNTs have PZC at pH of 4.6 while CNTs with 5%, 10%, and 20% Fe₂O₃ loading have PZC at pH of 5.2, 5.6, and 5.9, respectively.

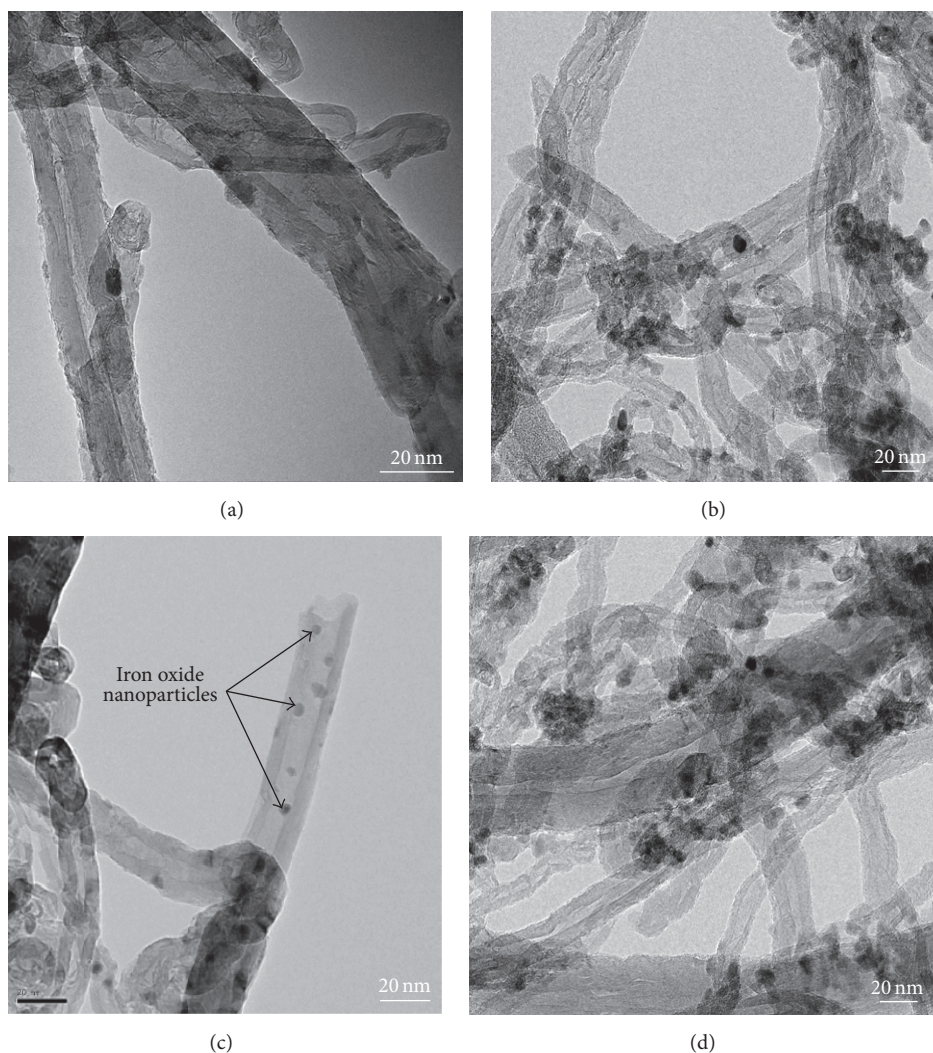


FIGURE 3: HRTEM images of (a) raw CNTs, (b) CNT-5% iron oxide, (c) CNT-10% iron oxide, and (d) CNT-20% iron oxide.

TABLE 1: EDS analysis of raw CNTs and CNTs with different percentage of Fe_2O_3 .

CNTs sample	Raw CNTs	CNT- Fe_2O_3 (5%)	CNT- Fe_2O_3 (10%)	CNT- Fe_2O_3 (20%)
Element	Weight %	Weight %	Weight %	Weight %
C	98.50	91.80	84.53	56.4
O	1.50	3.65	4.44	25.52
Fe	0	4.55	11.03	18.08
Total %	100	100	100	100

3.2. *Effect of pH.* The pH of the solution plays an important role in the adsorption of selenium ions on the adsorbent surface as it is dependent on the surface properties of the impregnated CNTs and distribution of selenium ions in water.

The effect of pH on the removal of selenium ions is presented in Figure 7. The adsorption of selenium species was higher at lower pH and the removal was observed to decrease with increase in pH for the impregnated CNTs. The

maximum removal was observed at pH 1. This higher removal at lower pH was due to the higher positive surface charges as indicated by zeta potential of the CNTs that favors the adsorption of anion (e.g., SeO_3^{2-}) [44]. This can be explained by release of OH ions when anion or weak acid is adsorbed onto hydroxide, which has favor toward adsorption of SeO_3^{2-} at low pH. Zhang et al. [38] used activated carbon doped with iron oxide for the removal of selenium from water. The authors reported that selenium removal sharply dropped after pH 8 and the maximum removal occurred in acidic solutions with pH between 1 and 3. A similar trend was previously observed in case of selenium ions adsorption on iron oxide nanoparticle [8], iron-coated GAC [38], hematite [45], soil [46], hydroxyapatite [39, 47], goethite and hydrous ferric oxide [48, 49], aluminum oxide coated sand [40], metal oxide nanoparticles [50], goethite [51], nanoscale zero-valent iron [52], and cellulose microcolumn [53].

It is anticipated that at lower pH, the adsorbent surface carries an additional positive charge and the anionic species are preferably adsorbed on the surface due to electrostatic

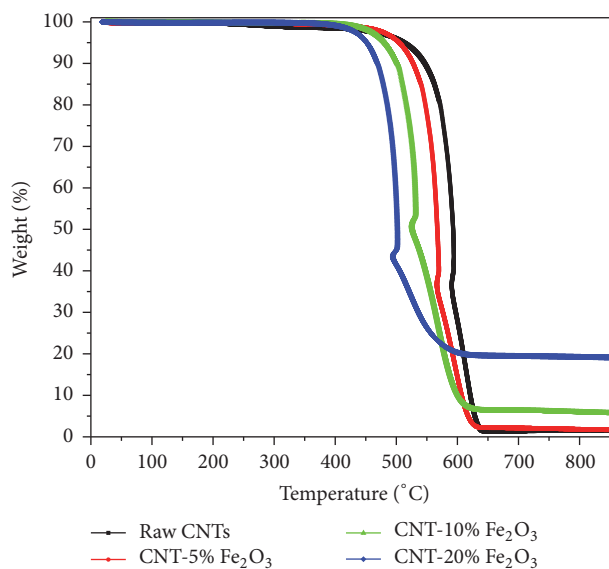


FIGURE 4: TGA analysis of raw CNTs and CNT-5% iron oxide, CNT-10% iron oxide, and CNT-20% iron oxide.

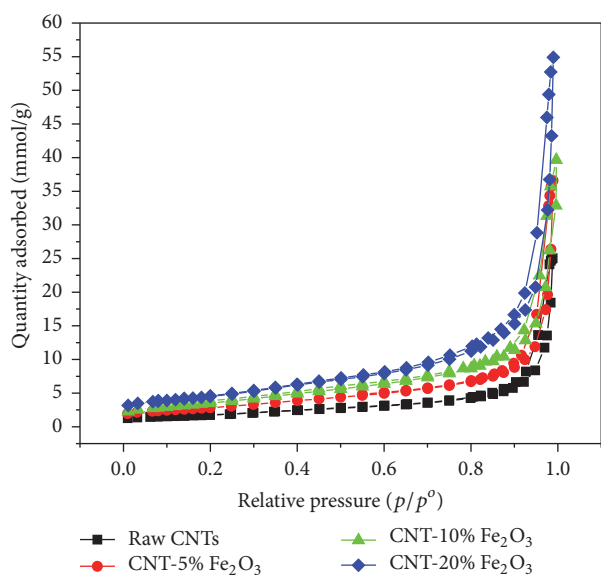


FIGURE 5: BET adsorption of N_2 at 77 K for raw CNTs and CNT-5% iron oxide, CNT-10% iron oxide, and CNT-20% iron oxide.

attractions [8, 46]. Monteil-Rivera et al. [47], however, reported that Se removal by hydroxyapatite increases with pH from pH 7 to 8.5, and it decreases above pH 8.5. In general, the adsorption capacity of Se was decreased slightly upon increasing the pH of solution. This might be due to the increase in the negative charge of the adsorbent surface and the consequent competition between the OH^- ions and selenium ions for the available adsorption sites [44, 45]. Figure 7 also reveals that raw CNTs were not efficient in removing Se ions from solution as shown in the flat trend that it depicts in Figure 6. The adsorption of selenium was less than 1% at pH between 1 and 2. Negligible (close to zero) was recorded at pH of 2. In contrast, it can be seen from the

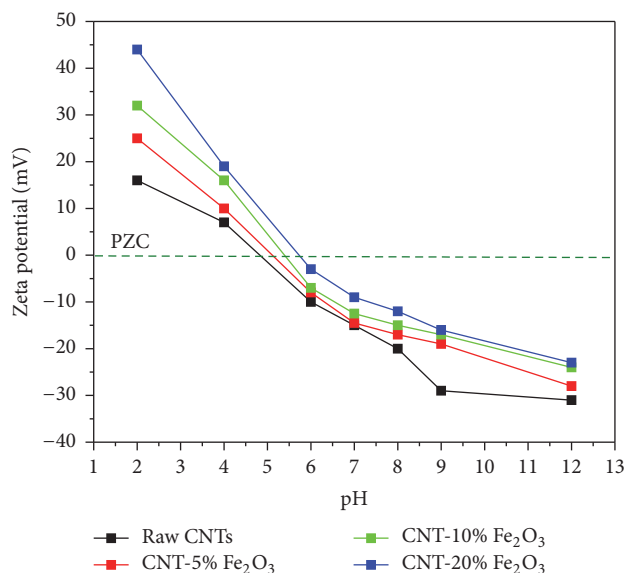


FIGURE 6: Zeta potential of raw CNTs and CNTs impregnated with 1%, 10%, and 20% Fe_2O_3 .

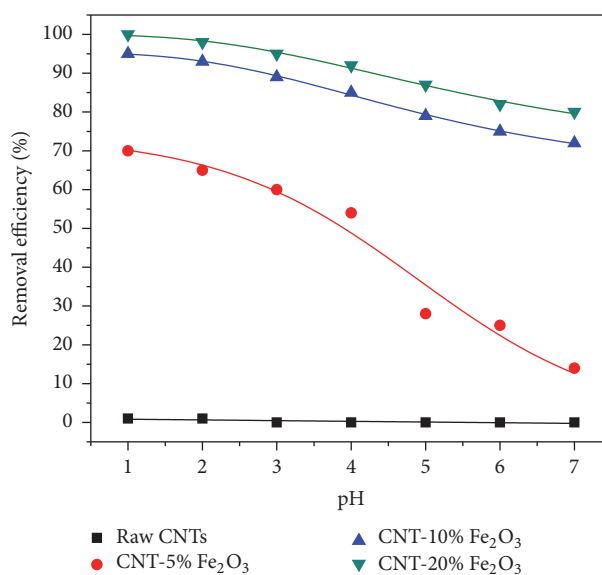


FIGURE 7: Effect of pH on the removal of selenium ions by raw and impregnated CNTs with different loading of iron oxide (agitation speed = 50 rpm, CNTs dosage = 10 mg, time = 6 hr, and initial concentration = 1 ppm).

trends in Figure 7 that vast improvement on the removal of Se from solution was achieved upon impregnating the surface of raw CNTs with iron oxide.

The percentage of iron oxide loading on the CNTs surface influenced the removal rate of Se. In general, it was observed at 20% loading rate that near 100% removal of Se was achieved compared to 93% and 65% for a loading rate of 10 and 5% iron oxide, respectively, at a pH of 1 for example. A number of factors may be attributed to this marked change. For example, the attachment of iron oxide particles onto the

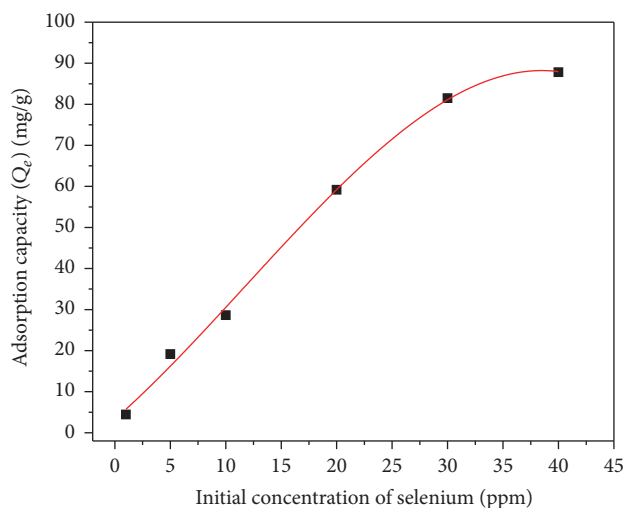


FIGURE 8: Effect of initial concentration of selenium on adsorption capacity of CNTs-20% iron oxide (agitation speed = 150 rpm, pH = 6, CNTs dosage = 10 mg, and time = 6 hr).

surface of CNTs may provide ample adsorption sites for the selenium ions to interact with. Also, it is well known that surfaces of metal oxides nanoparticles in aqueous solution are covered with hydroxyl groups [18]. Therefore, anion adsorption occurs by positive adsorbent surface charge (less negative sign compared to anion). Generally, increasing the pH causes decrease in the adsorbent surface charge and, accordingly, decreases in the adsorbent capacity [18, 39, 54]. As a result, when pH is increased the adsorbent surface is negatively charged (more negative sign) and leads to repulsion between negatively charged adsorbent particles and selenium anions. This repulsion causes termination of the adsorption process and also leads to the release of adsorbed selenium anions on surface of CNTs at higher pH to the water (desorption process). Based on the results reported in Figure 7, CNTs impregnated with 20 wt.% of iron oxide were selected in the later experiments to study the effects of other variables such as the initial Se concentration, CNTs dosage, contact time, and kinetics and isotherms models.

3.3. Effect of Initial Concentration. Figure 8 depicts the impact of initial Se concentration on the adsorption capacity of iron oxide impregnated CNTs. In general, the trend showed a marked increase of adsorption capacity with the increase in Se initial concentration. Figure 8 shows that at Se initial concentration between 5 and 20 ppm, the adsorption rate was steep and the adsorption was fast as can be seen from the slope of the first trend line. Above 20 ppm the adsorption slowed down and a plateau (second trend line) can be observed. The decline in the rate of adsorption at initial concentrations higher (as can be seen from the slope of the trend line) than 30 ppm (Figure 8) may be attributed to the saturation of all adsorption sites on the surface of CNTs. The higher adsorption capacity at higher Se concentration may be due to increase in the mass transfer (driving force) of selenium ions towards the iron oxide impregnated CNTs

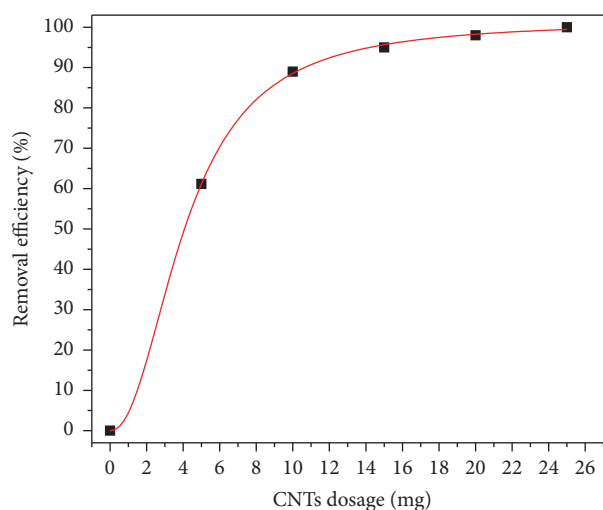


FIGURE 9: Effect of CNTs-20% iron oxide dosage on selenium removal (agitation speed = 150 rpm, pH = 6, time = 6 hr, and initial concentration = 1 ppm).

surfaces [18]. The highest adsorption capacity was about 88 mg/g at an initial Se concentration of 40 ppm as shown in Figure 8.

3.4. Effect of CNTs Dosage. The amount of CNTs added to the solution was varied between 5 and 25 mg in order to study the required optimum amount of adsorbent required to carry out the adsorption duty. In the experiments, the contact time, agitation speed, and pH were kept constant at 6 hr, 150 rpm, and 6, respectively. The experimental results are shown in Figure 9. Adsorption percentage (%) of selenium was plotted as a function of adsorbent dosage. Selenium ions adsorption was increased with increasing CNTs dosage due to the increase in the adsorption sites on CNTs surfaces resulting in the increase amount of adsorbed selenite ions. Selenium ions were completely removed from the solution using only 25 mg of CNTs. Therefore, the results show that the impregnated CNTs were suitable to adsorb selenium ions completely when there was sufficient CNTs surface area in the solution. Although the data was not shown here, the adsorption capacity was high at low dosages and keeps reducing at higher dosages. It is clearly agreed that as adsorbent dosage increases, the number of available adsorption sites increases, too. Alternatively, the decrease in adsorption capacity with increase in the adsorbent dosage is mostly related to the unsaturated nature of the adsorption sites through the adsorption process.

3.5. Effect of Contact Time. The effect of contact time on the adsorption of selenium ions is presented in Figure 10. It can be clearly seen that the rate of adsorption of selenium increased at initial period of contact time and then it decreased gradually with time until the adsorption reached an equilibrium point. The adsorption of selenium has increased rapidly during the first 30 minutes to reach about 65% removal. After that a slight increase was observed in the adsorption to

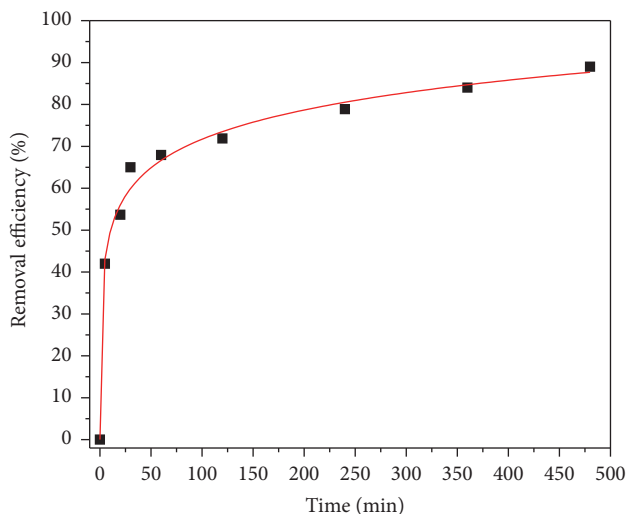


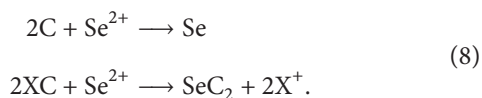
FIGURE 10: Effect of contact time on selenium removal (agitation speed = 150 rpm, pH = 6, CNTs dosage = 10 mg, and initial concentration = 1 ppm).

reach the maximum removal of selenium within four hours. The fast rate and then slow rate of adsorption suggest that selenium ions were first adsorbed on exterior surfaces of the CNTs during the initial time of contact. When the exterior surface gets saturated, the selenium ions diffused into the pores of the CNTs and were adsorbed at the interior surface of the CNTs.

3.6. Adsorption Kinetic Models. The modeling of the kinetics for selenium adsorption on CNTs was investigated using pseudo-first-order and pseudo-second-order kinetic models. Linearized plots of the two models are shown in Figure 11.

From Figure 11, the selenium adsorption on Fe₂O₃ impregnated CNTs does not fit very well to the pseudo-first-order model, as the R^2 values are less than 0.5. On the other hand, it does fit perfectly the pseudo-second-order model with R^2 value being almost 1. The rate constant for the 20% Fe₂O₃ loaded CNTs is found to be 0.016 g/mg·h.

The result obtained in this study is in good agreement with those reported in literature as most of the solid-liquid adsorption processes tend to conform to the pseudo-second-order model. Moreover, the pseudo-second-order model in this study can be defended by two-step linear relationship supporting the chemisorption nature of the process which is considered as rate-controlling mechanism as well [55]. The two-step linear mechanism between the composite CNTs (indicated as C and XC as activate adsorption site on CNTs) and Se ions is as follows:



As it was found in Figure 11, the adsorption is pseudo-second-order and the rate-limiting step is the chemical adsorption between Se ions and surface of CNTs through sharing or the exchange of electrons. Similar trends are reported for

TABLE 2: Parameters of Langmuir and Freundlich adsorption isotherm models of selenium.

Q_m (mg/g)	Langmuir			Freundlich	
	K_L (Lmg ⁻¹)	R^2	n	K_f (mg ^(1-1/n) L ^{1/n} g ⁻¹)	R^2
111	0.158	0.879	1.74	16	0.98

selenium ion adsorption in literature where the adsorption mechanism fit to pseudo-second-order model [38, 39].

3.7. Adsorption Isotherms Models. The adsorption data is modeled using the Freundlich and Langmuir isotherm models. As shown in Figure 12, the ability of the Freundlich model to fit the experimental data was studied by generating a plot of $\ln Q_e$ versus $\ln C_e$ with the intercept value of K_f and the slope of n . It can be observed from Table 3 and Figure 12 that Freundlich isotherm model best fit the data ($R^2 = 0.98$). From Figure 12(a) the Freundlich constants K_f and n for the CNTs were found to be 16 and 1.74, respectively. The value of n or slope of the fit is an indication of sorption intensity or surface heterogeneity. When the slope gets closer to zero, the system tends to become more heterogeneous and a value of the slope greater than unity implies a favorable process and indicative of cooperative sorption. Therefore, as value of n increases, the sorption process between selenium ion and CNTs is more favorable and this means there is better bonding between sorbent and selenium. However, the Langmuir isotherm model (Figure 12(a)) fit reasonably R^2 value of 0.879. The maximum adsorption capacity of the iron oxide impregnated CNTs, as predicted by isotherm model, was found to be 111 mg/g.

Interestingly, composite made of CNTs and iron oxide nanoparticle showed very superior adsorption capacity compared to each one of the mentioned adsorbent in Table 2, where the capacity could reach maximum of 111 mg/g for selenium removal. There are few factors which contributed to the very high adsorption capacity compared to other materials in Table 3. Superior surface area, high zeta potential, and special surface structure of CNTs suggest that CNTs have great potential for use as contaminant adsorbents in wastewater treatment. The only limiting factor which might affect usage of CNTs in the application such as environmental protection or water treatment is their production cost. It is not very far if we predict that the cost will further reduce by advancement in technology and CNTs then could be one of the potential for application such as water treatment.

4. Conclusions

The study revealed that CNTs impregnated with 20 wt.% of iron oxide showed 100% removal of selenium ions in 6 hours with an initial concentration of 1 ppm at pH 6, adsorbent dosage of 25 mg, and agitation speed of 150 rpm. The adsorption data very well fitted to the Freundlich model with maximum adsorption capacity of the iron oxide impregnated CNTs predicted by Langmuir isotherm model

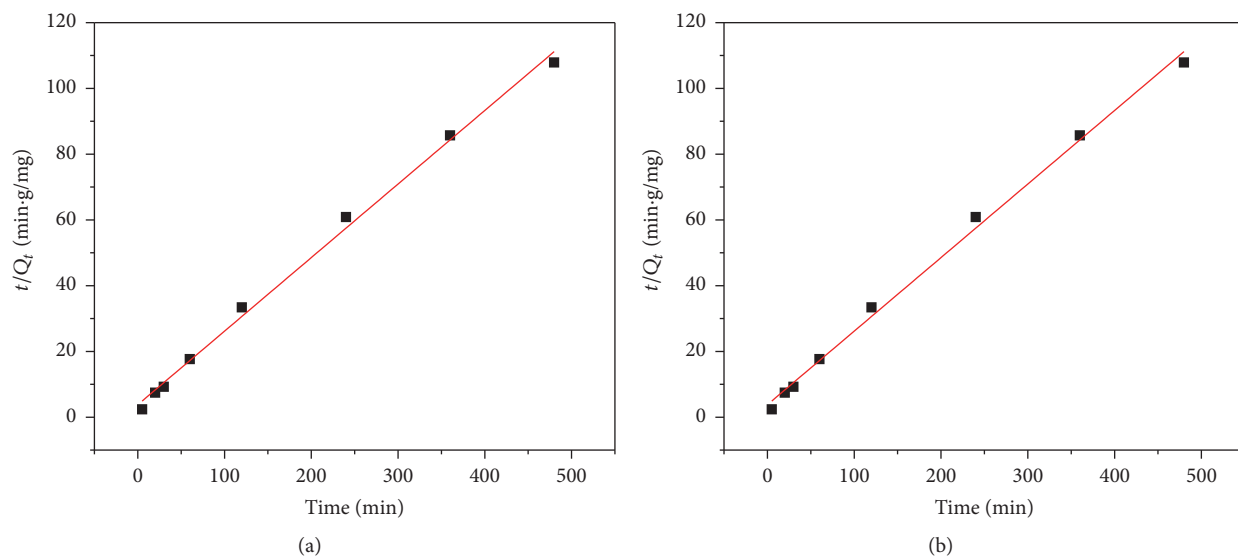


FIGURE 11: Adsorption kinetic for selenium removal: (a) pseudo-first-order and (b) pseudo-second-order model (agitation speed = 150 rpm, pH = 6, CNTs dosage = 10 mg, and initial concentration = 1 ppm).

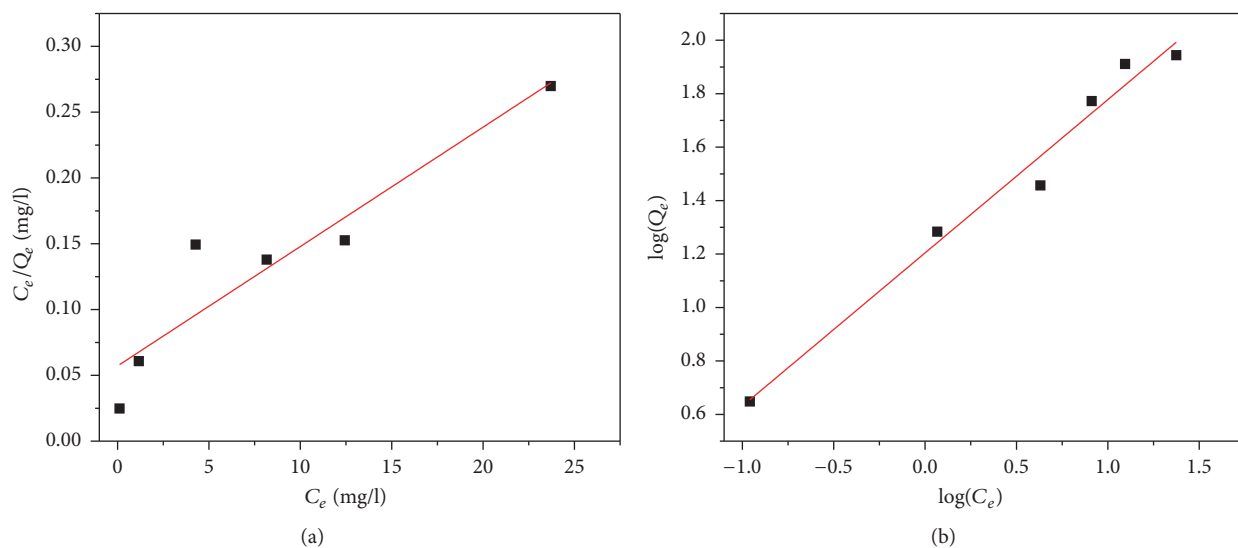


FIGURE 12: Adsorption isotherm models of selenium: (a) Langmuir and (b) Freundlich.

TABLE 3: Adsorption capacity of different materials for adsorption of selenium from water.

Type of adsorbent	Experimental conditions	Max. adsorption capacity (mg/g)	Reference
Iron oxide nanoparticle	pH = 4, initial concentration = 0.01 mg/L	15.1	[8]
Chitosan-clay composite	pH = 4, initial concentration = 0.1 mg/L, $T = 30^\circ\text{C}$	18.4	[15]
Iron-coated GAC	pH = 2-8, initial concentration = 2 mg/L, $T = 45^\circ\text{C}$	2.89	[38]
Nanocrystalline hydroxyapatite	pH = 5, initial concentration = 0.01 mg/L, $T = 30^\circ\text{C}$	1.94	[39]
Aluminum oxide coated sand	pH = 4.80, initial concentration = 1.2 mM	1.08	[40]
Sulfuric acid treated rice husk	pH = 1.5, initial concentration = 100 mg/L, $T = 45^\circ\text{C}$	40.92	[41]
Iron oxide impregnated CNTs	pH = 6, CNTs dosage = 10 mg and initial concentration = 1 ppm	111	This study

to be 111 mg/g. The date was correlated very well to pseudo-second-order kinetic model and rate of constant was found to be 0.016 g/mg·h. The highest adsorption capacity of iron oxide impregnated CNTs suggested that it can be employed effectively for the removal of selenium ions from water.

Conflicts of Interest

The authors declare that they have no conflicts of interest regarding the publication of this paper.

Acknowledgments

The authors would like to acknowledge the support provided by King Fahd University of Petroleum & Minerals (KFUPM) for sponsoring and funding this work.

References

- [1] J. Das, D. Das, G. P. Dash, and K. M. Parida, "Studies on Mg/Fe hydrotalcite-like-compound (HTlc): I. Removal of inorganic selenite (SeO_3^{2-}) from aqueous medium," *Journal of Colloid and Interface Science*, vol. 251, no. 1, pp. 26–32, 2002.
- [2] K. S. Dhillon and S. K. Dhillon, "Selenium in groundwater and its contribution towards daily dietary Se intake under different hydrogeological zones of Punjab, India," *Journal of Hydrology*, vol. 533, pp. 615–626, 2016.
- [3] J. Lessa, A. Araujo, G. Silva, L. Guilherme, and G. Lopes, "Adsorption-desorption reactions of selenium (VI) in tropical cultivated and uncultivated soils under Cerrado biome," *Chemosphere*, vol. 164, pp. 271–277, 2016.
- [4] H. Robberecht and R. Van Grieken, "Selenium in environmental waters: determination, speciation and concentration levels," *Talanta*, vol. 29, no. 10, pp. 823–844, 1982.
- [5] S. Santos, G. Ungureanu, R. Boaventura, and C. Botelho, "Selenium contaminated waters: an overview of analytical methods, treatment options and recent advances in sorption methods," *Science of the Total Environment*, vol. 521–522, no. 1, pp. 246–260, 2015.
- [6] L. C. Tan, Y. V. Nancharaiyah, E. D. van Hullebusch, and P. N. Lens, "Selenium: environmental significance, pollution, and biological treatment technologies," *Biotechnology Advances*, vol. 34, no. 5, pp. 886–907, 2016.
- [7] C. Hu, Q. Chen, G. Chen, H. Liu, and J. Qu, "Removal of Se(IV) and Se(VI) from drinking water by coagulation," *Separation and Purification Technology*, vol. 142, pp. 65–70, 2015.
- [8] G. Zelmannov and R. Semiat, "Selenium removal from water and its recovery using iron (Fe^{3+}) oxide/hydroxide-based nanoparticles sol (NanoFe) as an adsorbent," *Separation and Purification Technology*, vol. 103, pp. 167–172, 2013.
- [9] N. Rajamohan and M. Rajasimman, "Biosorption of Selenium using activated plant based sorbent—effect of variables, isotherm and kinetic modeling," *Biocatalysis and Agricultural Biotechnology*, vol. 4, no. 4, pp. 795–800, 2015.
- [10] H. G. Gorchev and G. Ozolins, "WHO guidelines for drinking-water quality," *WHO Chronicle*, vol. 38, no. 3, pp. 104–108, 2011.
- [11] G. Kallis and D. Butler, "The EU water framework directive: measures and implications," *Water Policy*, vol. 3, no. 2, pp. 125–142, 2001.
- [12] G. Gonzalez-Gil, P. N. L. Lens, and P. E. Saikaly, "Selenite reduction by anaerobic microbial aggregates: Microbial community structure, and proteins associated to the produced selenium spheres," *Frontiers in Microbiology*, vol. 7, article 571, 2016.
- [13] T. Kagami, T. Narita, M. Kuroda et al., "Effective selenium volatilization under aerobic conditions and recovery from the aqueous phase by *Pseudomonas stutzeri* NT-1," *Water Research*, vol. 47, no. 3, pp. 1361–1368, 2013.
- [14] L. C. Staicu, E. D. Van Hullebusch, M. A. Oturan, C. J. Ackerson, and P. N. L. Lens, "Removal of colloidal biogenic selenium from wastewater," *Chemosphere*, vol. 125, pp. 130–138, 2015.
- [15] N. Bleiman and Y. G. Mishael, "Selenium removal from drinking water by adsorption to chitosan-clay composites and oxides: batch and columns tests," *Journal of Hazardous Materials*, vol. 183, no. 1–3, pp. 590–595, 2010.
- [16] Y. Fu, J. Wang, Q. Liu, and H. Zeng, "Water-dispersible magnetic nanoparticle-graphene oxide composites for selenium removal," *Carbon*, vol. 77, pp. 710–721, 2014.
- [17] J. H. Kwon, L. D. Wilson, and R. Sammynaiken, "Sorptive uptake of selenium with magnetite and its supported materials onto activated carbon," *Journal of Colloid and Interface Science*, vol. 457, pp. 388–397, 2015.
- [18] A. W. Lounsbury, J. S. Yamani, C. P. Johnston, P. Lares-Casanova, and J. B. Zimmerman, "The role of counter ions in nano-hematite synthesis: implications for surface area and selenium adsorption capacity," *Journal of Hazardous Materials*, vol. 310, pp. 117–124, 2016.
- [19] L. D. Mafu, B. B. Mamba, and T. A. M. Msagati, "Synthesis and characterization of ion imprinted polymeric adsorbents for the selective recognition and removal of arsenic and selenium in wastewater samples," *Journal of Saudi Chemical Society*, vol. 20, no. 5, pp. 594–605, 2013.
- [20] V. C. Schwindt, J. S. Ardenghi, P. Bechthold et al., "Selenium adsorption at different coverages on Fe(100) and Fe(111): a DFT study," *Applied Surface Science*, vol. 315, no. 1, pp. 252–260, 2014.
- [21] M. Lenz and P. N. L. Lens, "The essential toxin: the changing perception of selenium in environmental sciences," *Science of the Total Environment*, vol. 407, no. 12, pp. 3620–3633, 2009.
- [22] M. O. M. Sharrad, H. Liu, and M. Fan, "Evaluation of FeOOH performance on selenium reduction," *Separation and Purification Technology*, vol. 84, pp. 29–34, 2012.
- [23] S. Klas and D. W. Kirk, "Understanding the positive effects of low pH and limited aeration on selenate removal from water by elemental iron," *Separation and Purification Technology*, vol. 116, pp. 222–229, 2013.
- [24] P. J. F. Harris, *Carbon Nanotube Science: Synthesis, Properties and Applications*, Cambridge University Press, Cambridge, UK, 2009.
- [25] D. Kang, X. Yu, M. Ge, F. Xiao, and H. Xu, "Novel Al-doped carbon nanotubes with adsorption and coagulation promotion for organic pollutant removal," *Journal of Environmental Sciences*, vol. 54, pp. 1–12, 2017.
- [26] A. K. Fard, G. Mckay, Y. Manawi, Z. Malaibari, and M. A. Hussien, "Outstanding adsorption performance of high aspect ratio and super-hydrophobic carbon nanotubes for oil removal," *Chemosphere*, vol. 164, pp. 142–155, 2016.
- [27] X. Liu, M. Wang, S. Zhang, and B. Pan, "Application potential of carbon nanotubes in water treatment: a review," *Journal of Environmental Sciences*, vol. 25, no. 7, pp. 1263–1280, 2013.
- [28] Ihsanullah, F. A. Al-Khalidi, B. Abu-Sharkh et al., "Effect of acid modification on adsorption of hexavalent chromium

- (Cr(VI)) from aqueous solution by activated carbon and carbon nanotubes," *Desalination and Water Treatment*, vol. 57, no. 16, pp. 7232–7244, 2016.
- [29] Y.-H. Li, J. Ding, Z. Luan et al., "Competitive adsorption of Pb^{2+} , Cu^{2+} and Cd^{2+} ions from aqueous solutions by multiwalled carbon nanotubes," *Carbon*, vol. 41, no. 14, pp. 2787–2792, 2003.
- [30] G. P. Rao, C. Lu, and F. Su, "Sorption of divalent metal ions from aqueous solution by carbon nanotubes: a review," *Separation and Purification Technology*, vol. 58, no. 1, pp. 224–231, 2007.
- [31] F. Yu, Y. Wu, J. Ma, and C. Zhang, "Adsorption of lead on multi-walled carbon nanotubes with different outer diameters and oxygen contents: kinetics, isotherms and thermodynamics," *Journal of Environmental Sciences*, vol. 25, no. 1, pp. 195–203, 2013.
- [32] N. M. M. Fourier, J. N. Sahu, E. C. Abdullah, and N. S. Jayakumar, "Rapid adsorption of toxic Pb(II) ions from aqueous solution using multiwall carbon nanotubes synthesized by microwave chemical vapor deposition technique," *Journal of Environmental Sciences*, vol. 45, pp. 143–155, 2016.
- [33] A. Abbas, B. A. Abussaud, Ihsanullah, N. A. H. Al-Baghli, M. Khraisheh, and M. A. Atieh, "Benzene removal by iron oxide nanoparticles decorated carbon nanotubes," *Journal of Nanomaterials*, vol. 2016, Article ID 5654129, 10 pages, 2016.
- [34] H. A. Asmaly, B. Abussaud, Ihsanullah et al., "Evaluation of micro- and nano-carbon-based adsorbents for the removal of phenol from aqueous solutions," *Toxicological and Environmental Chemistry*, vol. 97, no. 9, pp. 1164–1179, 2015.
- [35] Ihsanullah, H. A. Asmaly, T. A. Saleh, T. Laoui, V. K. Gupta, and M. A. Atieh, "Enhanced adsorption of phenols from liquids by aluminum oxide/carbon nanotubes: comprehensive study from synthesis to surface properties," *Journal of Molecular Liquids*, vol. 206, pp. 176–182, 2015.
- [36] H. Ding, X. Li, J. Wang, X. Zhang, and C. Chen, "Adsorption of chlorophenols from aqueous solutions by pristine and surface functionalized single-walled carbon nanotubes," *Journal of Environmental Sciences*, vol. 43, pp. 187–198, 2016.
- [37] A. Kayvani Fard, T. Rhadfi, G. Mckay et al., "Enhancing oil removal from water using ferric oxide nanoparticles doped carbon nanotubes adsorbents," *Chemical Engineering Journal*, vol. 293, pp. 90–101, 2016.
- [38] N. Zhang, L.-S. Lin, and D. Gang, "Adsorptive selenite removal from water using iron-coated GAC adsorbents," *Water Research*, vol. 42, no. 14, pp. 3809–3816, 2008.
- [39] S. Kongsri, K. Janpradit, K. Buapa, S. Techawongstien, and S. Chanthai, "Nanocrystalline hydroxyapatite from fish scale waste: preparation, characterization and application for selenium adsorption in aqueous solution," *Chemical Engineering Journal*, vol. 215–216, pp. 522–532, 2013.
- [40] W.-H. Kuan, S.-L. Lo, M. K. Wang, and C.-F. Lin, "Removal of Se(IV) and Se(VI) from water by aluminum-oxide-coated sand," *Water Research*, vol. 32, no. 3, pp. 915–923, 1998.
- [41] E. I. El-Shafey, "Sorption of Cd(II) and Se(IV) from aqueous solution using modified rice husk," *Journal of Hazardous Materials*, vol. 147, no. 1–2, pp. 546–555, 2007.
- [42] J. H. Lehman, M. Terrones, E. Mansfield, K. E. Hurst, and V. Meunier, "Evaluating the characteristics of multiwall carbon nanotubes," *Carbon*, vol. 49, no. 8, pp. 2581–2602, 2011.
- [43] I. W. Chiang, B. E. Brinson, A. Y. Huang et al., "Purification and characterization of single-wall carbon nanotubes (SWNTs) obtained from the gas-phase decomposition of CO (HiPco process)," *Journal of Physical Chemistry B*, vol. 105, no. 35, pp. 8297–8301, 2001.
- [44] R. Dobrowolski and M. Otto, "Preparation and evaluation of Fe-loaded activated carbon for enrichment of selenium for analytical and environmental purposes," *Chemosphere*, vol. 90, no. 2, pp. 683–690, 2013.
- [45] M. Duc, G. Lefèvre, and M. Fédoroff, "Sorption of selenite ions on hematite," *Journal of Colloid and Interface Science*, vol. 298, no. 2, pp. 556–563, 2006.
- [46] K.-H. Goh and T.-T. Lim, "Geochemistry of inorganic arsenic and selenium in a tropical soil: effect of reaction time, pH, and competitive anions on arsenic and selenium adsorption," *Chemosphere*, vol. 55, no. 6, pp. 849–859, 2004.
- [47] F. Monteil-Rivera, M. Fedoroff, J. Jeanjean, L. Minel, M.-G. Barthes, and J. Dumonceau, "Sorption of selenite (SeO_3^{2-}) on hydroxyapatite: an exchange process," *Journal of Colloid and Interface Science*, vol. 221, no. 2, pp. 291–300, 2000.
- [48] A. Manceau and L. Charlet, "The mechanism of selenate adsorption on goethite and hydrous ferric oxide," *Journal of Colloid And Interface Science*, vol. 168, no. 1, pp. 87–93, 1994.
- [49] K. F. Hayes, C. Papelis, and J. O. Leckie, "Modeling ionic strength effects on anion adsorption at hydrous oxide/solution interfaces," *Journal of Colloid And Interface Science*, vol. 125, no. 2, pp. 717–726, 1988.
- [50] Y. Tianmeng, B. Liu, and J. Liu, "Adsorption of selenite and selenate by metal oxides studied with fluorescent DNA probes for analytical application," *Journal of Analysis and Testing*, vol. 1, article 2, 2017.
- [51] Z. Nie, N. Finck, F. Heberling, T. Pruessmann, C. Liu, and J. Lutzenkirchen, "Adsorption of selenium and strontium on Goethite: an EXAFS study and surface complexation modeling of the ternary systems," *Environmental Science and Technology*, vol. 51, no. 7, pp. 3751–3758, 2017.
- [52] S. O. Adio, M. H. Omar, M. Asif, and T. A. Saleh, "Arsenic and Selenium removal from water using Biosynthesized Nanoscale zero-valent iron: a factorial design analysis," *Process Safety and Environmental Protection*, vol. 107, pp. 518–527, 2017.
- [53] M. Min, C. Shen, L. Fang et al., "Design of a selective regenerable cellulose microcolumn for selenium efficient recovery and economic determination," *Chemical Engineering Research and Design*, vol. 117, pp. 7773–783, 2017.
- [54] D. S. Han, B. Batchelor, and A. Abdel-Wahab, "Sorption of selenium(IV) and selenium(VI) to mackinawite (FeS): effect of contact time, extent of removal, sorption envelopes," *Journal of Hazardous Materials*, vol. 186, no. 1, pp. 451–457, 2011.
- [55] Y. S. Ho and G. McKay, "Pseudo-second order model for sorption processes," *Process Biochemistry*, vol. 34, no. 5, pp. 451–465, 1999.

Research Article

A Comparative Study of Raw and Metal Oxide Impregnated Carbon Nanotubes for the Adsorption of Hexavalent Chromium from Aqueous Solution

Muhammad I. Qureshi,¹ Faheemuddin Patel,² Nadhir Al-Baghli,¹ Basim Abussaud,¹ Bassam S. Tawabini,³ and Tahar Laoui²

¹Department of Chemical Engineering, KFUPM, Dhahran 31261, Saudi Arabia

²Department of Mechanical Engineering, KFUPM, Dhahran 31261, Saudi Arabia

³Department of Geosciences, KFUPM, Dhahran 31261, Saudi Arabia

Correspondence should be addressed to Tahar Laoui; tlouai@kfupm.edu.sa

Received 13 February 2017; Revised 12 March 2017; Accepted 16 March 2017; Published 10 April 2017

Academic Editor: Viktor Kochkodan

Copyright © 2017 Muhammad I. Qureshi et al. This is an open access article distributed under the Creative Commons Attribution License, which permits unrestricted use, distribution, and reproduction in any medium, provided the original work is properly cited.

The present study reports the use of raw, iron oxide, and aluminum oxide impregnated carbon nanotubes (CNTs) for the adsorption of hexavalent chromium (Cr(VI)) ions from aqueous solution. The raw CNTs were impregnated with 1% and 10% loadings (weight %) of iron oxide and aluminum oxide nanoparticles using wet impregnation technique. The synthesized materials were characterized using scanning electron microscopy (SEM) and thermogravimetric analysis (TGA). Batch adsorption experiments were performed to assess the removal efficiency of Cr(VI) ions from water and the effects of pH, contact time, adsorbent dosage, and initial concentration of the Cr(VI) ions were investigated. Results of the study revealed that impregnated CNTs achieved significant increase in the removal efficiency of Cr(VI) ions compared to raw CNTs. In fact, both CNTs impregnated with 10% loading of iron and aluminum oxides were able to remove up to 100% of Cr(VI) ions from aqueous solution. Isotherm studies were carried out using Langmuir and Freundlich isotherm models. Adsorption kinetics of Cr(VI) ions from water was found to be well described by the pseudo-second-order model. The results suggest that metallic oxide impregnated CNTs have very good potential application in the removal of Cr(VI) ions from water resulting in better environmental protection.

1. Introduction

Chromium is mainly found in natural deposits as ores and other compounds such as chrome ochre (Cr_2O_3), crocoite (PbCrO_4), and ferric chromite (FeCr_2O_4). It is the sixth most abundant transition metal [1, 2]. Chromium is discharged into water bodies from a number of industrial sources such as electroplating and metal cleaning, leather tanning, mining of chrome ore, production of steel and alloys, dyes and pigments, glass industry, wood preservation, and textile industry [2–5].

Chromium is found in different oxidation states such as 2+, 3+, and 6+. In water, it can exist in the form of chromate ion (CrO_4^{2-}), chromic acid (H_2CrO_4), hydrogen

chromate ion (HCrO_4^-), and dichromate ion ($\text{Cr}_2\text{O}_7^{2-}$) [6–8]. However, the hexavalent Cr(VI) and trivalent Cr(III) are the two most stable forms present in water in neutral pH range.

The typical concentration of chromium in industrial water ranges from 5.2 to 208,000 mg/L [9, 10]. The maximum allowable limits of chromium in drinking water are 0.05 and 0.1 mg/L, as suggested by the World Health Organization (WHO) and US Environmental Protection Agency (EPA), respectively [11–15].

Due to its carcinogenic and mutagenic nature, Cr(VI) is considered as almost 300 times more toxic than Cr(III) [16]. The toxic effects of Cr(VI) include liver and kidney damage, nausea, dermatitis, diarrhea, vomiting, internal hemorrhage,

and repository problems (asthma). Eye and skin contact may cause permanent damage to eye, severe burn, irritation, ulceration, and nasal septum [17, 18].

A number of remediation techniques have been reported to get rid of the Cr(VI) from water including solvent extraction [19], floatation [20], coagulation [21], ion exchange [22–25], membrane technologies [26, 27], adsorption [6, 7, 28] and cyanide treatment [29], and reduction followed by chemical precipitation [30]. However, adsorption is the most versatile, cost effective, and widely used method for removal of different contaminants from water including heavy metals. In the literature, different adsorbents have been reported for the removal of Cr(VI) from water including anaerobic sludge [31], lignocellulosic solid wastes [32], carbon slurry [33], waste slurry [34], agricultural wastes [35], cow dung carbon [36], corncob [37], almond shell carbon [38], zeolite [39], hazelnut shell carbon [40, 41], rice Polish [42], sphagnum moss peat [43], apple residue [44], moss [45], rice husk carbon [46], fly ash [6, 47], pine needles, charcoal, wool, olive stone/cake, cactus [48], used tyre carbon [49], coconut tree sawdust carbon [50], sawdust [51], dust coal, coconut shell and wood activated carbons [52], clay [53], palm pressed fibers and coconut husk [54], activated groundnut husk carbon [55], polyaniline coated on sawdust [56], coniferous leaves [57], leaf mould [58], wheat bran [59], sugar beet pulp [60], seaweeds [61], tannin gel particles [62], seaweed biosorbent [63], chitosan-1,2-cyclohexylenedinitrilotetraacetic acid–graphene oxide (Cs/CDTA/GO) nanocomposite [64], paper mill sludge [65], hydrous concrete particles [66], waste tea [67], activated alumina, rice husk ash, neem bark, saw dust, fuller's earth [6], eucalyptus bark, activated charcoal, and charred rice husk [68], treated waste newspaper [69], and graphene oxide (GO) [70].

Recently, carbon nanotubes (CNTs) have emerged as a novel adsorbent for the removal of various contaminants from water. CNTs offer the advantages of high porous and hollow structure, light mass density, large surface, and strong interaction with the pollutant molecules [28]. Studies have confirmed that surface modification of CNTs significantly enhanced their adsorption capability for the removal of various contaminants from water [71–76].

In the present study, raw CNTs and CNTs impregnated with iron oxide and aluminum oxide nanoparticles were used for the adsorption of Cr(VI) from water. The synthesized materials were characterized using scanning electron microscopy (SEM) and thermogravimetric analysis (TGA). Batch adsorption experiments were performed and the effect of pH, contact time, adsorbent dosage, and initial concentration of the adsorbate on the removal efficiency of Cr(VI) from water was investigated. Isotherm studies were carried out using Langmuir and Freundlich isotherm models.

2. Experimental

2.1. Materials Preparation. Raw CNTs were acquired from Chengdu Organic Chemicals Co. Ltd. (China), with the following characteristics: 95% purity, outside diameter of 10–20 nm, and length ranging from 1 to 10 μm . These raw

CNTs were impregnated with 1% and 10% loadings (weight %) of iron oxide and aluminum oxide nanoparticles using wet impregnation technique. Specific amount of CNTs was added in ethanol and sonicated to achieve homogenous dispersion of CNTs. Specific amount of metallic salt dissolved separately in ethanol and was sonicated, and then the resultant solution was added dropwise to the CNTs dispersed in ethanol. This dispersion was sonicated for proper mixing with CNTs and subsequently heated at 80–90°C in an oven overnight to evaporate the ethanol. On complete drying, the CNTs were calcined in a furnace at 350°C for 4 hours. This process resulted in the attachment of metal oxide nanoparticles onto the surface of CNTs.

2.2. Characterization of the Adsorbents. Raw and impregnated CNTs were characterized using various techniques. In order to perform morphological and elemental analysis, samples were coated with about 5 nm thick layer of platinum using Quorum sputter coater (Model: Q150R S). Scanning electron microscope (Model: TESCAN MIRA 3 FEG-SEM) was used to analyze the morphology and structure of raw and metal oxide impregnated CNTs. Thermogravimetric analysis (TGA) of raw and impregnated CNTs was performed using TA Instrument (Model: SDTQ600), in order to evaluate the purity and thermal degradation of materials. Samples were heated to 900°C in air, at heating rate of 10°C/min and air flow rate of 100 mL/min.

2.3. Batch-Mode Adsorption Experiment. Batch experiments were performed to study the effect of various parameters on the adsorption of Cr(VI) ions by raw and metal oxide impregnated CNTs at room temperature.

The effect of pH, contact time, agitation speed, and adsorbent dosage was investigated on the removal of Cr(VI) ions from aqueous solution. Concentration of Cr(VI) ions was measured using inductively coupled plasma mass spectrometer (Thermo-Fisher, X-Series 2 Q-ICP-MS).

Percentage removal and adsorption capacity were calculated using (1) and (2), respectively:

$$\text{Removal efficiency (\%)} = \frac{C_o - C_t}{C_o} * 100 \quad (1)$$

$$\text{Adsorption capacity (q)} = \frac{(C_o - C_t)V}{m}, \quad (2)$$

where “ C_o ” is the initial concentration (ppm) at start of the experiment ($t = 0$), while “ C_t ” is the concentration at time “ t ”. “ V ” is the volume (L) of the solution and “ m ” represents the amount (g) of the adsorbent dosage. For the batch adsorption experiments, the stock solution was prepared using the same methodology reported previously [73].

3. Results and Discussion

3.1. Characterization of Raw and Metal Oxide Impregnated CNTs. Surface morphologies of the raw and metal oxide impregnated CNTs were observed using SEM.

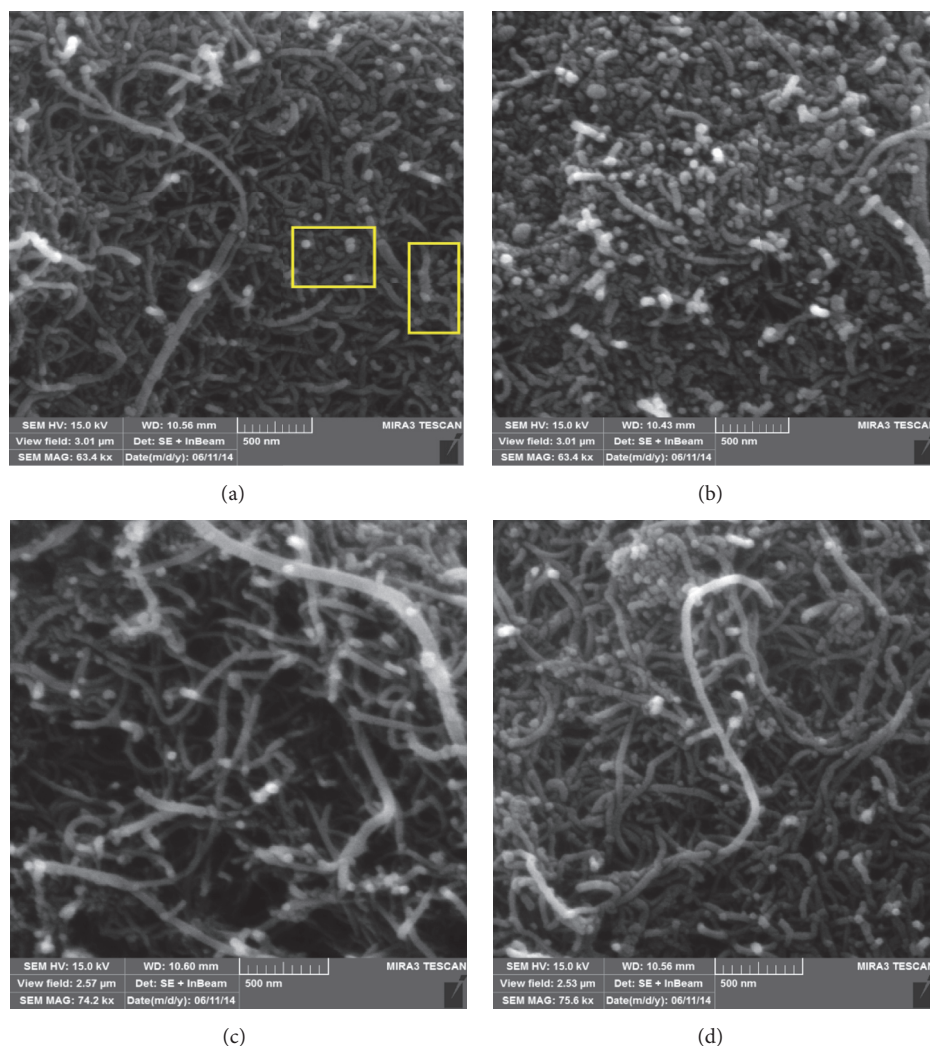


FIGURE 1: SEM images of CNTs with (a) 1% iron oxide (boxes indicate the iron oxide nanoparticles impregnated on CNTs), (b) 10% iron oxide, (c) 1% aluminum oxide, and (d) 10% aluminum oxide.

Figure 1 shows the SEM images for the metal oxides impregnated CNTs. Tubular geometry of the CNTs was observed and no damage was noticed in CNTs structures after impregnation. Metal oxide nanoparticles (highlighted in the box) were clearly observed on the surface of CNTs as displayed in Figures 1(a)–1(d). CNTs were properly dispersed for the low loading of 1% metal oxide (Figures 1(a) and 1(c)); however, at higher loading (10%) a little agglomeration of metal oxide particles could be seen in Figures 1(b) and 1(d). In general, the dispersion of CNTs was improved after impregnation with metal oxide nanoparticles. Metal oxide nanoparticles might help reduce the strong Van der Waals forces between CNTs leading to their improved dispersion.

TGA curves for raw and metal oxide impregnated CNTs are presented in Figure 2. CNTs were heated to 900°C at a rate of 10°C/min under air. All the TGA curves have two main weight loss regions. Initial small weight loss was attributed to the evaporation of physically bound water and some other lighter impurities. The second, steep, and rapid weight loss region represents the combustion of CNTs. Raw CNTs

showed more stability and started degrading around 550°C while degradation of 1% and 10% metal oxide impregnated CNTs started around 450°C and 500°C, respectively. This may be due to the fact that the impregnation of metal oxide nanoparticles on CNTs serves as an impurity hence leading to steep weight loss at lower temperature [77]. The weight of the residue left at the end of the analysis is the indication of metallic oxide nanoparticles. It can be observed that the amount of residue left was higher for the CNTs with 10% metal oxide loading as compared to raw CNTs and CNTs with 1% metal oxide loadings.

3.2. Effect of pH. The removal of Cr(VI) ions by raw and metal oxide impregnated CNTs, as a function of pH, is presented in Figure 3. Solution pH was varied from 3 to 8, while the other variables including adsorbent dosage, contact time, agitation speed, and Cr(VI) initial concentration were kept constant at 200 mg, 2 hours, 50 mg, 200 rpm, and 1 mg/L, respectively.

A maximum removal of Cr(VI) was achieved at pH 3, while the removal was observed to decrease with increase in

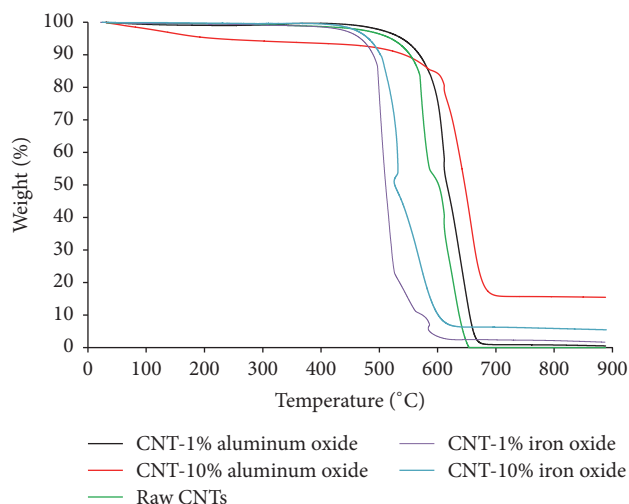


FIGURE 2: TGA curves for raw and metal oxide impregnated CNTs.

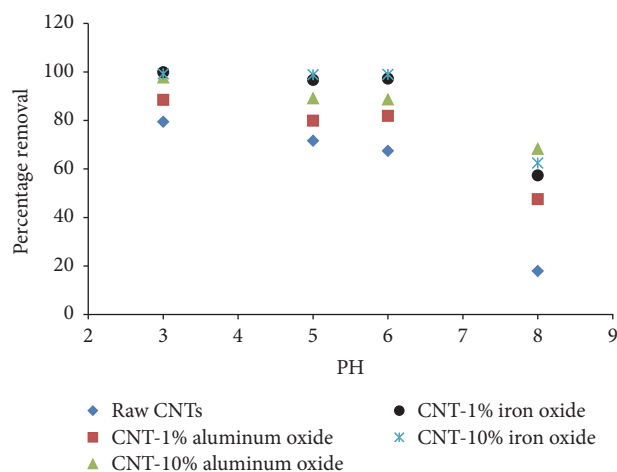
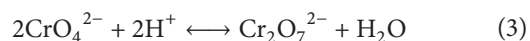


FIGURE 3: Effect of pH on the percentage removal of Cr(VI) (initial concentration = 1 mg/L, agitation speed = 200 rpm, adsorbent dosage = 200 mg, and time = 2 hours).

pH, for all the adsorbents. This phenomenon can be explained on the basis of surface charge of the adsorbents and ionic chemistry of the solution.

Chromium ions may exist in the form of chromate (CrO_4^{2-}), dichromate ($\text{Cr}_2\text{O}_7^{2-}$), and hydrogen chromate (HCrO_4^-), depending upon the solution pH and chromate concentration.

The equilibrium between the chromate (CrO_4^{2-}) and dichromate ions ($\text{Cr}_2\text{O}_7^{2-}$) in aqueous solution is represented by (3) [15, 73].



Chromate (CrO_4^{2-}) ions are the dominant species at high pH values, while, at low pH, mainly dichromate ions ($\text{Cr}_2\text{O}_7^{2-}$) exist in the solution [78, 79].

At low pH, the high removal of Cr(VI) ions is attributed to the electrostatic interaction between the $\text{Cr}_2\text{O}_7^{2-}$ anions and positively charged CNTs surface. However, at high

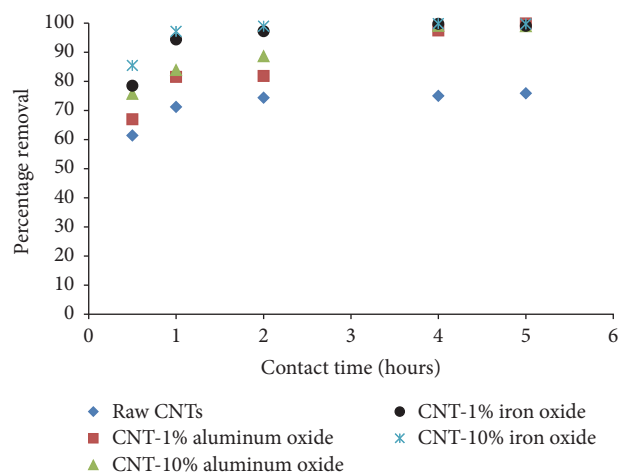


FIGURE 4: Effect of contact time on percentage removal of Cr(VI). (Initial concentration = 1 mg/L, agitation speed = 200 rpm, adsorbent dosage = 200 mg, pH = 6).

pH, surfaces of the CNTs carry more negative charges and repulsion between the CrO_4^{2-} ions and the CNTs surfaces resulted in lower removal of Cr(VI) ions. Furthermore, the low removal might also be due to competition between the OH^- and chromate (CrO_4^{2-}) ions over the limited adsorption sites as well as due to precipitation of $\text{Cr}(\text{OH})_3$ that might occur at high pH (here at pH = 8) [73].

Surface impregnation of CNTs with metal oxide was observed to enhance the removal efficiency. The maximum removal of 87.8% was obtained for CNT with 10% aluminum oxide loading at pH 3. Raw CNTs were still able to remove almost 74% Cr(VI) ions at same pH and under similar experimental conditions. Although the maximum removal was obtained at pH 3, however, to evaluate the potential of the adsorbents in real water treatment applications, a pH value of 6 was selected for the remaining experiments.

Because the solution pH has a significant effect on the removal of Cr(VI) ions, we may deduce that the main mechanism is electrostatic interaction. The net surface charge of the adsorbent changes with pH and affects the removal of Cr(VI). In addition to electrostatic interaction, some physical adsorption of Cr(VI) ions is expected on the surfaces of the CNTs due to Van der Waals interactions. Studies also suggest that strong surface complexation and ion exchange are the main mechanisms involved during the adsorption of Cr(VI) ions on CNTs surface [80].

3.3. Effect of Contact Time. The experimental results presenting the effect of time on the removal of Cr(VI) ions by raw and metal oxide impregnated CNTs are shown in Figure 4. Contact time was varied from 0.5 to 5 hours while the solution pH, Cr(VI) initial concentration, adsorbent dosage, and agitation speed were kept constant at 6, 1 mg/L, 200 mg, and 200 rpm, respectively.

It is obvious that Cr(VI) ions removal has improved significantly as the contact time increased from 0.5 to 4 hours. No significant increase in removal was observed after 4 hours of contact time indicating the reach of equilibrium.

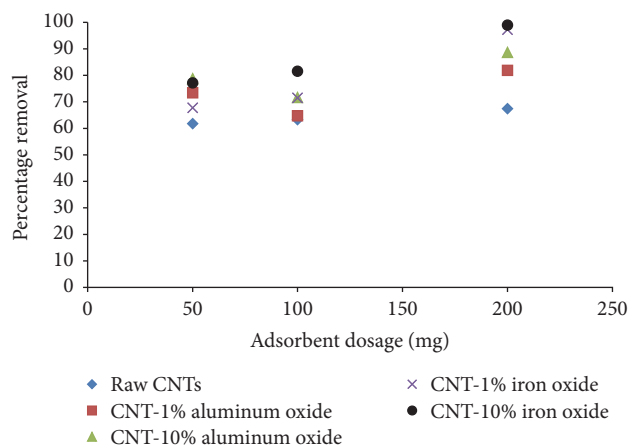


FIGURE 5: Effect of adsorbent dosage on percentage removal of Cr(VI) (initial concentration = 1 mg/L, agitation speed = 200 rpm, contact time = 2 hours, and pH = 6).

It was observed that CNTs impregnated with metal oxide were able to remove more than 97% of Cr(VI) ions after 2 hours of contact time (for CNTs impregnated with iron oxide) and almost 100% after 4 hours of contact time (for CNTs impregnated with both iron and aluminum oxides).

3.4. Effect of Adsorbent Dosage. The effect of adsorbent dosage on the removal of Cr(VI) ions is depicted in Figure 5. The adsorbent dosage was varied from 50 to 200 mg, while solution pH, contact time, initial concentration of Cr(VI), and agitation speed were kept constant at 6, 2 hours, 1 mg/L, and 200 rpm, respectively.

A direct relationship was observed between the adsorbent dosage and the removal of Cr(VI) ions for all adsorbents. The removal was observed to increase with increase in the adsorbent dosage and the maximum removal was recorded at 200 mg dosage. With increase in the adsorbent dosage, the number of active sites increases; hence more Cr(VI) ions can be adsorbed onto the adsorbent surface. At 200 mg dosage, CNTs with 10% loading of iron oxide yielded a maximum removal of 99% of Cr(VI) ions, as compared to raw CNTs yielding about 67% removal under similar experimental conditions. These results confirmed that metal oxide loading has a significant effect on the removal efficiency of the raw CNTs.

3.5. Effect of Agitation Speed. Agitation speed is an important parameter that effects and enhances the dispersion of the adsorbent in the solution and reduces the agglomeration. For the two loadings of metal oxides (1% and 10%) used in the present study, the CNTs were found to properly disperse in the solution and no significant agglomeration was observed. Figure 6 displays the effect of agitation speed on the removal of Cr(VI) ions by raw and metal oxides impregnated CNTs. The agitation speed was varied from 50 to 200 rpm, while the solution pH, initial concentration, adsorbent dosage, and contact time were kept constant at 6, 1 mg/L, 200 mg, and 2 hours, respectively. The removal of Cr(VI) ions was observed to increase with increase in agitation speed for all considered

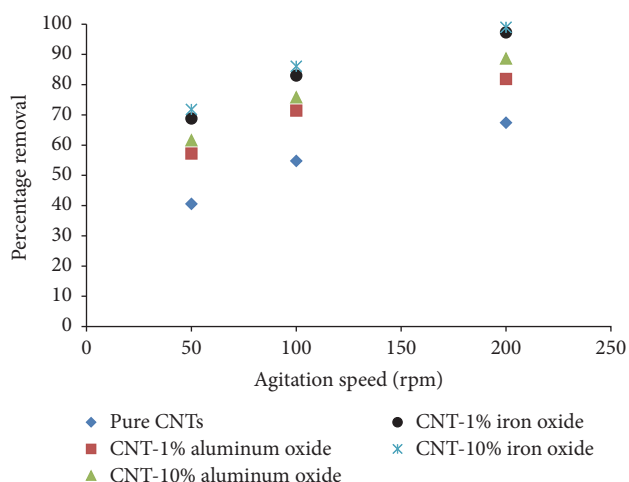


FIGURE 6: Effect of agitation speed on percentage removal of Cr(VI) ions (initial concentration = 1 mg/L, adsorbent dosage = 200 mg, contact time = 2 hours, and pH = 6).

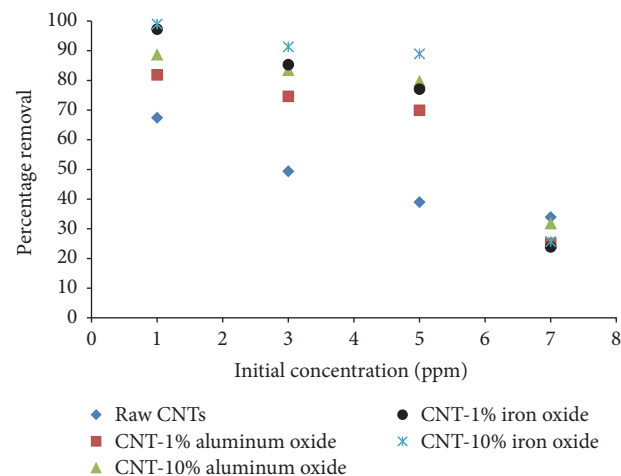


FIGURE 7: Effect of initial concentration on percentage removal of Cr(VI) (adsorbent dosage = 200 mg, contact time = 2 hours, agitation speed = 200 rpm, and pH = 6).

adsorbents. This is due to the fact that agitation facilitates effective diffusion of ions towards the adsorbent surface [73]. At 200 rpm speed, CNTs with 10% loading of iron oxide were able to remove 99% Cr(VI) ions.

3.6. Effect of Initial Concentration. The removal of Cr(VI) ions was also dependent on the initial concentration of Cr(VI) as shown in Figure 7. The initial concentration was varied from 1 to 7 ppm, while the solution pH, agitation speed, adsorbent dosage, and contact time were kept constant at 6, 200 rpm, 200 mg, and 2 hours, respectively. The maximum removal was achieved at low dosage concentration and the removal was observed to decrease with increase in concentration for all adsorbents. This might be due to the fact that, at high concentration, the adsorption sites are saturated due to availability of surplus Cr(VI) ions. At 1 ppm dosage, a maximum removal 99% of Cr(VI) ions was achieved with CNTs with 10% loading of iron oxide.

TABLE 1: Parameters of Langmuir and Freundlich isotherm models for chromium.

Adsorbent	Freundlich			Langmuir	
	n	K_F (L/mg)	R^2	K_L (L/mg)	R^2
CNT-iron oxide	7.922564	0.628705	0.9980	-7.47535	0.9966
CNT-aluminum oxide	3.907029	0.571687	0.9996	-10.9559	0.9855
Raw CNTs	2.110755	0.291322	0.9975	0.756502	0.9859

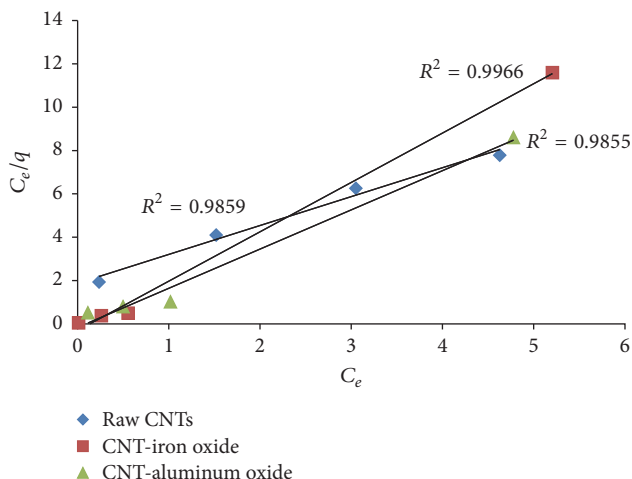


FIGURE 8: Langmuir adsorption model for Cr(VI).

3.7. *Freundlich and Langmuir Isotherm Models.* Adsorption equilibrium data was fitted by Langmuir and Freundlich models. Langmuir model best describes the monolayer adsorption while Freundlich model provides information about heterogeneous adsorption on adsorbent surface [81].

Representative equations of the isotherm models are presented below.

Langmuir isotherm model:

$$q_e = \frac{q_m K_L C_e}{1 + K_L C_e}; \quad (4)$$

Freundlich isotherm model:

$$q_e = K_F C_e^{1/n}, \quad (5)$$

where C_e and q_e are the concentrations of contaminants in water and in adsorbent at the adsorption equilibrium, respectively. q_m is the maximum adsorption capacity; K_L is the adsorption equilibrium constant of Langmuir model; K_F and n are Freundlich constants related to the adsorption capacity and surface heterogeneity of the adsorbents, respectively.

Figures 8 and 9 show Langmuir and Freundlich adsorption isotherm models for Cr(VI), respectively, while adsorption parameters and regression data of the models are presented in Table 1. It can be seen that both Langmuir and Freundlich isotherm models show a good fit for both raw and metal oxide impregnated CNTs. However, the value of regression coefficient (R^2) value for Freundlich isotherm model is slightly higher than Langmuir isotherm model.

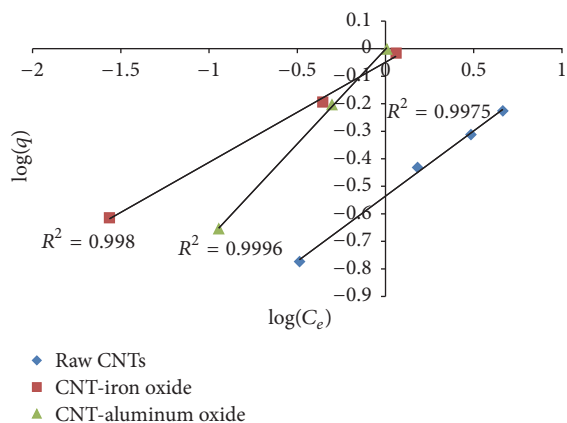


FIGURE 9: Freundlich adsorption model for Cr(VI).

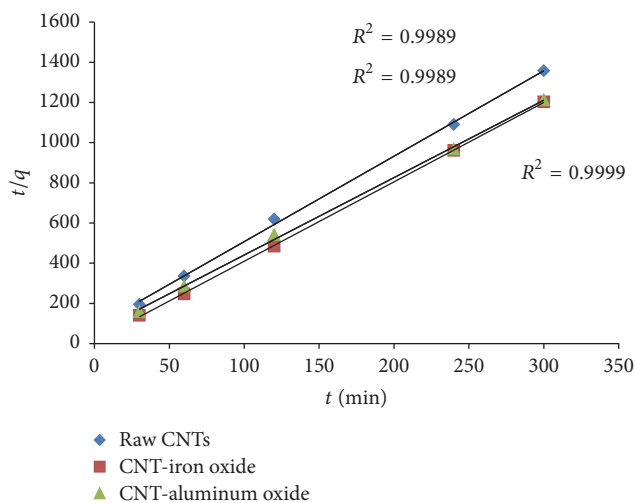


FIGURE 10: Pseudo-second-order kinetics for the adsorption of Cr(VI).

3.8. *Kinetics Modeling.* Adsorption kinetic is one of the most important factors that govern the solute uptake rate and represents the adsorption efficiency of the adsorbent. The pseudo-second-order model was used to model the kinetics of adsorption.

Representative equation of pseudo-second-order model is provided below:

$$\frac{t}{q_t} = \frac{1}{k_2 q_e^2} + \frac{t}{q_e}. \quad (6)$$

Figure 10 represents the fitting of experimental data with the pseudo-second-order model. Table 2 provides the results of

TABLE 2: Parameters of pseudo-second-order kinetic model for chromium.

Adsorbent	q_e (mg/g)	k_2 (mg g ⁻¹ min ⁻¹)	R^2
CNT-iron oxide	0.253062	0.534162	0.9999
CNT-aluminum oxide	0.259575	0.133789	0.9989
Raw CNTs	0.235297	0.109363	0.9989

the kinetics model fittings for the adsorption of Cr(VI) using raw and metal oxide impregnated CNTs.

It can be seen from Figure 10 and Table 2 that the correlation coefficient (R^2) of pseudo-second-order kinetic equation is sufficiently high for all the adsorbents. Therefore, the process of Cr(VI) removal using raw and metal oxide impregnated CNTs can be well described by the pseudo-second-order model.

4. Conclusion

Raw, iron oxide, and aluminum oxide impregnated carbon nanotubes (CNTs) were found to be effective adsorbents for the removal of Cr(VI) ions from aqueous solution. The removal of Cr(VI) ions was strongly dependent on pH, contact time, adsorbent dosage, and initial concentration of the Cr(VI) ions. Solution pH was found to be a critical parameter affecting the adsorption of Cr(VI) ions, in comparison with the other parameters. The removal of Cr(VI) ions was observed to decrease with increase in pH of the solution. It was observed that both CNTs impregnated with 10% of iron and aluminum oxides were able to remove almost 100% of Cr(VI) ions at solution pH 6, Cr(VI) initial concentration of 1 mg/L, adsorbent dosage of 200 mg, agitation speed of 200 rpm, and contact time of 4 hours. The prepared materials were found to exhibit high removal efficiency at pH 6 suggesting their great potential in real water treatment applications.

Conflicts of Interest

The authors declare that there are no conflicts of interest regarding the publication of this paper.

Acknowledgments

The authors would like to acknowledge the support provided by the Deanship of Scientific Research (DSR) at King Fahd University of Petroleum and Minerals (KFUPM) for funding this work through Project no. IN131065.

References

- [1] D. Mohan and C. U. Pittman Jr., "Activated carbons and low cost adsorbents for remediation of tri- and hexavalent chromium from water," *Journal of Hazardous Materials*, vol. 137, no. 2, pp. 762–811, 2006.
- [2] B. M. Weckhuysen, I. E. Wachs, and R. A. Schoonheydt, "Surface chemistry and spectroscopy of chromium in inorganic oxides," *Chemical Reviews*, vol. 96, no. 8, pp. 3327–3349, 1996.
- [3] S. Kalidhasan, M. Ganesh, S. Sricharan, and N. Rajesh, "Extractive separation and determination of chromium in tannery effluents and electroplating waste water using tribenzylamine as the extractant," *Journal of Hazardous Materials*, vol. 165, no. 1–3, pp. 886–892, 2009.
- [4] J. R. Rao, P. Thanikaivelan, K. J. Sreeram, and B. U. Nair, "Green route for the utilization of chrome shavings (chromium-containing solid waste) in tanning industry," *Environmental Science and Technology*, vol. 36, no. 6, pp. 1372–1376, 2002.
- [5] S. Vasudevan, G. Sozhan, S. Mohan, R. Balaji, P. Malathy, and S. Pushpavanam, "Electrochemical regeneration of chromium containing solution from metal finishing industry," *Industrial and Engineering Chemistry Research*, vol. 46, no. 9, pp. 2898–2901, 2007.
- [6] A. K. Bhattacharya, T. K. Naiya, S. N. Mandal, and S. K. Das, "Adsorption, kinetics and equilibrium studies on removal of Cr(VI) from aqueous solutions using different low-cost adsorbents," *Chemical Engineering Journal*, vol. 137, no. 3, pp. 529–541, 2008.
- [7] D. Mohan, K. P. Singh, and V. K. Singh, "Removal of hexavalent chromium from aqueous solution using low-cost activated carbons derived from agricultural waste materials and activated carbon fabric cloth," *Industrial and Engineering Chemistry Research*, vol. 44, no. 4, pp. 1027–1042, 2005.
- [8] D. Mohan, K. P. Singh, and V. K. Singh, "Trivalent chromium removal from wastewater using low cost activated carbon derived from agricultural waste material and activated carbon fabric cloth," *Journal of Hazardous Materials*, vol. 135, no. 1–3, pp. 280–295, 2006.
- [9] P. Miretzky and A. F. Cirelli, "Cr(VI) and Cr(III) removal from aqueous solution by raw and modified lignocellulosic materials: a review," *Journal of Hazardous Materials*, vol. 180, no. 1–3, pp. 1–19, 2010.
- [10] F. C. Richard and A. C. M. Bourg, "Aqueous geochemistry of chromium: a review," *Water Research*, vol. 25, no. 7, pp. 807–816, 1991.
- [11] J. Zhu, H. Gu, J. Guo et al., "Mesoporous magnetic carbon nanocomposite fabrics for highly efficient Cr(VI) removal," *Journal of Materials Chemistry A*, vol. 2, no. 7, pp. 2256–2265, 2014.
- [12] B. Qiu, C. Xu, D. Sun et al., "Polyaniline coating on carbon fiber fabrics for improved hexavalent chromium removal," *RSC Advances*, vol. 4, no. 56, pp. 29855–29865, 2014.
- [13] B. Qiu, C. Xu, D. Sun et al., "Polyaniline coated ethyl cellulose with improved hexavalent chromium removal," *ACS Sustainable Chemistry and Engineering*, vol. 2, no. 8, pp. 2070–2080, 2014.
- [14] T. Karthikeyan, S. Rajgopal, and L. R. Miranda, "Chromium(VI) adsorption from aqueous solution by *Hevea Brasilensis* sawdust activated carbon," *Journal of Hazardous Materials*, vol. 124, no. 1–3, pp. 192–199, 2005.
- [15] C. Xu, B. Qiu, H. Gu et al., "Synergistic interactions between activated carbon fabrics and toxic hexavalent chromium," *ECS Journal of Solid State Science and Technology*, vol. 3, no. 3, pp. M1–M9, 2014.
- [16] K. K. Krishnani and S. Ayyappan, "Heavy metals remediation of water using plants and lignocellulosic agrowastes," *Reviews of*

- Environmental Contamination and Toxicology*, vol. 188, pp. 59–84, 2006.
- [17] M. Aliabadi, I. Khazaei, H. Fakhraee, and M. T. H. Mousavian, "Hexavalent chromium removal from aqueous solutions by using low-cost biological wastes: equilibrium and kinetic studies," *International Journal of Environmental Science and Technology*, vol. 9, no. 2, pp. 319–326, 2012.
- [18] D. E. Kimbrough, Y. Cohen, A. M. Winer, L. Creelman, and C. Mabuni, "A critical assessment of chromium in the environment," *Critical Reviews in Environmental Science and Technology*, vol. 29, no. 1, pp. 1–46, 1999.
- [19] E. Salazar, M. I. Ortiz, A. M. Urtiaga, and J. A. Irabien, "Equilibrium and kinetics of chromium(VI) extraction with Aliquat 336," *Industrial and Engineering Chemistry Research*, vol. 31, no. 6, pp. 1516–1522, 1992.
- [20] K. A. Matis and P. Mavros, "Recovery of metals by ion flotation from dilute aqueous solutions," *Separation and Purification Method*, vol. 20, no. 1, pp. 1–48, 1991.
- [21] F. Akbal and S. Camci, "Copper, chromium and nickel removal from metal plating wastewater by electrocoagulation," *Desalination*, vol. 269, no. 1–3, pp. 214–222, 2011.
- [22] G. Tiravanti, D. Petruzzelli, and R. Passino, "Pretreatment of tannery wastewaters by an ion exchange process for Cr(III) removal and recovery," *Water Science and Technology*, vol. 36, no. 2–3, pp. 197–207, 1997.
- [23] S. Rengaraj, K.-H. Yeon, and S.-H. Moon, "Removal of chromium from water and wastewater by ion exchange resins," *Journal of Hazardous Materials*, vol. 87, no. 1–3, pp. 273–287, 2001.
- [24] S. Rengaraj, C. K. Joo, Y. Kim, and J. Yi, "Kinetics of removal of chromium from water and electronic process wastewater by ion exchange resins: 1200H, 1500H and IRN97H," *Journal of Hazardous Materials*, vol. 102, no. 2–3, pp. 257–275, 2003.
- [25] D. Petruzzelli, R. Passino, and G. Tiravanti, "Ion exchange process for chromium removal and recovery from tannery wastes," *Industrial and Engineering Chemistry Research*, vol. 34, no. 8, pp. 2612–2617, 1995.
- [26] C. A. Kozlowski and W. Walkowiak, "Removal of chromium(VI) from aqueous solutions by polymer inclusion membranes," *Water Research*, vol. 36, no. 19, pp. 4870–4876, 2002.
- [27] H. F. Shaalan, M. H. Sorour, and S. R. Tewfik, "Simulation and optimization of a membrane system for chromium recovery from tanning wastes," *Desalination*, vol. 141, no. 3, pp. 315–324, 2001.
- [28] Ihsanullah, A. Abbas, A. M. Al-Amer et al., "Heavy metal removal from aqueous solution by advanced carbon nanotubes: critical review of adsorption applications," *Separation and Purification Technology*, vol. 157, pp. 141–161, 2016.
- [29] L. Monser and N. Adhoum, "Modified activated carbon for the removal of copper, zinc, chromium and cyanide from wastewater," *Separation and Purification Technology*, vol. 26, no. 2–3, pp. 137–146, 2002.
- [30] D. Park, Y.-S. Yun, J. Y. Kim, and J. M. Park, "How to study Cr(VI) biosorption: use of fermentation waste for detoxifying Cr(VI) in aqueous solution," *Chemical Engineering Journal*, vol. 136, no. 2–3, pp. 173–179, 2008.
- [31] M. Ulmanu, E. Marañón, Y. Fernández, L. Castrillón, I. Anger, and D. Dumitriu, "Removal of copper and cadmium ions from diluted aqueous solutions by low cost and waste material adsorbents," *Water, Air, and Soil Pollution*, vol. 142, no. 1–4, pp. 357–373, 2003.
- [32] M. Aliabadi, K. Morshedzadeh, and H. Soheyli, "Removal of hexavalent chromium from aqueous solution by lignocellulosic solid wastes," *International Journal of Environmental Science and Technology*, vol. 3, no. 3, pp. 321–325, 2006.
- [33] V. K. Singh and P. N. Tiwari, "Removal and recovery of chromium (VI) from industrial waste water," *Journal of Chemical Technology and Biotechnology*, vol. 69, no. 3, pp. 376–382, 1997.
- [34] S. K. Srivastava, R. Tyagi, and N. Pant, "Adsorption of heavy metal ions on carbonaceous material developed from the waste slurry generated in local fertilizer plants," *Water Research*, vol. 23, no. 9, pp. 1161–1165, 1989.
- [35] E. Demirbas, M. Kobya, E. Senturk, and T. Ozkan, "Adsorption kinetics for the removal of chromium (VI) from aqueous solutions on the activated carbons prepared from agricultural wastes," *Water SA*, vol. 30, no. 4, pp. 533–539, 2004.
- [36] D. D. Das, R. Mahapatra, J. Pradhan, S. N. Das, and R. S. Thakur, "Removal of Cr(VI) from aqueous solution using activated cow dung carbon," *Journal of Colloid and Interface Science*, vol. 232, no. 2, pp. 235–240, 2000.
- [37] S. Bosinco, J. Roussy, E. P. Guibal, and P. L. Cloirec, "Interaction mechanisms between hexavalent chromium and corncob," *Environmental Technology*, vol. 17, no. 1, pp. 55–62, 1996.
- [38] P. Candela, J. M. M. Martinez, and R. T. Macia, "Chromium(VI) removal with activated carbons," *Water Research*, vol. 29, pp. 2174–2180, 1995.
- [39] A. M. El-Kamash, A. A. Zaki, and M. A. El Geleel, "Modeling batch kinetics and thermodynamics of zinc and cadmium ions removal from waste solutions using synthetic zeolite A," *Journal of Hazardous Materials*, vol. 127, no. 1–3, pp. 211–220, 2005.
- [40] G. Cimino, A. Passerini, and G. Toscano, "Removal of toxic cations and Cr(VI) from aqueous solution by hazelnut shell," *Water Research*, vol. 34, no. 11, pp. 2955–2962, 2000.
- [41] M. Kobya, "Adsorption, kinetic and equilibrium studies of Cr(VI) by hazelnut shell activated carbon," *Adsorption Science and Technology*, vol. 22, no. 1, pp. 51–64, 2004.
- [42] K. K. Singh, R. Rastogi, and S. H. Hasan, "Removal of cadmium from wastewater using agricultural waste 'rice polish'," *Journal of Hazardous Materials*, vol. 121, no. 1–3, pp. 51–58, 2005.
- [43] D. C. Sharma and C. F. Forster, "Removal of hexavalent chromium using sphagnum moss peat," *Water Research*, vol. 27, no. 7, pp. 1201–1208, 1993.
- [44] S. H. Lee, C. H. Jung, H. Chung, M. Y. Lee, and J.-W. Yang, "Removal of heavy metals from aqueous solution by apple residues," *Process Biochemistry*, vol. 33, no. 2, pp. 205–211, 1998.
- [45] C. K. Lee, K. S. Low, and K. L. Kek, "Removal of chromium from aqueous solution," *Bioresource Technology*, vol. 54, no. 2, pp. 183–189, 1995.
- [46] K. S. Low, C. K. Lee, and A. Y. Ng, "Column study on the sorption of Cr(VI) using quaternized rice hulls," *Bioresource Technology*, vol. 68, no. 2, pp. 205–208, 1999.
- [47] W. Jianlong, "Removal of Cr(VI) from aqueous solution by coal flyash adsorption I: characteristics of chromium adsorption on flyash," *Toxicological and Environmental Chemistry*, vol. 68, no. 1–2, pp. 53–62, 1999.
- [48] M. Dakiky, M. Khamis, A. Manassra, and M. Mer'eb, "Selective adsorption of chromium(VI) in industrial wastewater using low-cost abundantly available adsorbents," *Advances in Environmental Research*, vol. 6, no. 4, pp. 533–540, 2002.

- [49] N. K. Hamadi, X. D. Chen, M. M. Farid, and M. G. Q. Lu, "Adsorption kinetics for the removal of chromium(VI) from aqueous solution by adsorbents derived from used tyres and sawdust," *Chemical Engineering Journal*, vol. 84, no. 2, pp. 95–105, 2001.
- [50] K. Selvi, S. Pattabhi, and K. Kadirvelu, "Removal of Cr(VI) from aqueous solution by adsorption onto activated carbon," *Bioresource Technology*, vol. 80, no. 1, pp. 87–89, 2001.
- [51] S. S. Shukla, J. Y. Li, K. L. Dorris, and A. Shukla, "Removal of nickel from aqueous solutions by sawdust," *Journal of Hazardous Materials*, vol. 121, no. 1–3, pp. 243–246, 2005.
- [52] C. Selomulya, V. Meeyoo, and R. Amal, "Mechanisms of Cr(VI) removal from water by various types of activated carbons," *Journal of Chemical Technology and Biotechnology*, vol. 74, no. 2, pp. 111–122, 1999.
- [53] H. Farrah and W. F. Pickering, "The sorption of lead and cadmium species by clay minerals," *Australian Journal of Chemistry*, vol. 30, no. 7, pp. 1417–1422, 1977.
- [54] W. T. Tan, S. T. Ooi, and C. K. Lee, "Removal of chromium(VI) from solution by coconut husk and palm pressed fibres," *Environmental Technology*, vol. 14, no. 3, pp. 277–282, 1993.
- [55] K. Periasamy, K. Srinivasan, and P. R. Muruganan, "Studies on chromium(VI) removal by activated ground nut husk carbon," *Indian Journal of Environmental Health*, vol. 33, pp. 433–439, 1991.
- [56] M. S. Mansour, M. E. Ossman, and H. A. Farag, "Removal of Cd (II) ion from waste water by adsorption onto polyaniline coated on sawdust," *Desalination*, vol. 272, no. 1–3, pp. 301–305, 2011.
- [57] M. Ayoma, T. Sugiyama, S. Doi, N. S. Cho, and H. E. Kim, "Removal of Hexavalent chromium from dilute aqueous solution by coniferous leaves," *Holzforchung*, vol. 53, no. 4, pp. 365–368, 1999.
- [58] D. C. Sharma and C. F. Forster, "The treatment of chromium wastewaters using the sorptive potential of leaf mould," *Bioresource Technology*, vol. 49, no. 1, pp. 31–40, 1994.
- [59] L. Dupont and E. Guillon, "Removal of hexavalent chromium with a lignocellulosic substrate extracted from wheat bran," *Environmental Science and Technology*, vol. 37, no. 18, pp. 4235–4241, 2003.
- [60] Z. Reddad, C. Gerente, Y. Andres, and P. Le Cloirec, "Adsorption of several metal ions onto a low-cost biosorbent: kinetic and equilibrium studies," *Environmental Science and Technology*, vol. 36, no. 9, pp. 2067–2073, 2002.
- [61] A. C. A. Da Costa and F. P. De França, "Cadmium uptake by biosorbent seaweeds: adsorption isotherms and some process conditions," *Separation Science and Technology*, vol. 31, no. 17, pp. 2373–2393, 1996.
- [62] Y. Nakano, M. Tanaka, Y. Nakamura, and M. Konno, "Removal and recovery system of hexavalent chromium from waste water by tannin gel particles," *Journal of Chemical Engineering of Japan*, vol. 33, no. 5, pp. 747–752, 2000.
- [63] D. Kratochvil, P. Pimentel, and B. Volesky, "Removal of trivalent and hexavalent chromium by seaweed biosorbent," *Environmental Science and Technology*, vol. 32, no. 18, pp. 2693–2698, 1998.
- [64] M. E. A. Ali, "Synthesis and adsorption properties of chitosan-CDTA-GO nanocomposite for removal of hexavalent chromium from aqueous solutions," *Arabian Journal of Chemistry*, In press.
- [65] N. Calace, A. Di Muro, E. Nardi, B. M. Petronio, and M. Pietroletti, "Adsorption isotherms for describing heavy-metal retention in paper mill sludges," *Industrial and Engineering Chemistry Research*, vol. 41, no. 22, pp. 5491–5497, 2002.
- [66] C.-H. Weng, C. P. Huang, H. E. Allen, and P. F. Sanders, "Cr(VI) adsorption onto hydrous concrete particles from groundwater," *Journal of Environmental Engineering*, vol. 127, no. 12, pp. 1124–1131, 2001.
- [67] S. S. Ahluwalia and D. Goyal, "Removal of heavy metals by waste tea leaves from aqueous solution," *Engineering in Life Sciences*, vol. 5, no. 2, pp. 158–162, 2005.
- [68] V. Sarin and K. K. Pant, "Removal of chromium from industrial waste by using eucalyptus bark," *Bioresource Technology*, vol. 97, no. 1, pp. 15–20, 2006.
- [69] M. H. Dehghani, D. Sanaei, I. Ali, and A. Bhatnagar, "Removal of chromium(VI) from aqueous solution using treated waste newspaper as a low-cost adsorbent: kinetic modeling and isotherm studies," *Journal of Molecular Liquids*, vol. 215, pp. 671–679, 2016.
- [70] A. S. K. Kumar, S. S. Kakan, and N. Rajesh, "A novel amine impregnated graphene oxide adsorbent for the removal of hexavalent chromium," *Chemical Engineering Journal*, vol. 230, pp. 328–337, 2013.
- [71] Ihsanullah, F. A. Al-Khaldi, B. Abusharkh et al., "Adsorptive removal of cadmium(II) ions from liquid phase using acid modified carbon-based adsorbents," *Journal of Molecular Liquids*, vol. 204, pp. 255–263, 2015.
- [72] Ihsanullah, H. A. Asmaly, T. A. Saleh, T. Laoui, V. K. Gupta, and M. A. Atieh, "Enhanced adsorption of phenols from liquids by aluminum oxide/carbon nanotubes: comprehensive study from synthesis to surface properties," *Journal of Molecular Liquids*, vol. 206, pp. 176–182, 2015.
- [73] Ihsanullah, F. A. Al-Khaldi, B. Abu-Sharkh et al., "Effect of acid modification on adsorption of hexavalent chromium (Cr(VI)) from aqueous solution by activated carbon and carbon nanotubes," *Desalination and Water Treatment*, vol. 57, no. 16, pp. 7232–7244, 2016.
- [74] H. A. Asmaly, B. Abussaud, Ihsanullah, T. A. Saleh, V. K. Gupta, and M. A. Atieh, "Ferric oxide nanoparticles decorated carbon nanotubes and carbon nanofibers: from synthesis to enhanced removal of phenol," *Journal of Saudi Chemical Society*, vol. 19, no. 5, pp. 511–520, 2015.
- [75] H. A. Asmaly, B. Abussaud, Ihsanullah et al., "Evaluation of micro- and nano-carbon-based adsorbents for the removal of phenol from aqueous solutions," *Toxicological and Environmental Chemistry*, vol. 97, no. 9, pp. 1164–1179, 2015.
- [76] A. Abbas, B. A. Abussaud, Ihsanullah, N. A. H. Al-Baghli, M. Khraisheh, and M. A. Atieh, "Benzene removal by iron oxide nanoparticles decorated carbon nanotubes," *Journal of Nanomaterials*, vol. 2016, Article ID 5654129, 10 pages, 2016.
- [77] Ihsanullah, A. M. Al Amer, T. Laoui et al., "Fabrication and antifouling behaviour of a carbon nanotube membrane," *Materials and Design*, vol. 89, pp. 549–558, 2016.
- [78] J. Zhu, S. Wei, H. Gu et al., "One-pot synthesis of magnetic graphene nanocomposites decorated with core@double-shell nanoparticles for fast chromium removal," *Environmental Science and Technology*, vol. 46, no. 2, pp. 977–985, 2012.
- [79] C. J. Lin, S. L. Wang, P. M. Huang et al., "Chromate reduction by zero-valent Al metal as catalyzed by polyoxometalate," *Water Research*, vol. 43, no. 20, pp. 5015–5022, 2009.

- [80] J. Hu, C. Chen, X. Zhu, and X. Wang, "Removal of chromium from aqueous solution by using oxidized multiwalled carbon nanotubes," *Journal of Hazardous Materials*, vol. 162, no. 2-3, pp. 1542–1550, 2009.
- [81] H. Ding, X. Li, J. Wang, X. Zhang, and C. Chen, "Adsorption of chlorophenols from aqueous solutions by pristine and surface functionalized single-walled carbon nanotubes," *Journal of Environmental Sciences*, vol. 43, pp. 187–198, 2016.

Research Article

Removal of Zinc from Aqueous Solution by Optimized Oil Palm Empty Fruit Bunches Biochar as Low Cost Adsorbent

Seyed Ali Zamani,¹ Robiah Yunus,² A. W. Samsuri,³
M. A. Mohd Salleh,⁴ and Bahareh Asady²

¹Department of Civil Engineering, Faculty of Engineering, Universiti Putra Malaysia, 43300 UPM Serdang, Selangor, Malaysia

²Department of Chemical and Environmental Engineering, Faculty of Engineering, Universiti Putra Malaysia, 43300 UPM Serdang, Selangor, Malaysia

³Department of Land Management, Faculty of Agriculture, Universiti Putra Malaysia, 43400 UPM Serdang, Selangor, Malaysia

⁴Institute of Advanced Technology, Faculty of Engineering, Universiti Putra Malaysia, 43400 UPM Serdang, Selangor, Malaysia

Correspondence should be addressed to Robiah Yunus; robiah@upm.edu.my

Received 5 January 2017; Accepted 19 February 2017; Published 21 March 2017

Academic Editor: Muataz A. Atieh

Copyright © 2017 Seyed Ali Zamani et al. This is an open access article distributed under the Creative Commons Attribution License, which permits unrestricted use, distribution, and reproduction in any medium, provided the original work is properly cited.

This study aims to produce optimized biochar from oil palm empty fruit bunches (OPEFB), as a green, low cost adsorbent for uptake of zinc from aqueous solution. The impact of pyrolysis conditions, namely, highest treatment temperature (HTT), heating rate (HR), and residence time (RT) on biochar yield and adsorption capacity towards zinc, was investigated. Mathematical modeling and optimization of independent variables were performed employing response surface methodology (RSM). HTT was found to be the most influential variable, followed by residence time and heating rate. Based on the central composite design (CCD), two quadratic models were developed to correlate three independent variables to responses. The optimum production condition for OPEFB biochar was found as follows: HTT of 615°C, HR of 8°C/min, and RT of 128 minutes. The optimum biochar showed 15.18 mg/g adsorption capacity for zinc and 25.49% of yield which was in agreement with the predicted values, satisfactory. Results of the characterization of optimum product illustrated well-developed BET surface area and porous structure in optimum product which favored its sorptive ability.

1. Introduction

Heavy metal pollution is one of the most serious environmental issues, faced worldwide today [1–3]. Intense industrial activities result in releasing of significant amount of heavy metals including zinc into aqua environment [4]. Mining, metal coating, galvanizing steel and iron, and production of batteries, as well as production of deodorants, paints, ceramic, wood, drug, and fabrics, are major industries, responsible for releasing of zinc into environment [4]. Human exposure to intense amount of zinc leads to metal-fume fever, vomiting, stomach cramp, nausea, loss of appetite, and neurological signs such as ataxia [5]. Health risks of zinc contaminated water for both human and other living organisms is a great concern because of its non biodegradability and mobility. According to World Health Organization guidelines for

quality of drinking water and to protect the environment, maximum acceptable zinc level in drinking water is recommended as 5.00 mg/l [6]. Due to global shortage of water resources, health risks, and environmental problems associated with heavy metal pollution such as zinc, treatment of wastewater by effective methods is critical.

Different methods and techniques have been introduced for controlling water and wastewater pollution by heavy metals such as ion exchange, adsorption, precipitation, coagulation, membrane technologies, and reverse osmosis. Among these methodologies, adsorption has been demonstrated to be an economically practicable alternative method for uptake of metals from water system [7, 8]. The simplicity of operation and design in this method as well as its effectiveness in minimizing various types of pollutants leads to its widespread applicability in controlling water pollution [9]. High cost

of adsorption by commercially produced activated carbon leads to extensive researches on possibility of using waste biomaterials, as low cost sorbents, for treatment of water and wastewater from heavy metal contaminants [10].

In recent years, biochar from different agrobased and municipal waste materials has been shown to be a potential low cost alternative for separation of heavy metal from water system [11, 12]. Different agrobased and municipal wastes derived biochars have been evaluated for removal of toxic metals in numerous studies. The results of these studies highlighted the capability of biochars as great potential low cost sorbents and indicated the important role of biochar's physicochemical characteristics in its uptake ability [2, 7, 13–16].

Annually, enormous amounts of biowastes from oil palm mills are produced around the world which contribute to great environmental concern, and many researchers have been focused on conversion of these wastes into value-added products. Oil palm empty fruit bunches account for 23% per ton of fresh fruit bunch which should be handled properly [17]. Currently, the majority of empty fruit bunches are combusted in the incinerators for the purpose of fertilizer production which produces "white smoke" and considered an environmental concern by the Department of Environment [18]. The great amount of generated empty fruit bunches from oil palm mills could be a potential feedstock substrate for biochar production by an environmentally friendly method. Production of biochar from oil palm empty fruit bunches, an abundant waste of oil palm mill, has twofold advantage: firstly, production of low cost and ecofriendly adsorbent for removal of heavy metals and, secondly, solving part of waste disposal problem by conversion of unwanted wastes into value-added products.

Production of efficient sorbent for this purpose has been always a concern. Among the sorbent characteristics, surface area, surface functionalities, and acceptable level of yield are important in adsorption process design [19]. These characteristics of biochar are controlled by its production conditions and primary feedstock properties [19]. In assessing the effect of production conditions, employing an adequate experimental design is key point.

Design of experiment (DOE) enables engineering researchers to alleviate the costs by rationalizing the experiments and improving productivity and product quality. Response surface methodology, one of the DOE techniques, is applied for experimental design, statistical modeling, and optimization of a process. It is a helpful tool in studying the effect of factors and their interactions on specific response to optimize the response of interest [20].

RSM has been widely used in optimization of experimental conditions of various processes; however, its application in production of biochar is very rare in literature. Some previous studies focused on applying RSM in determining the effect of different parameters during production of adsorbent and batch adsorption experiments, on removal of hazardous contaminants such as chromium [21, 22], copper [23], nickel [24], reactive blue dye [25], lead and zinc [26], and cationic and anionic dye [27].

To our knowledge, no study has been performed on optimized production of biochar from oil palm empty fruit

bunches, applying RSM. Therefore, the focus of the present study is to produce biochar from oil palm empty fruit bunches and to optimize the preparation conditions using central composite design for yield and its adsorption capacity towards zinc. The influence of three numerical variables, namely, highest treatment temperature, heating rate, and residence time, on the responses was considered, simultaneously.

2. Materials and Methods

2.1. Preparation of Biochar. Oil palm empty fruit bunches were collected from Ulu Langat Palm Oil Mill, a local oil palm mill in Malaysia; Seri Sdn Bhd (Lot 3115, Batu 34, Jalan Banting, Dengkil, 43800, Selangor, Malaysia). The biomass samples were dried in oven at 105°C for 24 h to get constant weight. Afterward, the samples were cut into smaller parts (2 nm) to ease the pyrolysis process. The pyrolysis process was performed by placing samples in vertical stainless steel reactor and heating from room temperature to predetermined temperature with specific heating rate and they were kept at highest temperature for specific duration. Purified nitrogen (99.995%) with flow rate of 150 cm³/min was used during pyrolysis process to wash tarry vapors away from the surface of biochar.

2.2. Design of Experiment. Response surface methodology (RSM) is a statistical technique which utilizes the quantitative data of the experiments for purpose of determining the regression model and optimum operation conditions [28]. It applies mathematical and statistical methods for analyzing and simulating of a process with the objective of optimizing a response which is affected by several independent variables [29]. Central composite design (CCD) is the most common method for fitting quadratic surfaces and optimization with minimum number of experiments [30]. In general, CCD consists of 2ⁿ factorial runs, 2n axial runs, and n_c center points in which n is the number factors.

Three numerical factors have been considered for this purpose, namely, x₁ as highest treatment temperature (HTT), x₂ as heating rate (HR), and x₃ as residence time (RT). Two responses in this work were yield (Y₁) and adsorption capacity of OPEFB biochar (Y₂). Number of runs based on CCD method for three independent variables is equal to 20 experiments, including 8 factorial points, 6 axial points, and 6 center points based on the following equation [31]:

$$N = 2^n + 2n + n_c = 2^3 + 2 \times 3 + 6 = 20, \quad (1)$$

where N is the total number of experiments and n is the number of factors. The center points are useful in considering the errors of experiments and reproducibility of the model. For all three factors the ranges have been entered based on "−alpha" and "+alpha" level where alpha is the distance of axial points from center points, intending not to have any unreachable level for the factors. These variables and their respective ranges were selected based on screening tests in preliminary studies. Levels of independent variables are given in Table 1. The experiments were conducted as randomized in order to minimize the influence of uncontrolled factors.

TABLE 1: Level of different factors.

Variables	Units	(-1) level	(+1) level	-alpha	+alpha
(A) HTT	(°C)	460.8095	639.1905	400	700
(B) HR	(°C/min)	7.026982	12.97302	5	15
(C) RT	(min)	60.40473	149.5953	30	180

An empirical model was developed to correlate the three independent variables and each response based on second-order polynomial equation as follows:

$$Y = b_0 + \sum_{i=1}^n b_i x_i + \left(\sum_{i=1}^n b_{ii} x_i \right)^2 + \sum_{i=1}^{n-1} \sum_{j=i+1}^n b_{ij} x_i x_j \quad (2)$$

In which, b_0 is the constant, b_i is the linear coefficient and b_{ii} is the quadratic coefficient, and x_i and x_j are the coded values of pyrolysis conditions.

2.3. Model Fitting and Statistical Analysis. The analysis of experimental data was performed using Design Expert version 7 (STAT-EASE Inc., Minneapolis, USA) for regression analysis to fit the empirical models and statistical significance evaluation of the models.

2.4. Adsorption Experiments. Zinc stock solution was prepared by dissolving appropriate amount of $ZnCl_2$ (Anhydrous, Sigma Aldrich) in Millipore water with purity of 99.99% to concentration of 2000 ppm. The batch adsorption experiments were conducted in 20 sets of 250 ml Erlenmeyer flasks. In a typical experiment, 0.4 g of biochar was added to 50 ml of heavy metal solution with concentration of 200 ppm and the pH of solution was set at 6. Subsequently the mixture was agitated for 24 hours for equilibration and then filtered employing Whatman filter paper. The equilibrium time was selected based on preliminary studies as the time when the zinc concentration remained constant. The resultant solution was analyzed for concentration of zinc utilizing A Analyst 400 PerkinElmer atomic absorption spectrometer device. The adsorption capacity of biochars was calculated by the following equation:

$$Q = \frac{(C_i - C_e) v}{m} \quad (3)$$

In the previous equation, C_i and C_e are the initial and equilibrium concentration of zinc (mg/l), respectively. Q (mg/g) is the adsorption capacity of biochar, m is the dry mass of biochar (g), and v is for volume of solution (l).

2.5. Yield of Biochar. The yield of biochar was calculated according to the following equation:

$$\text{Yield} = \frac{\text{weight of biochar (g)}}{\text{weight of dry biomass (g)}} * 100. \quad (4)$$

2.6. Characterization of Optimum Biochar. The surface structure of biochar was analyzed by means of scanning electron microscopy utilizing Zeiss scanning electron microscope

(Carl Zeiss Germany). N_2 adsorption at 77 K was performed for surface area and pore volume estimation of biochar, using Sorptomatic 1990 system (Thermo Finnigan). Surface functional groups of biochars were determined with aid of Fourier Transform Infrared spectroscopy, using Nicolet Nexus 6700 FTIR spectrometer. The KBr pellet was prepared by mixing well grinded biochar samples with KBr powder at ratio of 1:100 approximately.

3. Results and Discussion

3.1. Development of Regression Model Equation. The complete design matrix of experiments with the obtained results for both responses is presented in Table 2. A polynomial regression equation was developed based on CCD to analyze the variables, their interactions, and identifying the significant factors. Runs 1, 4, 12, 15, 16, and 19 are center points and used to determine the error of experiments. Biochar yield was found to be in the range of 23.2% and 33.73% while the adsorption capacity for zinc obtained ranged between 7.59 mg/g and 14.74 mg/g.

Based on the sequential model sums of squares, the fitted model was chosen as the highest order polynomial model in which the additional terms were significant and model was not aliased. For both responses, the quadratic model was selected as suggested by the software. The final empirical equations for yield (Y_1) and zinc adsorption capacity of biochar (Y_2) in terms of coded variables are presented in (1) and (2), respectively.

$$Y_2 = 25.91 - 2.39x_1 - 1.23x_2 - 0.61x_3 + 0.40x_1x_2 + 0.23x_1x_3 - 0.22x_2x_3 + 1.15x_1^2 + 0.24x_2^2 - 0.051x_3^2, \quad (5)$$

$$Y_2 = 14.01 + 1.56x_1 - 0.66x_2 + 0.90x_3 + 0.11x_1x_2 + 0.28x_1x_3 + 0.035x_2x_3 - 1.12x_1^2 - 0.56x_2^2 - 1.07x_3^2. \quad (6)$$

Positive sign in front of the terms represents the synergistic influence while negative sign represents antagonistic influence. Values of coefficient determination, R squared, adjusted R squared, standard deviation (SD), and coefficient of variation (CV) were used to evaluate the quality of developed model. R^2 values for (5) and (6) were 0.9766 and 0.9794, implying that models were able to explain 97.66% and 97.94% of total variance in biochar yield and biochar adsorption capacity for zinc, respectively. The closer R^2 is to unity, the better the model fits experimental data. Both R^2 values are considered relatively high and suggesting satisfactory agreement between model and experimental data. The adjusted R squared with values of 0.9556 and 0.9609 for (5) and (6), respectively, indicates good sample size and ability of model. Coefficient of variation (CV) is a measure of the model reproducibility and considered as the ratio of standard deviation to mean value of observed response. The model is regarded as reproducible if the value of CV for the model

TABLE 2: Design matrix with results.

Run	Point type	(A) HTT (°C)	(B) HR (°C/min)	(C) RT (min)	Yield (%)	Q (mg/g)
1	Center	550.00	10.00	105.00	26.14	13.72
2	Axial	550.00	15.00	105.00	25.2	11.43
3	Fact	460.81	7.03	60.40	32.08	10.28
4	Center	550.00	10.00	105.00	25.97	13.91
5	Axial	550.00	10.00	180.00	24.93	12.11
6	Axial	550.00	10.00	30.00	26.67	9.47
7	Axial	700.00	10.00	105.00	24.67	13.67
8	Fact	639.19	7.03	149.60	26.01	14.74
9	Axial	400.00	10.00	105.00	33.73	7.59
10	Fact	460.81	12.97	149.60	26.45	9.89
11	Axial	550.00	5.00	105.00	28.06	13.01
12	Center	550.00	10.00	105.00	26.25	14.22
13	Fact	460.81	12.97	60.40	28.54	8.35
14	Fact	460.81	7.03	149.60	30.52	11.53
15	Center	550.00	10.00	105.00	25.88	14.13
16	Center	550.00	10.00	105.00	25.9	13.81
17	Fact	639.19	7.03	60.40	26.29	12.22
18	Fact	639.19	12.97	149.60	23.2	13.37
19	Center	550.00	10.00	105.00	25.3	14.36
20	Fact	639.19	12.97	60.40	24.71	10.86

TABLE 3: Analysis of variance (ANOVA) for response surface quadratic model for yield.

Source of data	Sum of squares	Degree of freedom (DF)	Mean square	F-value	p value Prob > F	Comment
Model	125.62	9	13.96	46.44	<0.0001	Significant
x_1	77.90	1	77.90	259.18	<0.0001	
x_2	20.69	1	20.69	68.84	<0.0001	
x_3	5.13	1	5.13	17.05	0.0020	
x_1x_2	1.30	1	1.30	4.31	0.0646	
x_1x_3	0.43	1	0.43	1.44	0.2580	
x_2x_3	0.39	1	0.39	1.29	0.2828	
x_1^2	19.09	1	19.09	63.50	<0.0001	
x_2^2	0.85	1	0.85	2.81	0.1244	
x_3^2	0.038	1	0.038	0.13	0.7302	
Residual	3.01	10	0.30			
Lack of fit	2.46	5	0.49	4.51	0.0618	Not significant
Pure error	0.55	5	0.11			

is less than 10% [26, 32]. Coefficients of variation (CV) for both studied responses were less than 10% and were equal to 2.04% and 3.47% for Y_1 and Y_2 , respectively. The standard deviation values for the models were 0.55 and 0.42 which reflect the accuracy of the model. The adequacy of the model was further checked by analysis of variance (ANOVA). The ANOVA for quadratic model for yield of biochar is given in Table 3. From ANOVA for yield of biochar, the F -value was 46.44 and p value was less than 0.0001, reflecting that model was significant. Regarding the model terms, p value less than 0.05 implies that model term was significant. According to Table 3 for yield of biochar, x_1 , x_2 , x_3 , and x_1^2 were significant

model terms, whereas x_1x_2 , x_2x_3 , x_1x_3 , x_2^2 , and x_3^2 were insignificant terms to the model.

The result of ANOVA for quadratic model for adsorption capacity of biochar is presented in Table 4. The F -value of 52.95 with p value less than 0.0001 indicates the significance of the model. Table 4 illustrates that x_1 , x_2 , x_3 , x_1^2 , x_2^2 , and x_3^2 are significant model terms. On the other hand, the interactions of factors x_1x_2 , x_1x_3 , and x_2x_3 were insignificant terms to the response.

The predicted versus experimental values for yield and adsorption capacity of OPEFB biochar are illustrated in Figures 1 and 2, respectively. As it can be observed, the

TABLE 4: Analysis of variance (ANOVA) for response surface quadratic model for adsorption capacity of OPEFB biochar.

Source of data	Sum of squares	Degree of freedom (DF)	Mean square	F-value	p value Prob > F	Comment
Model	84.47	9	9.39	52.95	<0.0001	Significant
x_1	33.42	1	33.42	188.57	<0.0001	
x_2	5.87	1	5.87	33.14	0.0002	
x_3	11.01	1	11.01	62.09	<0.0001	
x_1x_2	0.09	1	0.09	0.5	0.4967	
x_1x_3	0.63	1	0.63	3.54	0.0894	
x_2x_3	0.01	1	0.01	0.06	0.8189	
x_1^2	18.2	1	18.2	102.69	<0.0001	
x_2^2	4.55	1	4.55	25.65	0.0005	
x_3^2	16.42	1	16.42	92.62	<0.0001	
Residual	1.77	10	0.18			
Lack of fit	1.46	5	0.29	4.65	0.0585	Not significant
Pure error	0.31	5	0.06			

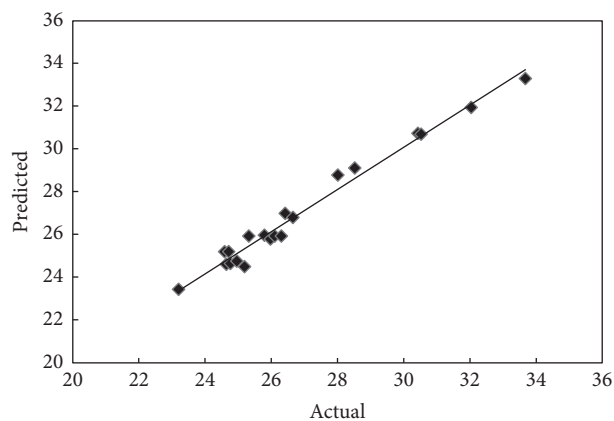


FIGURE 1: Predicted versus actual values for yield of OPEFB biochar.

predicted values are close to the experimental values which indicate that the developed model successfully fitted the correlation between variables and responses.

3.2. Yield of Oil Palm Empty Fruit Bunches Biochar (OPEFBB).

Referring to the yield of biochar, HTT had the greatest influence on the response followed by the HR and RT. Figures 3(a) and 3(b) represent the three-dimensional response surfaces to demonstrate the influence of biochar preparation conditions on yield. Figure 3(a) illustrates the surface plot of percentage of yield under the impact of highest treatment temperature (HTT) and heating rate (HR) where residence time (RT) was fixed at zero level (105 minutes). On the other hand, Figure 3(b) illustrates the effect of highest treatment temperature and residence time on yield (heating rate was fixed at zero level). As demonstrated in Figures 3(a) and 3(b), the biochar yield decreased with increasing in HTT, HT, and RT.

Similar trend was also reported in other works, studying the influence of production parameters on char yield.

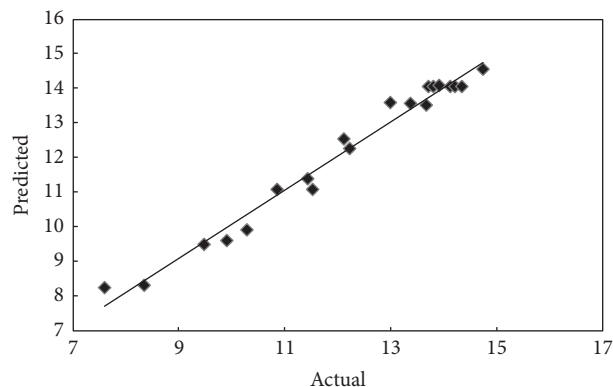


FIGURE 2: Predicted versus actual values for adsorption capacity of OPEFB biochar.

Al-Wabel et al. reported reduction in yield of *Conocarpus* wastes biochar by increasing the highest treatment temperature, specifically when the temperature increased more than 200°C. This may be due to the destruction of cellulose and hemicellulose and combustion of organic matters [33]. Angin found that the yield of safflower seed cake-based biochar was reduced by rising pyrolysis temperature and heating rate. The effect of heating rate on the yield was also reported to be more significant at lower pyrolysis temperatures [34]. McBeath et al. examined the effect of pyrolysis conditions on yield and characteristics of biochar from eighteen different feedstocks and concluded that increasing pyrolysis temperature resulted in lower yield of char [35]. This is due to the evaporation of volatile matters and higher heat and mass transfer rate and destructive reactions. In another study by Hmid et al. both pyrolysis temperature and heating rate were reported as influential factors on the yield of biochars derived from olive solid residues considerably [36]. Ronsse et al. studied the influence of pyrolysis peak temperature and residence time on the yield of biochars from various feedstocks. It was

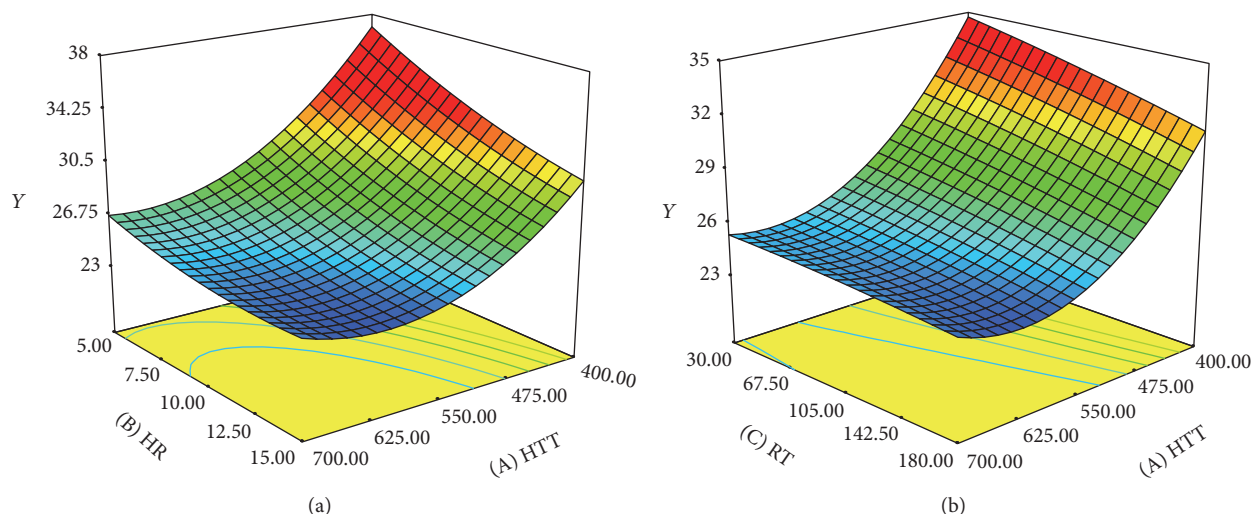


FIGURE 3: (a) Surface plot of percentage of yield (Y) as a function of highest treatment temperature (HTT) and heating rate (HR) at fixed residence time of 105 minutes. (b) Surface plot of percentage of yield (Y) as a function of highest treatment temperature (HTT) and residence time (RT) at fixed heating rate of 10°C per minute.

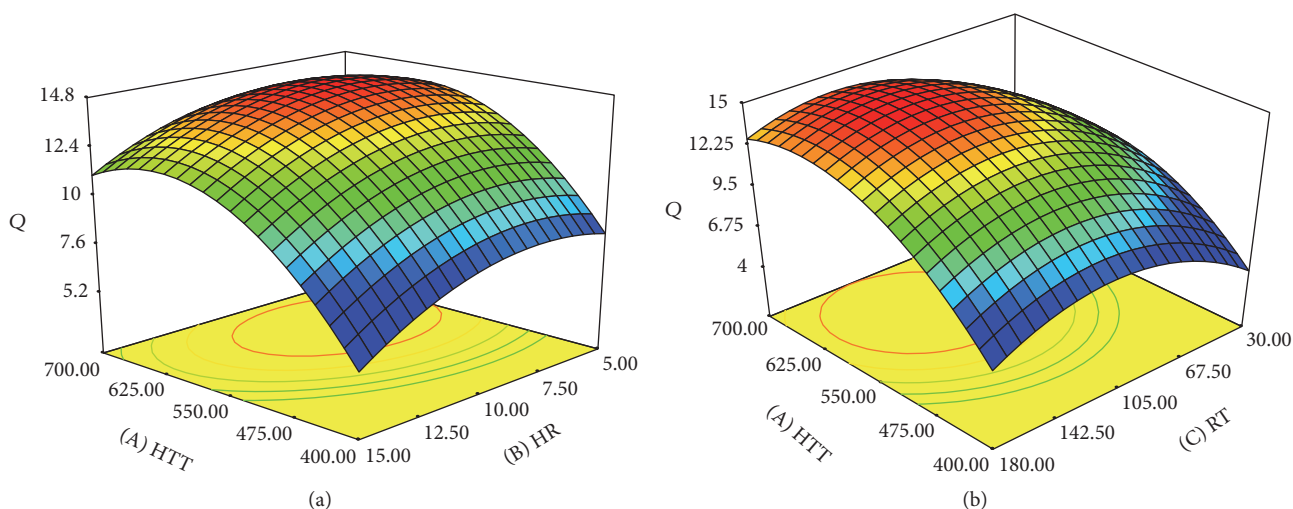


FIGURE 4: (a) Surface plot of adsorption capacity of biochar (Q) as a function of highest treatment temperature (HTT) and heating rate (HR) at fixed residence time of 105 minutes. (b) Surface plot of adsorption capacity of biochar (Q) as a function of highest treatment temperature (HTT) and residence time (RT) at fixed heating rate of 10°C per minute.

observed that biochar yield tends to decrease by increasing residence time and peak temperature [37].

In this work, all three production variables correlated negatively with biochar yield. The interaction effect of production parameters on biochar yield was not significant. The increase in pyrolysis temperature resulted in releasing of more volatile compound, primary decomposition of parent material, and possible secondary decomposition of produced biochar. Increasing in heating rate may cause severe heat and mass transfer rate which led to lower biochar yield. The influence of residence time on biochar yield was not also significant.

3.3. Adsorption Capacity of Oil Palm Empty Fruit Bunches Biochar (OPEFBB).

Based on the ANOVA, all three variables

and their quadratic effect were found to be significant on the adsorption capacity of OPEFBB biochar; however, HTT with F -value of 33.4246 was the most influential factor. Figures 4(a) and 4(b) demonstrate the three-dimensional response surfaces to show the influence of operating variables on adsorption capacity. The effect of the highest treatment temperature and heating rate on adsorption capacity where residence time was maintained at zero level is depicted in Figure 4(a), whereas the effect of highest treatment temperature and residence time on adsorption capacity of OPEFBB biochar when heating rate was fixed at zero level is presented in Figure 4(b). As it can be seen from Figure 4(a), the adsorption capacity of biochar increases with increasing temperature and heating rate up to specific point and, afterward, it decreases possibly because of blockage of some pores

TABLE 5: Model validation.

Model desirability	HTT (x_1)	HR (x_2)	RT (x_3)	Biochar yield (%)		Adsorption capacity (mg/g)	
				Predicted	Experimental	Predicted	Experimental
0.934	615	8	128	25.28	25.49	14.98	15.18

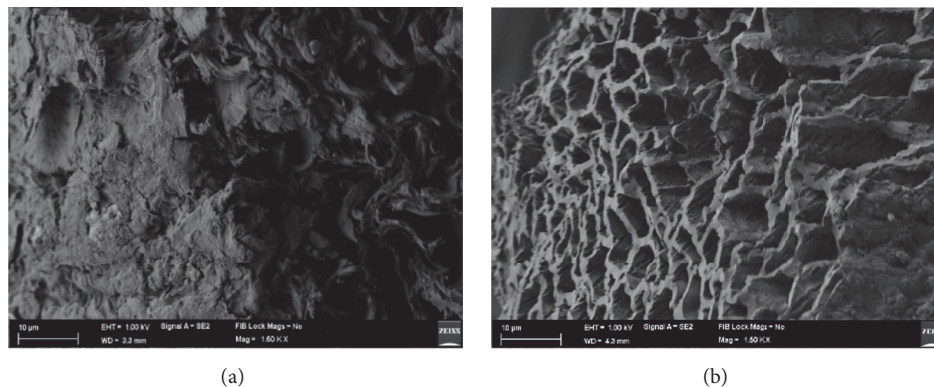


FIGURE 5: (a) SEM image of oil palm empty fruit bunches. (b) SEM image of OPEFB biochar produced under optimum conditions.

due to melting and releasing of tars. The highest treatment temperature had a positive linear effect on adsorption capacity, whereas heating rate has a negative effect. In addition, both factors have a negative quadratic effect on adsorption capacity of OPEFB biochar. Raising heating rate increases the adsorption capacity up to a certain point after which it reduces. This is due to the fact that the time for releasing volatiles becomes shortened at high heating rate which results in agglomeration of volatiles between and inside the pores and, therefore, the chance of blocking the pores entrance increases. Similar results have been reported in other studies [34, 38, 39].

Surface plot of the effect of highest treatment temperature and residence time on adsorption capacity of OPEFB biochar when heating rate was fixed at zero level is presented in Figure 4(b). Residence time increase favors the adsorption capacity up to a certain point of time, after which further increase causes the adsorption capacity to decrease due to the failure of pore walls' strength and their destruction.

3.4. Process Optimization. Getting high yield is an important factor in producing biosorbents, but adsorption capacity determines the quality of product. Therefore, both high yield and high adsorption capacity is desirable for economics feasibility of the product. However, optimizing both of these responses is very difficult as their affecting factors are opposite, which means adsorption capacity of OPEFB biochar increases while the yield decreases and vice versa. Consequently, in order to compromise between the two responses, the function of desirability has been employed using Expert-Design software version 7 (STAT-EASE Inc., Minneapolis, USA). The experimental conditions which showed the highest desirability were chosen for verification. The yield and adsorption capacity of the biochar prepared under optimum conditions compared to the predicted values are presented in Table 5. The optimum biochar from oil palm empty fruit

bunches was obtained using highest temperature of 615°C, heating rate of 8°C/min, and residence time of 128 min. The optimum biochar showed the adsorption capacity of 15.03 mg/g towards zinc and the biochar yield of 25.27%.

As it can be observed from Table 5, the obtained experimental results are in good agreement with model prediction points with relatively small deviation, indicating the accuracy of the model. Overall, OPEFB proved to be a potential promising substrate for production of biochar, a green low cost sorbent, with high performance for removal of heavy metals (zinc) from the aqueous solution.

3.5. Characterization. Figures 5(a) and 5(b) illustrate the scanning electron microscope images of the precursor (OPEFB) and the biochar obtained under optimum conditions. As it is clear in the micrograph, the external surfaces of the biochar obtained under optimized conditions consist of cracks, crevices, and significant amount of honey comb like pores with various sizes. Comparison of this micrograph with SEM micrograph of OPEFB revealed that during pyrolysis the cracks and pores of biochar become cleaner due to increase in devolatilization and, therefore, more ordered structural arrangement can be detected in optimum product.

Figure 6 displays the adsorption-desorption isotherm of OPEFB biochar synthesized under RSM optimum conditions. This adsorption isotherm can be classified as type I with a type H4 hysteresis loop at relative pressure 0.9, resembling microporous structured materials with some degree of mesoporosity. The surface physical parameters determined from N₂ adsorption isotherm for optimum product and OPEFB biochar synthesized at 300°C from the preliminary studies are summarized in Table 6. By comparison of the results of textural properties of optimum OPEFB biochar with unoptimized one, it is evident that RSM optimum product displays higher BET surface area, micropore surface area, micropore volume, and mesopore volume indicating pore

TABLE 6: Results of surface area and pore characterization of optimized RSM OPEFB biochar.

Material	BET surface area (m ² /g)	Micropore surface area (m ² /g)	Micropore volume (cm ³ /g)	Mesopores volume (cm ³ /g)	Total pore volume (cm ³ /g)	Average pore diameter (Å)	Reference
RSM optimized OPEFB biochar	421.26	347.09	0.13	0.018	0.15	14.41	Present study
OPEFB biochar (300°)	44.38	7.80	0.003	0.317	0.32	28.84	Preliminary study

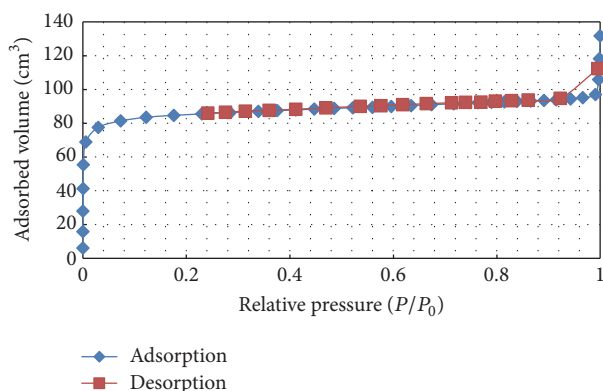


FIGURE 6: Adsorption-desorption isotherm graph of OPEFB biochar produced at RSM optimum conditions.

development at optimum pyrolysis conditions. This is most likely due to the progressive decomposition of volatile matter and better carbonization that leads to enhanced porosity.

4. Conclusion

In this study, novel, low cost adsorbent from empty fruit bunches were synthesized by pyrolysis. The influence of pyrolysis conditions on the yield and adsorption capacity of oil palm empty fruit bunches biochar for zinc was studied employing RSM. Through analysis of developed response surfaces, HTT was found to have the most significant influence on both responses. The optimum biochar was obtained at highest treatment temperature of 615°C, heating rate of 8°C/min, and residence time of 128 min which demonstrated 15.18 mg/g zinc adsorption capacity and 25.49% yield. The resultant biochar produced under optimum conditions demonstrates 421.26 m²/g surface area and 0.15 cm³/g total pore volume.

Conflicts of Interest

Authors declare no conflicts of interest.

References

- [1] S.-J. Lee, J. H. Park, Y.-T. Ahn, and J. W. Chung, "Comparison of heavy metal adsorption by peat moss and peat moss-derived biochar produced under different carbonization conditions," *Water, Air, and Soil Pollution*, vol. 226, no. 2, article 2275, 2015.
- [2] D. Kołodyńska, J. Krukowska, and P. Thomas, "Comparison of sorption and desorption studies of heavy metal ions from biochar and commercial active carbon," *Chemical Engineering Journal*, vol. 307, pp. 353–363, 2017.
- [3] V. M. Martínez-Juárez, J. F. Cárdenas-González, M. E. Torre-Bouscoulet, and I. Acosta-Rodríguez, "Biosorption of mercury (II) from aqueous solutions onto fungal biomass," *Bioinorganic Chemistry and Applications*, vol. 2012, Article ID 156190, 5 pages, 2012.
- [4] S. Malamis and E. Katsou, "A review on zinc and nickel adsorption on natural and modified zeolite, bentonite and vermiculite: examination of process parameters, kinetics and isotherms," *Journal of Hazardous Materials*, vol. 252–253, pp. 428–461, 2013.
- [5] F. Fu and Q. Wang, "Removal of heavy metal ions from wastewaters: a review," *Journal of Environmental Management*, vol. 92, no. 3, pp. 407–418, 2011.
- [6] N. K. Srivastava and C. B. Majumder, "Novel biofiltration methods for the treatment of heavy metals from industrial wastewater," *Journal of Hazardous Materials*, vol. 151, no. 1, pp. 1–8, 2008.
- [7] D. Mohan, A. Sarswat, Y. S. Ok, and C. U. Pittman, "Organic and inorganic contaminants removal from water with biochar, a renewable, low cost and sustainable adsorbent—a critical review," *Bioresour. Technology*, vol. 160, pp. 191–202, 2014.
- [8] F. Mutongo, O. Kuipa, and P. K. Kuipa, "Removal of Cr(VI) from aqueous solutions using powder of potato peelings as a low cost sorbent," *Bioinorganic Chemistry and Applications*, vol. 2014, Article ID 973153, 2014.
- [9] A. Bhatnagar and M. Sillanpää, "Utilization of agro-industrial and municipal waste materials as potential adsorbents for water treatment—a review," *Chemical Engineering Journal*, vol. 157, no. 2–3, pp. 277–296, 2010.
- [10] A. S. Singha and A. Guleria, "Use of low cost cellulosic biopolymer based adsorbent for the removal of toxic metal ions from the aqueous solution," *Separation Science and Technology*, vol. 49, no. 16, pp. 2557–2567, 2014.
- [11] X. Tan, Y. Liu, G. Zeng et al., "Application of biochar for the removal of pollutants from aqueous solutions," *Chemosphere*, vol. 125, pp. 70–85, 2015.
- [12] M. I. Inyang, B. Gao, Y. Yao et al., "A review of biochar as a low-cost adsorbent for aqueous heavy metal removal," *Critical Reviews in Environmental Science and Technology*, vol. 46, no. 4, pp. 406–433, 2016.
- [13] Y. Han, A. A. Boateng, P. X. Qi, I. M. Lima, and J. Chang, "Heavy metal and phenol adsorptive properties of biochars from pyrolyzed switchgrass and woody biomass in correlation with

- surface properties,” *Journal of Environmental Management*, vol. 118, pp. 196–204, 2013.
- [14] J.-H. Park, Y. S. Ok, S.-H. Kim et al., “Competitive adsorption of heavy metals onto sesame straw biochar in aqueous solutions,” *Chemosphere*, vol. 142, pp. 77–83, 2016.
- [15] X. Cui, S. Fang, Y. Yao et al., “Potential mechanisms of cadmium removal from aqueous solution by *Canna indica* derived biochar,” *Science of the Total Environment*, vol. 562, pp. 517–525, 2016.
- [16] G. N. Paranavithana, K. Kawamoto, Y. Inoue et al., “Adsorption of Cd^{2+} and Pb^{2+} onto coconut shell biochar and biochar-mixed soil,” *Environmental Earth Sciences*, vol. 75, no. 6, article 484, 2016.
- [17] R. Omar, A. Idris, R. Yunus, K. Khalid, and M. I. Aida Isma, “Characterization of empty fruit bunch for microwave-assisted pyrolysis,” *Fuel*, vol. 90, no. 4, pp. 1536–1544, 2011.
- [18] S. H. Chang, “An overview of empty fruit bunch from oil palm as feedstock for bio-oil production,” *Biomass and Bioenergy*, vol. 62, pp. 174–181, 2014.
- [19] T. Chen, Y. Zhang, H. Wang et al., “Influence of pyrolysis temperature on characteristics and heavy metal adsorptive performance of biochar derived from municipal sewage sludge,” *Bioresour. Technol.*, vol. 164, pp. 47–54, 2014.
- [20] M. V. Gil, M. Martínez, S. García, F. Rubiera, J. J. Pis, and C. Pevida, “Response surface methodology as an efficient tool for optimizing carbon adsorbents for CO_2 capture,” *Fuel Processing Technology*, vol. 106, pp. 55–61, 2013.
- [21] J. Cao, Y. Wu, Y. Jin, P. Yilihan, and W. Huang, “Response surface methodology approach for optimization of the removal of chromium(VI) by $\text{NH}_2\text{-MCM-41}$,” *Journal of the Taiwan Institute of Chemical Engineers*, vol. 45, no. 3, pp. 860–868, 2014.
- [22] S. Bajpai, S. K. Gupta, A. Dey et al., “Application of Central Composite Design approach for removal of chromium (VI) from aqueous solution using weakly anionic resin: modeling, optimization, and study of interactive variables,” *Journal of Hazardous Materials*, vol. 227–228, pp. 436–444, 2012.
- [23] Z. Z. Chowdhury, S. M. Zain, R. A. Khan, A. Arami-Niya, and K. Khalid, “Process variables optimization for preparation and characterization of novel adsorbent from lignocellulosic waste,” *BioResources*, vol. 7, no. 3, pp. 3732–3754, 2012.
- [24] A. Saravanan, P. Senthil Kumar, and B. Preetha, “Optimization of process parameters for the removal of chromium(VI) and nickel(II) from aqueous solutions by mixed biosorbents (custard apple seeds and *Aspergillus niger*) using response surface methodology,” *Desalination and Water Treatment*, vol. 57, no. 31, pp. 14530–14543, 2016.
- [25] Z. Ayazi, Z. M. Khoshhesab, and S. Norouzi, “Modeling and optimizing of adsorption removal of Reactive Blue 19 on the magnetite/graphene oxide nanocomposite via response surface methodology,” *Desalination and Water Treatment*, vol. 57, no. 52, pp. 25301–25316, 2016.
- [26] T. M. Alslaibi, I. Abustan, M. A. Ahmad, and A. A. Foul, “Application of response surface methodology (RSM) for optimization of Cu^{2+} , Cd^{2+} , Ni^{2+} , Pb^{2+} , Fe^{2+} , and Zn^{2+} removal from aqueous solution using microwaved olive stone activated carbon,” *Journal of Chemical Technology and Biotechnology*, vol. 88, no. 12, pp. 2141–2151, 2013.
- [27] M. Auta and B. H. Hameed, “Optimized waste tea activated carbon for adsorption of Methylene Blue and Acid Blue 29 dyes using response surface methodology,” *Chemical Engineering Journal*, vol. 175, no. 1, pp. 233–243, 2011.
- [28] A. Witek-Krowiak, K. Chojnacka, D. Podstawczyk, A. Dawiec, and K. Pokomeda, “Application of response surface methodology and artificial neural network methods in modelling and optimization of biosorption process,” *Bioresour. Technol.*, vol. 160, pp. 150–160, 2014.
- [29] D. C. Montgomery, *Design and Analysis of Experiments*, John Wiley & Sons, 2008.
- [30] D. Ranjan, D. Mishra, and S. H. Hasan, “Bioadsorption of arsenic: an artificial neural networks and response surface methodological approach,” *Industrial and Engineering Chemistry Research*, vol. 50, no. 17, pp. 9852–9863, 2011.
- [31] J. M. Salman and B. H. Hameed, “Effect of preparation conditions of oil palm fronds activated carbon on adsorption of bentazon from aqueous solutions,” *Journal of Hazardous Materials*, vol. 175, no. 1–3, pp. 133–137, 2010.
- [32] I. Y. S. Rustom, M. H. López-Leiva, and B. M. Nair, “Optimization of extraction of peanut proteins with water by response surface methodology,” *Journal of Food Science*, vol. 56, no. 6, pp. 1660–1663, 1991.
- [33] M. I. Al-Wabel, A. Al-Omran, A. H. El-Naggar, M. Nadeem, and A. R. A. Usman, “Pyrolysis temperature induced changes in characteristics and chemical composition of biochar produced from *Conocarpus* wastes,” *Bioresour. Technol.*, vol. 131, pp. 374–379, 2013.
- [34] D. Angin, “Effect of pyrolysis temperature and heating rate on biochar obtained from pyrolysis of safflower seed press cake,” *Bioresour. Technol.*, vol. 128, pp. 593–597, 2013.
- [35] A. V. McBeath, C. M. Wurster, and M. I. Bird, “Influence of feedstock properties and pyrolysis conditions on biochar carbon stability as determined by hydrogen pyrolysis,” *Biomass and Bioenergy*, vol. 73, pp. 155–173, 2015.
- [36] A. Hmid, D. Mondelli, S. Fiore, F. P. Fanizzi, Z. Al Chami, and S. Dumontet, “Production and characterization of biochar from three-phase olive mill waste through slow pyrolysis,” *Biomass and Bioenergy*, vol. 71, pp. 330–339, 2014.
- [37] F. Ronsse, S. van Hecke, D. Dickinson, and W. Prins, “Production and characterization of slow pyrolysis biochar: influence of feedstock type and pyrolysis conditions,” *GCB Bioenergy*, vol. 5, no. 2, pp. 104–115, 2013.
- [38] R. A. Brown, A. K. Kercher, T. H. Nguyen, D. C. Nagle, and W. P. Ball, “Production and characterization of synthetic wood chars for use as surrogates for natural sorbents,” *Organic Geochemistry*, vol. 37, no. 3, pp. 321–333, 2006.
- [39] H. Yang, R. Yan, H. Chen, D. H. Lee, D. T. Liang, and C. Zheng, “Mechanism of palm oil waste pyrolysis in a packed bed,” *Energy and Fuels*, vol. 20, no. 3, pp. 1321–1328, 2006.

Research Article

Adsorption of Toluene and Paraxylene from Aqueous Solution Using Pure and Iron Oxide Impregnated Carbon Nanotubes: Kinetics and Isotherms Study

Aamir Abbas,^{1,2} Basim Ahmed Abussaud,¹ Ihsanullah,¹
Nadhir A. H. Al-Baghli,¹ and Halim Hamid Redhwi¹

¹Department of Chemical Engineering, King Fahd University of Petroleum & Minerals, Dhahran 31261, Saudi Arabia

²Department of Chemical Engineering, University of Engineering and Technology, Lahore 54890, Pakistan

Correspondence should be addressed to Basim Ahmed Abussaud; basim@kfupm.edu.sa

Received 1 January 2017; Accepted 15 February 2017; Published 12 March 2017

Academic Editor: Viktor Kochkodan

Copyright © 2017 Aamir Abbas et al. This is an open access article distributed under the Creative Commons Attribution License, which permits unrestricted use, distribution, and reproduction in any medium, provided the original work is properly cited.

Multiwalled carbon nanotubes (CNTs) and iron oxide impregnated carbon nanotubes (CNTs-iron oxide) were investigated for the adsorption of hazardous toluene and paraxylene (p-xylene) from aqueous solution. Pure CNTs were impregnated with iron oxides nanoparticles using wet impregnation technique. Various characterization techniques including thermogravimetric analysis, scanning electron microscopy, elemental dispersion spectroscopy, X-ray diffraction, and nitrogen adsorption analysis were used to study the thermal degradation, surface morphology, purity, and surface area of the materials. Batch adsorption experiments show that iron oxide impregnated CNTs have higher degree of removal of p-xylene (i.e., 90%) compared with toluene (i.e., 70%), for soaking time 2 h, with pollutant initial concentration 100 ppm, at pH 6 and shaking speed of 200 rpm at 25°C. Pseudo-second-order model provides better fitting for the toluene and p-xylene adsorption. Langmuir and Freundlich isotherm models demonstrate good fitting for the adsorption data of toluene and p-xylene.

1. Introduction

Toluene and p-xylene are produced in different refinery operations and widely utilized in different petrochemical industries as a raw material. Toluene is used as a solvent in paints, cleaners, and degreasers and can also be utilized for surface coatings. It is also used as a raw material in explosives and polyurethanes production. Xylene exists as a clear liquid and can be found in three different isomeric forms: orthoxylene (o-xylene), metaxylene (m-xylene), and paraxylene (p-xylene). It has applications as a solvent in paints removers, cleaners, and inks. P-xylene is also used in the manufacturing of terephthalic acid (PTA), a feed stock for the production of polyester resins [1, 2].

Toluene and p-xylene are hazardous chemicals for human beings and environment. They have a number of harmful effects on human health including kidney, liver, and nervous system damage [3]. It is important to remove these hazardous compounds from the water before discharging from the

facility. Removal of toluene and p-xylene was investigated heavily in the literature [4–9]. Among various methods, adsorption is the most economical, suitable, and widely practiced method for the removal of toluene, p-xylene, and other hydrocarbons from water. Researchers are in quest of the novel adsorbents with the improved adsorption capacity, high removal efficiency, easy regeneration, and handling capabilities [10, 11]. In recent years CNTs [12], a new class of materials, were introduced with high adsorption capacity and removal efficiency for removal of different organic, inorganic, and biological contaminants from water [5, 10, 11, 13–17].

CNTs have good surface modification ability and high surface area that is advantageous in many adsorption applications. CNTs modification with different functional groups resulted in higher removal efficiency of toluene and p-xylene [11, 18–22]. Metal oxide nanoparticles impregnated CNTs exhibited excellent adsorption capacity and efficiency for the removal of a number of contaminants from water [23–28].

In the present study, pure and CNTs impregnated with iron oxide nanoparticles were used for the adsorption of toluene and p-xylene from water. The synthesized materials were characterized using various material characterization tools. Batch adsorption experiments were performed and the effects of contact time, adsorption dosage, and initial concentration of adsorbate were determined on the removal of toluene and p-xylene from water. The kinetics of toluene and p-xylene were analyzed using pseudo-first-order, second-order, and intraparticle diffusion model. Adsorption isotherm studies of toluene and p-xylene were carried out using Langmuir, Freundlich, and Dubinin-Radushkevich (D-R) isotherm models.

2. Materials and Methods

2.1. Materials Synthesis. Multiwall carbon nanotubes (CNTs) with 95% purity were purchased from Chengdu Organic Chemicals Co. Ltd. (China). Iron (III) nitrate nonahydrate, $\text{Fe}(\text{NO}_3)_3 \cdot 9\text{H}_2\text{O}$ (Reagent grade Sigma-Aldrich, purity $\geq 98\%$), toluene, and p-xylene of analytical grade were purchased from Sigma-Aldrich. All chemicals were used with same purity as received. Pure CNTs were impregnated with iron oxide nanoparticles using wet impregnation technique. 18 g (90% wt. of CNTs and 10% wt. iron nitrate) of CNTs was immersed in 500 mL of ethanol (ACS spectrophotometric grade, 95.0%, Sigma-Aldrich) and the mixture was sonicated using a probe type sonicator (VCX-750, Sonics & Materials, CT, USA) for deagglomeration and proper distribution inside ethanol solvent. 2 g of iron nitrate salt was also dissolved in 100 mL ethanol and the resultant solution was added to CNTs dropwise and sonicated for proper mixing with CNTs. Solution was heated at 80–90°C in an oven overnight to evaporate the ethanol. On complete drying, sample was calcined in a furnace at 350°C for 4 hours.

2.2. Materials Characterization. Pure and impregnated CNTs were characterized using various techniques. In order to perform morphology and elemental analysis, samples were coated with 5 nm thick layer of platinum using Quorum sputter coater (Model: Q150R S). Scanning electron microscope (SEM Model: TESCAN MIRA 3 FEG-SEM) was used to analyze the morphology and structure of pure and iron oxide impregnated CNTs. Energy dispersive X-ray (EDX) was used to perform the elemental analysis of materials. Samples were also analyzed using transmission electron microscope (TEM Model JEOL JEM-2100F) to get the information about dispersion of nanoparticles on the surface of CNTs. It also provided the information about catalyst particles used for growing CNTs. TA Instrument (Model: SDTQ600) was applied for thermogravimetric analysis (TGA) of pure and impregnated CNTs. Samples were heated to 900°C, at heating rate of 10°C/min and air flow rate of 100 mL/min. This analysis performed under air provided the purity and thermal degradation of materials. X-ray diffraction (XRD) measurements of the materials were performed using XRD (Model: Bruker D8 Advance) equipped with Cu $K\alpha$ radiation source (40 kV, 20 mA) and operated at a scanning rate of 1° min⁻¹ over 2 θ

range of 10–80°. XRD provided the information about the presence of different phases in materials. Nitrogen adsorption-desorption was carried out at 77 K for determining the surface area and porosity of the materials using an automatic volumetric adsorption analyzer (Model: ASAP 2020, Micromeritics, USA). In this analysis, samples were degassed at 300°C under vacuum, prior to adsorption-desorption isotherm measurement. The surface area (S_{BET}) of the synthesized materials was calculated, based on the Brunauer-Emmett-Teller (BET) isotherm. Total pore volume and pore size distribution of the materials were determined by applying the Barrett-Joyner-Halenda (BJH) model to the adsorption isotherms [29, 30].

2.3. Toluene and p-Xylene Adsorption Experimentation. All adsorption experiments were performed in 125 mL glass flasks containing 50 mg of adsorbent and 100 mL solution. Samples were shaken on mechanical shaker (Lab Companion Model: SK-600) at 200 rpm and 25 \pm 2°C. All solutions were prepared in deionized water. Blank experiments without adding adsorbent were also carried out to confirm the adsorption on glass walls and loss due to volatilization. After shaking, the samples were filtered using filter paper of 0.45 μm pore size and analyzed. To study the effect of adsorbent amount, various amounts of adsorbent ranging from 25 to 150 mg were added to each flask containing 100 mL solution of toluene or p-xylene with initial concentration of 100 ppm. To investigate the kinetics of toluene and p-xylene adsorption, each glass flask containing 50 mg of adsorbent was filled with 100 mL of a 100 ppm toluene or p-xylene solution at 25 \pm 2°C and placed on shaker. At regular time intervals, the samples were filtered, and concentration was analyzed. For adsorption isotherms data, 100 mL samples of toluene solution of different initial concentration (20–150 ppm) were treated with 50 mg of adsorbents. Similarly, for p-xylene 100 mL samples of different initial concentration (20–100 ppm) were treated with 50 mg of adsorbents. Initial and final concentrations of toluene and p-xylene were analyzed using gas chromatograph (Model: 7890B, Agilent Corp., USA) with flame ionization detection (GC-FID) and chemical oxygen demand (COD: HACH Model DR 3900) analyzer.

For the analysis using GC-FID, 1 μL sample was injected in wax column (30 m length, 20 mm internal diameter). Temperature was raised from 40 to 100°C with ramp of 10°C/minute. Temperature of both the injection point and FID detector was 250°C. For COD analysis, 2 mL solution of toluene or p-xylene was added to ready-made vial solution and heated at 150°C for 2 hours using the furnace (HACH Model DRB 200). On completion of digestion, vials were cooled at room temperature and COD was analyzed using the spectrophotometer (HACH Model DR 3900). COD was converted to concentration using (1) and (2) for toluene and p-xylene, respectively:

$$\text{Concentration of toluene (mg/L)} = \frac{\text{COD of sample}}{3.13} \quad (1)$$

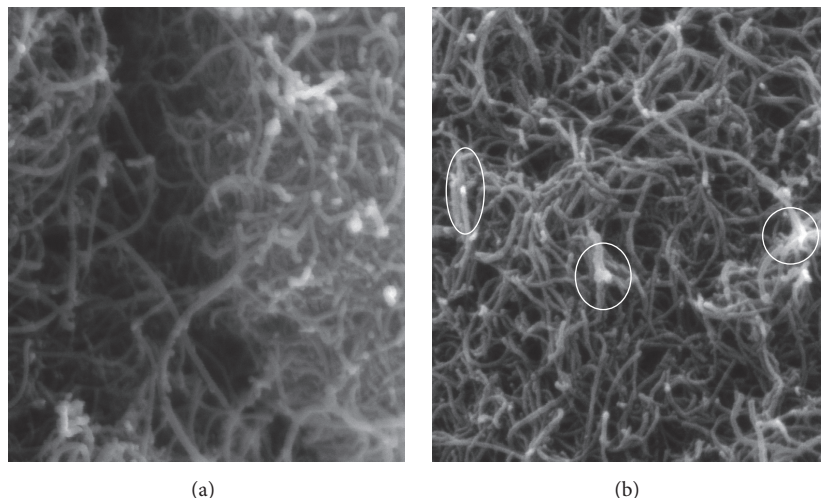


FIGURE 1: SEM images of (a) pure and (b) iron oxide impregnated CNTs conditions (voltage: 15 kV, resolution: 64 kX, and view field: 3 μm).

$$\begin{aligned} \text{Concentration of p-xylene (mg/L)} \\ = \frac{\text{COD of sample}}{3.16} \end{aligned} \quad (2)$$

Percentages of removal and adsorption capacity were calculated using (3) and (4), respectively:

$$\text{Removal efficiency (\%)} = \frac{C_o - C_t}{C_o} * 100 \quad (3)$$

$$\text{Adsorption capacity (q)} = \frac{(C_o - C_t)V}{m}, \quad (4)$$

where “ C_o ” is the initial concentration (ppm) at the start of the experiment ($t = 0$), while “ C_t ” is the concentration at time “ t ”. “ V ” is the volume (L) of the solution and “ m ” represents the amount (g) of the adsorbent dosage.

3. Results and Discussion

3.1. Characterizations of CNTs

3.1.1. Scanning Electron Microscopy. Figure 1 shows the SEM images for pure and iron oxide impregnated CNTs. Tubular geometry of both pure and iron oxide impregnated CNTs was observed and no damage was indicated in CNTs structures after impregnation. Iron oxide nanoparticles were observed in white circles in Figure 1(b). It can be seen that the dispersion of CNTs has improved after impregnation with iron oxide nanoparticles. Iron oxide nanoparticles might help to reduce the strong Van der Waals forces between CNTs, hence leading to their dispersion.

3.1.2. Energy Dispersive X-Ray Spectroscopy. Figure 2 demonstrates the EDX analysis of the materials. Analysis of the pure CNTs confirmed the presence of carbon as a main constituent. Presence of nickel was due to the catalyst particles used for growing CNTs, while platinum was used as a sputtering material. Analysis of iron oxide impregnated CNTs

indicated the presence of iron in addition to the constituents of pure sample.

3.1.3. Transmission Electron Microscopic Analysis. Figure 3 provides the TEM images for both pure and iron oxide impregnated CNTs. Highly well-ordered crystalline structure of multiwall carbon nanotubes was observed in Figure 3(a). Nickel particles used for growing CNTs were also observed in the image and indicated with arrows. Figure 3(b) provides the distribution of iron oxide nanoparticles on the surface of CNTs. Small and irregular shaped iron nanoparticles were observed in the sample. It was also observed that particles are widely distributed on the surface of CNTs with diameter range of 5–10 nm. At some locations particles also seem agglomerated making clusters.

3.1.4. Thermogravimetric Analysis. Figure 4 indicates the TGA for both pure and iron oxide impregnated CNTs. Both of the TGA curves have two main weight loss regions. Initial small weight loss of around 2% was attributed to the evaporation of physically bound water and some other lighter impurities. The second, steep and rapid weight loss region represents the combustion of CNTs. Pure CNTs showed more stability and started degrading around 550°C while degradation of iron oxide impregnated CNTs started around 500°C. This may be due to the fact that the impregnation of iron oxide nanoparticles on CNTs serves as an impurity, hence leading to steep weight loss at lower temperature [31]. Additionally, iron oxide nanoparticles reduced the agglomeration of CNTs as shown in SEM images that might also led to easy degradation [32]. Around 1% weight of the material was left at the end of the analysis for pure CNTs. This indicated the presence of nickel nanoparticles that were used as a catalyst for synthesis of CNTs. Iron oxide impregnated CNTs showed higher weight residue of around 7%, which represent the weight of iron oxide nanoparticles in addition to the nickel catalyst.

3.1.5. X-Ray Diffraction. Figure 5 shows the XRD pattern of the pure and iron oxide impregnated CNTs. XRD pattern of

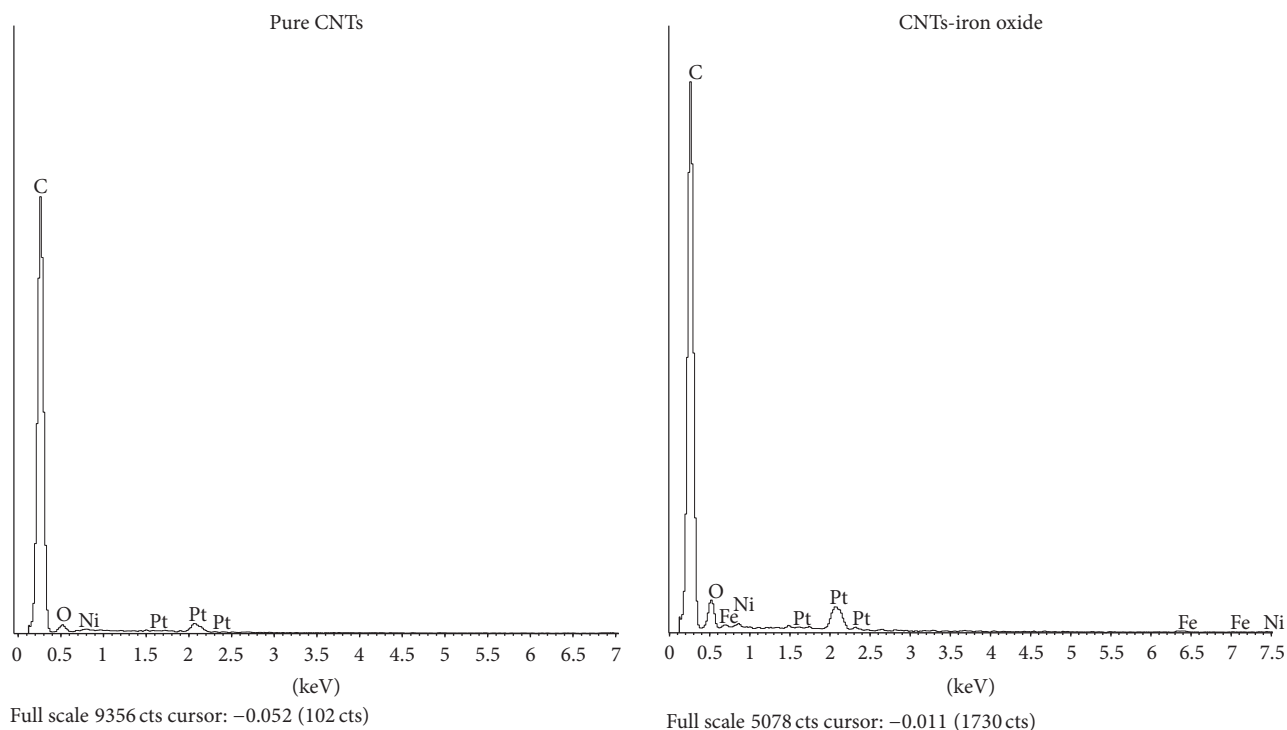


FIGURE 2: EDX analysis of pure and iron oxide impregnated CNTs.

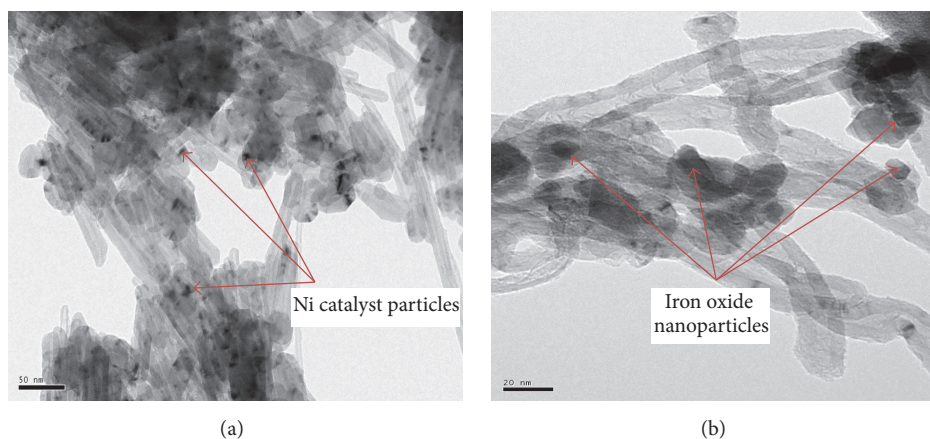


FIGURE 3: TEM images of (a) pure and (b) iron oxide impregnated CNTs.

iron oxide impregnated CNTs showed additional peaks, when compared with XRD pattern of pure CNTs. The characteristic peaks of graphite carbon were seen in both samples at 2θ of 26° and 43° that represented the presence of CNTs. Additional peaks of iron oxide in impregnated CNTs sample are indicated by the representative peaks at 2θ of 35° and 52° [33].

3.1.6. Surface Area and Pore Size Analysis. Nitrogen adsorption-desorption isotherm curves for pure and iron oxide impregnated CNTs are shown in Figure 6 and classified as Type V according to international union of pure and applied chemistry (IUPAC) classification. Type V indicates the presence of mesopores and external sites for adsorption of

molecules on the surface of pure and iron oxide impregnated CNTs. The hysteresis loop was found of type H3 in each curve and occurred due to capillary condensation [34]. Table 1 provides the BET surface area of the pure and iron oxide impregnated CNTs. It was observed that the iron oxide impregnated CNTs have higher surface area ($216 \text{ m}^2/\text{g}$) compared with pure CNTs ($138 \text{ m}^2/\text{g}$). This increase in surface area of the iron oxide impregnated CNTs might be due to improved distribution and deagglomeration of CNTs after attachment of iron oxide nanoparticles which is in accordance with Type V assumptions of mesopores and external surface availability for adsorption. Mean pore size indicates the mesopores for pure and iron oxide impregnated CNTs. Based on the results presented in Table 1, total pore

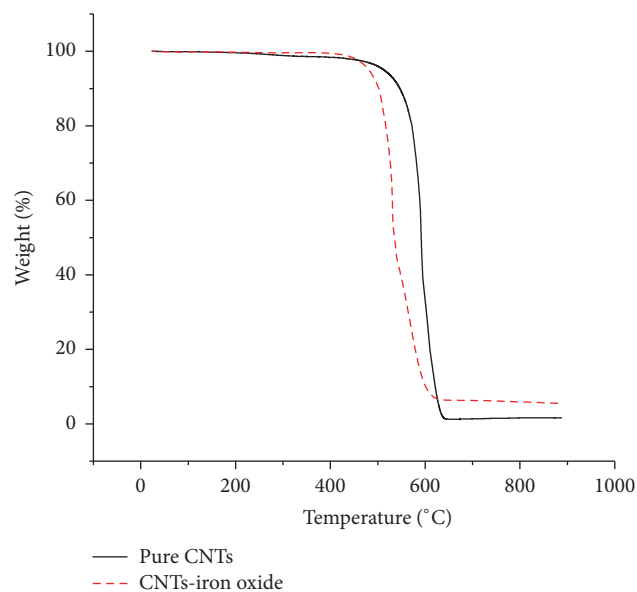


FIGURE 4: TGA plot of pure and iron oxide impregnated CNTs.

TABLE 1: Surface and structural parameters of pure and iron oxide impregnated CNTs.

Physical property	Materials	
	Pure CNTs	CNTs-iron oxide
BET surface area (m ² /g)	138	216
Total pore volume (cm ³ /g)	0.61	0.96
Cumulative pore area (m ² /g)	145	207
Mean pore radius (Å)	167	185

volume was 0.61 cm³/g for pure CNTs and 0.96 cm³/g for iron oxide impregnated CNTs. This higher surface area and pore volume of iron oxide impregnated CNTs may be useful for adsorption. Mean pore radius was found in the range of mesopores for both materials.

3.2. Adsorption Experimentation Results

3.2.1. Effect of Contact Time. Figure 7 provides the effect of contact time on the removal of toluene and p-xylene using the pure and iron oxide impregnated CNTs. The removal efficiency enhanced with increasing contact time for both pure and iron oxide impregnated CNTs until equilibrium was attained. Initially, higher removal was due to plenty of active sites available that contributed to fast removal of adsorbate molecules. With the passage of time, the number of vacant active sites reduced and removal was observed to decrease. Furthermore, layers of the adsorbed molecules offer additional resistance to the new molecules to penetrate through.

Removal of p-xylene was found to be higher compared with toluene under same experimental conditions, except initial concentration of 61 ppm for toluene and 48 ppm for p-xylene. This can be attributed to low solubility and higher hydrophobicity of p-xylene compared with toluene.

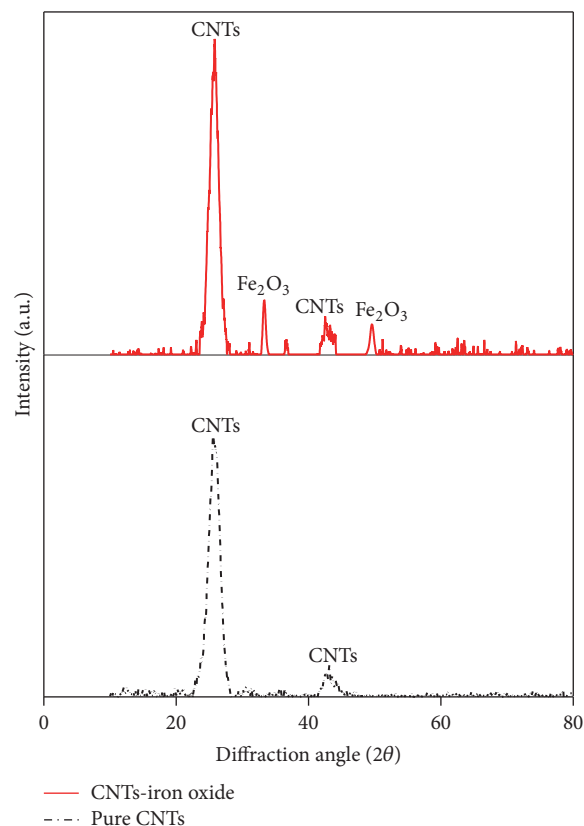


FIGURE 5: XRD analysis of pure CNTs and iron oxide impregnated CNTs.

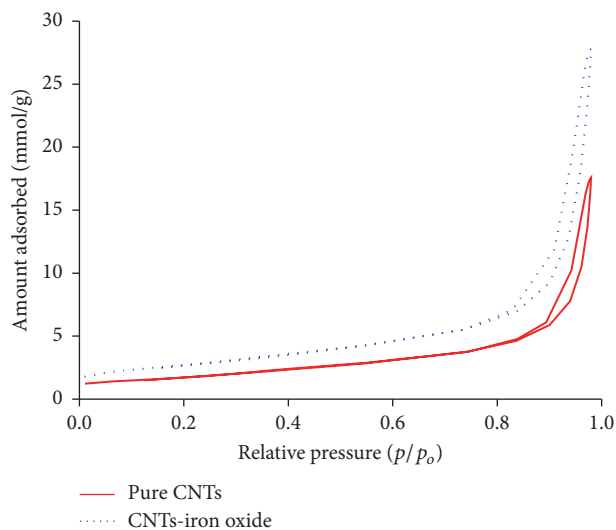


FIGURE 6: Nitrogen adsorption-desorption isotherms for pure and iron oxide impregnated CNTs.

Solubility of toluene is 530 mg/L in water while p-xylene has solubility of 150.5 mg/L. Generally, the decrease in solubility for hydrophobic organic compounds (hydrophobicity based on log K_{ow} is 2.69 for toluene and 3.15 for p-xylene) leads to increase in adsorption. Similar trends were reported for adsorption of benzene, toluene, ethylbenzene, and p-xylene

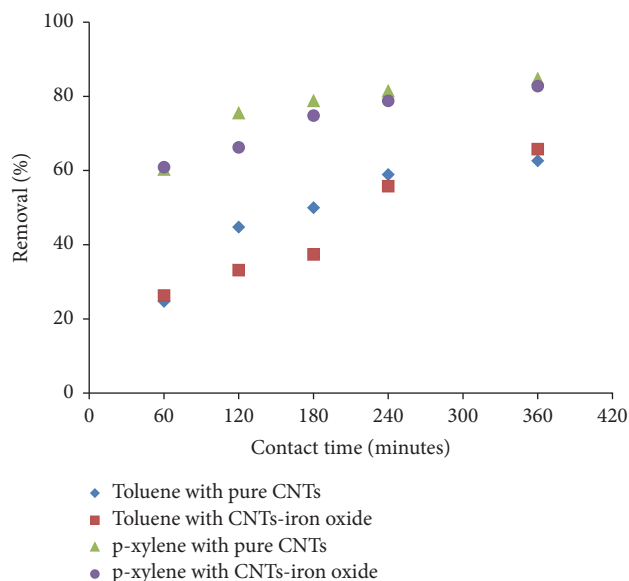


FIGURE 7: Effect of contact time on the removal of toluene and p-xylene (initial concentration: 61 mg/L for toluene and 48 mg/L for p-xylene, adsorbent dosage: 50 mg, shaking speed: 200 rpm, pH: 6, and temperature: 298 K).

using various adsorbents in some studies [18, 36]. Furthermore, it was observed that percentage removal efficiency was almost similar using pure and iron oxide impregnated CNTs for both toluene and p-xylene after 240 minutes.

3.2.2. Effect of Adsorbent Amount. Figure 8 provides effect of the adsorbent amount on the removal of both contaminants. It is obvious that with increasing amount of the adsorbent, removal of both the toluene and p-xylene increased. Higher quantity of the adsorbent provided more adsorption sites, hence leading to higher removal of the contaminants. As adsorbent dosage was increased from 25 to 100 mg, removal increased from 21 to 48% and from 16 to 52% for toluene using pure and iron oxide impregnated CNTs, respectively. Similarly, for p-xylene, by increasing the adsorbent amount from 25 mg to 75 mg, removal increased from 66 to 84% and from 68 to 80% for pure and iron oxide impregnated CNTs, respectively. Further increase in adsorbent amount does not affect much removal efficiency because it achieved the equilibrium adsorption capacity. Similar findings were also reported elsewhere [37]. Although surface area and pore volume were higher for iron oxide impregnated CNTs but it was found that the removal efficiency of both pure and impregnated CNTs was almost similar for the adsorption of toluene and p-xylene. With the same amount of the adsorbent, p-xylene showed higher removal percentage compared with toluene which was due to lower solubility and higher hydrophobicity of p-xylene.

3.2.3. Adsorption Kinetics Study. Adsorption kinetic is one of the most important factors that govern the solute uptake rate and represents the adsorption efficiency of the adsorbent. Pseudo-first-order, second-order, and Weber-Morris

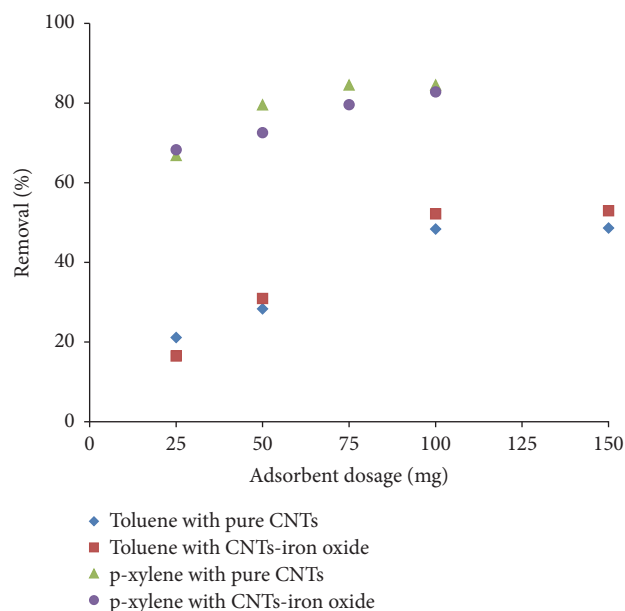


FIGURE 8: Effect of the adsorbent amount on removal of toluene and p-xylene (initial concentration: 61 mg/L for toluene and 48 mg/L for p-xylene, contact time: 2 hr, shaking speed: 200 rpm, pH: 6, and temperature: 298 K).

intraparticle diffusion model were used for the kinetics model fitting of toluene and p-xylene adsorption data. Representative equations of these models are provided below.

The Pseudo-First-Order Model

$$\ln(q_e - q_t) = \ln(q_e) - k_1 t. \quad (5)$$

The Pseudo-Second-Order Model

$$\frac{t}{q_t} = \frac{1}{k_2 q_e^2} + \frac{t}{q_e}. \quad (6)$$

The Weber-Morris Intraparticle Diffusion Model

$$q_t = k_{id} t^{0.5} + C, \quad (7)$$

where q_t and q_e are the concentrations of contaminants on adsorbent at time “ t ” and equilibrium, respectively. k_1 is pseudo-first-order model constant, k_2 is second-order model constant, and k_{id} is intraparticle diffusion model. Figure 9 indicates the fitting of experimental data with kinetics models for toluene and p-xylene.

Table 2 provides the results of the kinetics model fittings for the adsorption of toluene and p-xylene using pure and iron impregnated CNTs. It was observed that pseudo-second-order model was best to describe the adsorption of toluene and p-xylene using pure and iron impregnated CNTs. The values of regression coefficient (R^2) were highest for pseudo-second-order model ranging from 95 to 97% except for toluene adsorption using iron oxide impregnated CNTs with value of 80%. The experimentally calculated values of

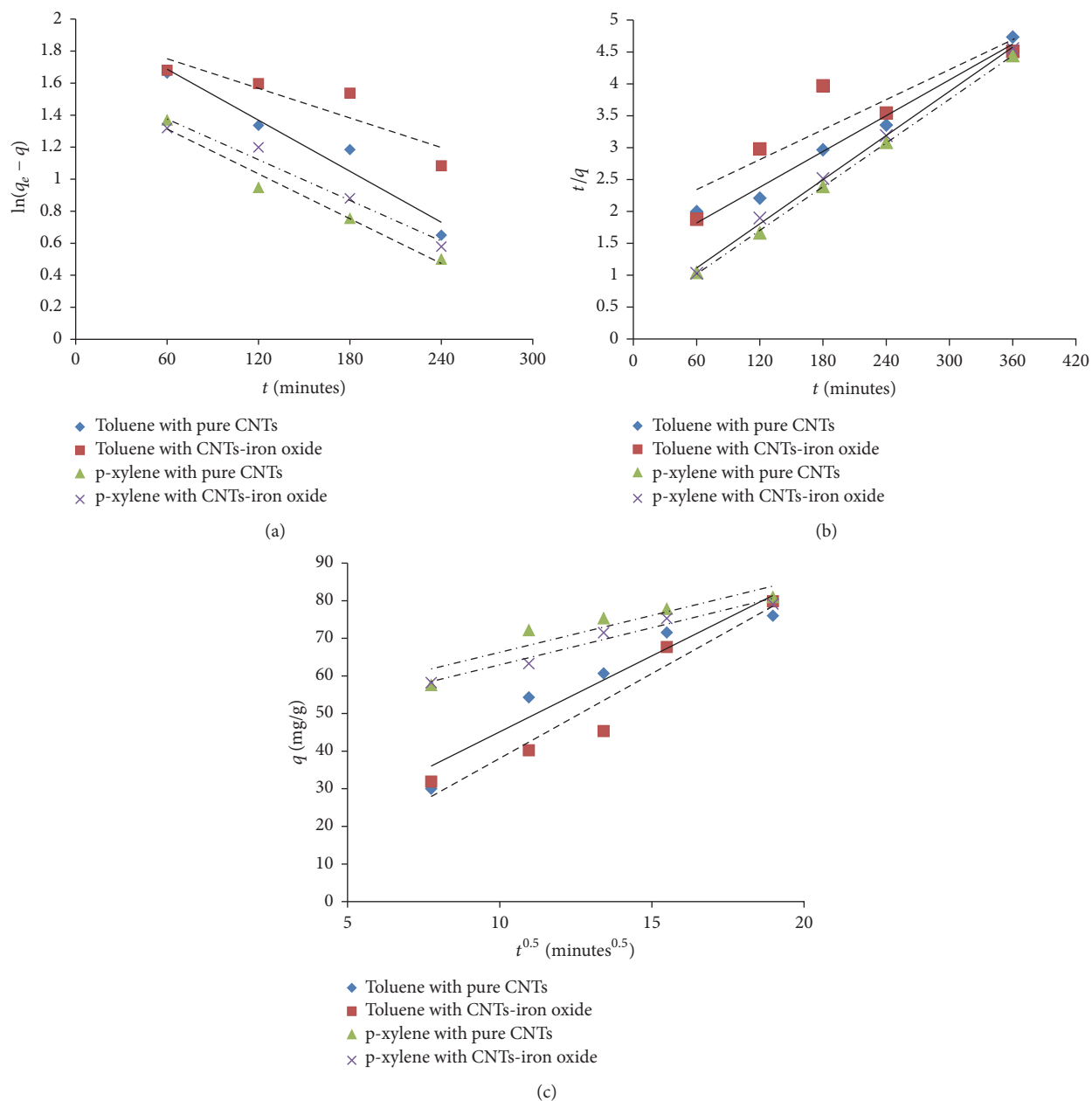


FIGURE 9: Adsorption kinetics model fitting using (a) pseudo-first-order, (b) pseudo-second-order, and (c) intraparticle diffusion model for toluene and p-xylene.

adsorption capacities were in good combination with the values obtained from pseudo-second-order model fitting. It was also noted that fitting of data using intraparticle diffusion model was linear but does not pass through the origin; therefore intraparticle diffusion is not a sole rate controlling step. Therefore, the overall adsorption kinetics might be dependent on the boundary layer diffusion in addition to the intraparticle diffusion. Similar trends were reported elsewhere [38].

It can be observed that p-xylene has higher values of the constants. This might be due to the introduction/presence of additional methyl groups in the p-xylene which may help in faster removal. One more interesting observation was

that percentage removal of p-xylene was higher compared with toluene but the adsorption capacities are lower for p-xylene using both adsorbents, which was due to lower initial concentration of p-xylene used for kinetics data as described in Section 3.2.1.

3.2.4. Adsorption Isotherms Study. Adsorption equilibrium data of the toluene and p-xylene using pure and iron oxide impregnated CNTs was fitted with Langmuir, Freundlich, and D-R isotherm model. These models have been widely used to study the adsorption of various adsorbates on CNTs. Nonlinear forms of these models were used to avoid the error due to linearization. Langmuir model best describes

TABLE 2: Adsorption kinetics parameters of toluene and p-xylene adsorption.

Model	Parameters	Toluene		p-xylene	
		Pure CNTs	CNTs-iron oxide	Pure CNTs	CNTs-iron oxide
	C_o	60.70	60.70	47.78	47.78
Experimental	$q_{e,experimental}$	76.04	79.87	81	79.11
Pseudo-first-order	$k_1 (\text{min}^{-1}) * 10^{-3}$	5.3	3.1	4.7	4.2
	$q_{e,calculated}$	7.43	6.94	4.92	5.10
	$R^2 (\%)$	95	80	97	97
Pseudo-second-order	$k_2 (\text{g mg}^{-1} \text{min}^{-1}) * 10^{-4}$	0.69	0.32	3.9	3.1
	$q_{e,calculated}$	107.53	128.21	87.72	86.96
	$R^2 (\%)$	98	80	99.9	99.7
Intraparticle diffusion model	$k_{id} (\text{g mg}^{-1} \text{min}^{-0.5})$	4.04	4.51	1.96	1.97
	C	4.74	-6.99	46.66	43.23
	$R^2 (\%)$	91	93	85	96

TABLE 3: Isotherm models parameters for toluene and p-xylene adsorption.

Model	Parameters	Toluene		p-xylene	
		Pure CNTs	CNTs-iron oxide	Pure CNTs	CNTs-iron oxide
Langmuir	$K_L (\text{L/mg})$	0.005	0.002	0.008	0.003
	$q_m (\text{mg/g})$	127.94	381.18	219.51	458.52
	$R^2 (\%)$	98.5	97.6	99.7	99.4
Freundlich	$K_F (\text{mg/g}) / (\text{mg/L})^n$	0.71	0.79	3.18	1.93
	n	1.08	0.99	1.32	1.11
	$R^2 (\%)$	98.3	97.6	99.5	99.3
Dubinin-Radushkevich (D-R)	$q_m (\text{mg/g})$	24.62	39.11	76.32	100.58
	$B (\text{mole}^2/\text{kJ}^2)$	72.87	99.73	99.81	349.98
	$E_a (\text{kJ/mole})$	0.08	0.07	0.07	0.04
	$R^2 (\%)$	99.2	99.2	99	98.4

the monolayer adsorption while Freundlich model provides information about heterogeneous adsorption on adsorbent surface [39]. Representative equations of the isotherm models are presented below.

Langmuir Isotherm Model

$$q_e = \frac{q_m K_L C_e}{1 + K_L C_e} \quad (8)$$

Freundlich Isotherm Model

$$q_e = K_F C_e^{1/n} \quad (9)$$

D-R Isotherm Model

$$q_e = q_m e^{-Be^2} \quad (10)$$

where C_e and q_e are the concentrations of contaminants in water and in adsorbent at the adsorption equilibrium, respectively. q_m is the maximum adsorption capacity; K_L is the adsorption equilibrium constant of Langmuir model; K_F and n are Freundlich constants related to the adsorption capacity and surface heterogeneity of the adsorbents, respectively. Figure 10 represents the fitting of data with isotherm

models while adsorption parameters and regression data of the models are presented in Table 3. Regression coefficient (R^2) has almost equal value for the Langmuir and Freundlich model for the adsorption of both toluene and p-xylene on pure and impregnated CNTs. It is evident from the results that values of rate constants K_L and K_F were higher for p-xylene compared with values for toluene, which can be attributed to low solubility and higher hydrophobicity of p-xylene. Lower solubility of p-xylene in water might be helpful in providing more attraction towards CNTs surface and fast adsorption rate. Values of " n " are close to 1 in all cases which indicates the suitable and uniform adsorption of toluene and p-xylene. Activation energy " E_a " was calculated using D-R isotherm model fitting. It was found that values are less than 1 which indicates physical adsorption of toluene and p-xylene molecules on the surface of adsorbents. This phenomenon can be helpful in easy regeneration of adsorbents for reuse.

3.2.5. Comparison with Existing Literature. Comparison of adsorption capacity for removal of toluene and p-xylene using single wall carbon nanotubes (SWCNTs), multiwall carbon nanotubes (CNTs), and modified CNTs is shown in Table 4. It is observed from the results of Table 4 that iron oxide impregnated CNTs have relatively higher adsorption capacity compared with other adsorbents previously reported

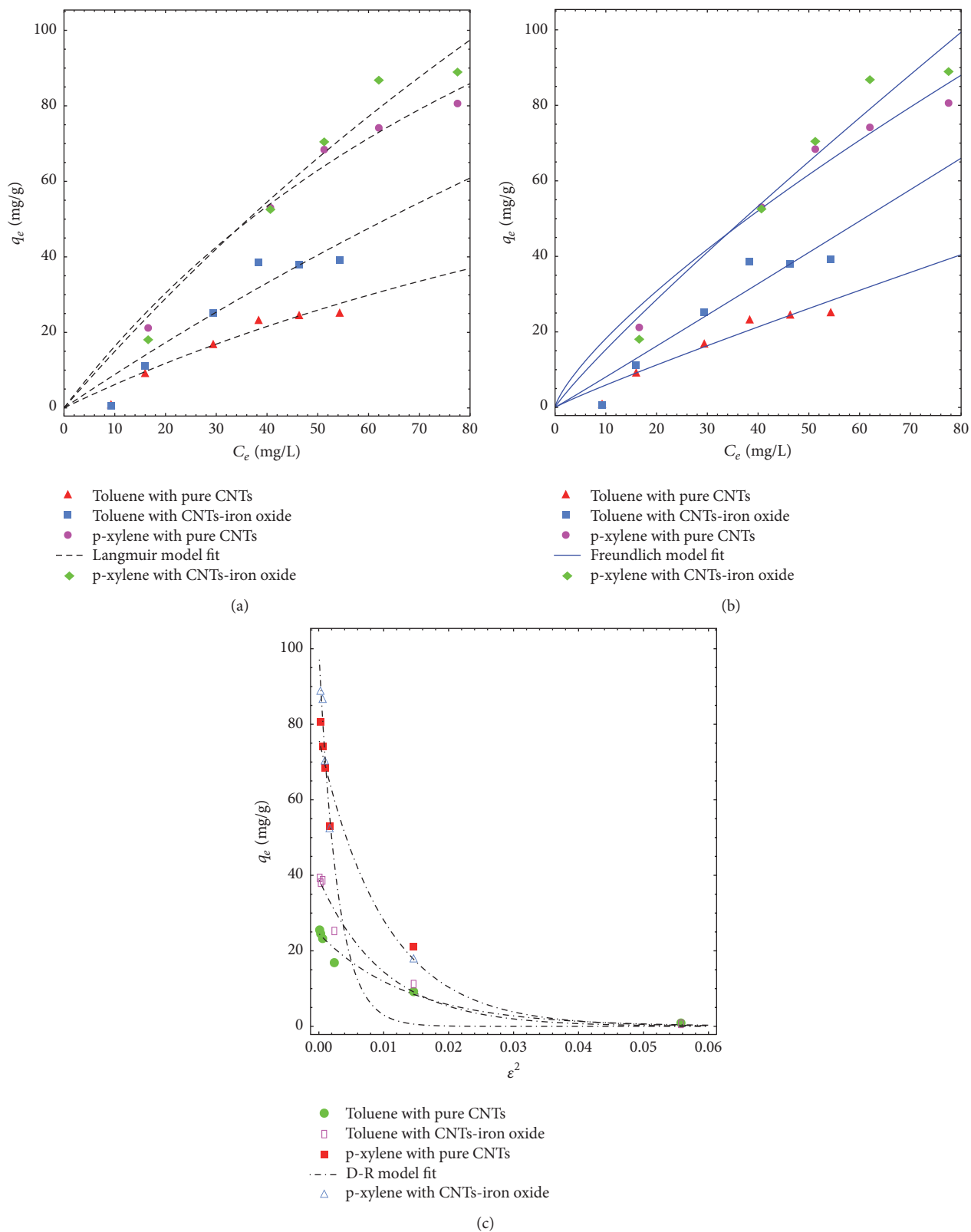


FIGURE 10: Adsorption isotherm model fitting using (a) Langmuir, (b) Freundlich, and (c) D-R model for toluene and p-xylene.

TABLE 4: Comparison of adsorption capacity of different CNTs based adsorbents for toluene and p-xylene removal.

Adsorbent	Adsorption capacity (mg/g)		Conditions	References
	Toluene	p-xylene		
CNT (NaOCl)	279.8	413.77	pH 7, T 298 K	[20]
SWCNT	—	77.5	pH 5.4, T 298 K	[22]
SWCNT (HNO ₃)	—	85.5	pH 5.4, T 298 K	[22]
CNTs-KOH	87.12	—	pH 7, T 293 K	[19]
CNT	80.1	147.8	pH 7, T 298 K	[35]
CNT (NaOCl)	252.1	318.3	pH 7, T 298 K	[35]
Pure CNTs	127.94	219.51	pH 7, T 298 K	This work
CNTs-iron oxide	381.18	458.52	pH 7, T 298 K	This work

in literature. CNTs impregnated with iron oxide can be good adsorbent for removal of toluene and p-xylene from large volume of water.

4. Conclusions

Wet impregnation technique was used for synthesizing iron oxide impregnated CNTs. Materials were characterized using SEM, EDX, TGA, XRD, and nitrogen adsorption desorption analysis. Removal of toluene and p-xylene was carried out in batch experiments and effect of contact time, adsorbent amount, and initial concentration was studied. Results demonstrate higher removal of p-xylene compared with toluene under almost similar experimental conditions. Kinetic studies show that adsorption of toluene and p-xylene obeys a pseudo-second-order model. Adsorption isotherms study indicated that Langmuir and Freundlich isotherm models demonstrate very good fit with experimental data. Adsorption capacity of p-xylene was calculated using Langmuir model fit as 219 mg/g and 458 mg/g for pure and iron oxide impregnated CNTs while it was 127 mg/g and 381 mg/g for toluene adsorption using pure and iron oxide impregnated CNTs.

Competing Interests

The authors declare that they have no competing interests.

Acknowledgments

The authors would like to acknowledge the support provided by the Chemical Engineering Department, King Fahd University of Petroleum and Minerals, Saudi Arabia.

References

- [1] J. J. McKetta Jr., *Encyclopedia of Chemical Processing and Design: Volume 67—Water and Wastewater Treatment: Protective Coating Systems to Zeolite*, CRC Press, 1999, <http://books.google.com/books?id=uDuCw37SaUMC&pgis=1>.
- [2] C. Kent, *Basics of Toxicology*, John Wiley & Sons, 1998, <http://books.google.com/books?id=VEUIWz4vQsC&pgis=1>.
- [3] US EPA, "Drinking Water Contaminants," <http://water.epa.gov/drink/contaminants/#Organic>.
- [4] B. A. Abussaud, N. Ulkem, D. Berk, and G. J. Kubes, "Wet air oxidation of benzene," *Industrial and Engineering Chemistry Research*, vol. 47, no. 13, pp. 4325–4331, 2008.
- [5] A. Fakhru'l-Razi, A. Pendashteh, L. C. Abdullah, D. R. A. Biak, S. S. Madaeni, and Z. Z. Abidin, "Review of technologies for oil and gas produced water treatment," *Journal of Hazardous Materials*, vol. 170, no. 2-3, pp. 530–551, 2009.
- [6] M. Bahmani, V. Bitarafhaghghi, K. Badr, P. Keshavarz, and D. Mowla, "The photocatalytic degradation and kinetic analysis of BTEX components in polluted wastewater by UV/H₂O₂-based advanced oxidation," *Desalination and Water Treatment*, vol. 52, no. 16-18, pp. 3054–3062, 2014.
- [7] K. Kabra, R. Chaudhary, and R. L. Sawhney, "Treatment of hazardous organic and inorganic compounds through aqueous-phase photocatalysis: a review," *Industrial and Engineering Chemistry Research*, vol. 43, no. 24, pp. 7683–7696, 2004.
- [8] M. N. Chong, B. Jin, C. W. K. Chow, and C. Saint, "Recent developments in photocatalytic water treatment technology: a review," *Water Research*, vol. 44, no. 10, pp. 2997–3027, 2010.
- [9] I. Oller, S. Malato, and J. A. Sánchez-Pérez, "Combination of advanced oxidation processes and biological treatments for wastewater decontamination—a review," *Science of the Total Environment*, vol. 409, no. 20, pp. 4141–4166, 2011.
- [10] X. Liu, M. Wang, S. Zhang, and B. Pan, "Application potential of carbon nanotubes in water treatment: a review," *Journal of Environmental Sciences*, vol. 25, no. 7, pp. 1263–1280, 2013.
- [11] O. G. Apul and T. Karanfil, "Adsorption of synthetic organic contaminants by carbon nanotubes: a critical review," *Water Research*, vol. 68, pp. 34–55, 2015.
- [12] S. Iijima, "Helical microtubules of graphitic carbon," *Nature*, vol. 354, no. 6348, pp. 56–58, 1991.
- [13] A. Abbas, B. A. Abussaud, Ihsanullah, N. A. H. Al-Baghli, M. Khraisheh, and M. A. Atieh, "Benzene removal by iron oxide nanoparticles decorated carbon nanotubes," *Journal of Nanomaterials*, vol. 2016, Article ID 5654129, 10 pages, 2016.
- [14] X. Ren, C. Chen, M. Nagatsu, and X. Wang, "Carbon nanotubes as adsorbents in environmental pollution management: a review," *Chemical Engineering Journal*, vol. 170, no. 2-3, pp. 395–410, 2011.
- [15] F. Tournus and J.-C. Charlier, "Ab initio study of benzene adsorption on carbon nanotubes," *Physical Review B*, vol. 71, no. 16, Article ID 165421, 2005.

- [16] X. Qu, P. J. Alvarez, and Q. Li, "Applications of nanotechnology in water and wastewater treatment," *Water Research*, vol. 47, no. 12, pp. 3931–3946, 2013.
- [17] L. M. Woods, Ş. C. Bădescu, and T. L. Reinecke, "Adsorption of simple benzene derivatives on carbon nanotubes," *Physical Review B*, vol. 75, no. 15, Article ID 155415, 2007.
- [18] F. Yu, J. Ma, and Y. Wu, "Adsorption of toluene, ethylbenzene and xylene isomers on multi-walled carbon nanotubes oxidized by different concentration of NaOCl," *Frontiers of Environmental Science and Engineering in China*, vol. 6, no. 3, pp. 320–329, 2012.
- [19] F. Yu, Y. Wu, X. Li, and J. Ma, "Kinetic and thermodynamic studies of toluene, ethylbenzene, and m-xylene adsorption from aqueous solutions onto KOH-activated multiwalled carbon nanotubes," *Journal of Agricultural and Food Chemistry*, vol. 60, no. 50, pp. 12245–12253, 2012.
- [20] F. Su, C. Lu, and S. Hu, "Adsorption of benzene, toluene, ethylbenzene and p-xylene by NaOCl-oxidized carbon nanotubes," *Colloids and Surfaces A: Physicochemical and Engineering Aspects*, vol. 353, no. 1, pp. 83–91, 2010.
- [21] C.-J. M. Chin, M.-W. Shih, and H.-J. Tsai, "Adsorption of non-polar benzene derivatives on single-walled carbon nanotubes," *Applied Surface Science*, vol. 256, no. 20, pp. 6035–6039, 2010.
- [22] C.-J. M. Chin, L.-C. Shih, H.-J. Tsai, and T.-K. Liu, "Adsorption of o-xylene and p-xylene from water by SWCNTs," *Carbon*, vol. 45, no. 6, pp. 1254–1260, 2007.
- [23] B. Abussaud, H. A. Asmaly, Ihsanullah et al., "Sorption of phenol from waters on activated carbon impregnated with iron oxide, aluminum oxide and titanium oxide," *Journal of Molecular Liquids*, vol. 213, pp. 351–359, 2016.
- [24] Ihsanullah, F. A. Al-Khaldi, B. Abusharkh et al., "Adsorptive removal of cadmium(II) ions from liquid phase using acid modified carbon-based adsorbents," *Journal of Molecular Liquids*, vol. 204, pp. 255–263, 2015.
- [25] H. A. Asmaly, B. Abussaud, Ihsanullah et al., "Evaluation of micro- and nano-carbon-based adsorbents for the removal of phenol from aqueous solutions," *Toxicological and Environmental Chemistry*, vol. 97, no. 9, pp. 1164–1179, 2015.
- [26] H. A. Asmaly, B. Abussaud, Ihsanullah, T. A. Saleh, V. K. Gupta, and M. A. Atieh, "Ferric oxide nanoparticles decorated carbon nanotubes and carbon nanofibers: from synthesis to enhanced removal of phenol," *Journal of Saudi Chemical Society*, vol. 19, no. 5, pp. 511–520, 2015.
- [27] Ihsanullah, H. A. Asmaly, T. A. Saleh, T. Laoui, V. K. Gupta, and M. A. Atieh, "Enhanced adsorption of phenols from liquids by aluminum oxide/carbon nanotubes: comprehensive study from synthesis to surface properties," *Journal of Molecular Liquids*, vol. 206, pp. 176–182, 2015.
- [28] Ihsanullah, F. A. Al-Khaldi, B. Abu-Sharkh et al., "Effect of acid modification on adsorption of hexavalent chromium (Cr(VI)) from aqueous solution by activated carbon and carbon nanotubes," *Desalination and Water Treatment*, vol. 57, no. 16, pp. 7232–7244, 2016.
- [29] W. Stefaniak, J. Goworek, and B. Biliński, "Pore size analysis by nitrogen adsorption and thermal desorption," *Colloids and Surfaces A: Physicochemical and Engineering Aspects*, vol. 214, no. 1-3, pp. 231–237, 2003.
- [30] N. Wibowo, L. Setyadi, D. Wibowo, J. Setiawan, and S. Ismadji, "Adsorption of benzene and toluene from aqueous solutions onto activated carbon and its acid and heat treated forms: influence of surface chemistry on adsorption," *Journal of Hazardous Materials*, vol. 146, no. 1-2, pp. 237–242, 2007.
- [31] R. H. Gangupomu, M. L. Sattler, and D. Ramirez, "Comparative study of carbon nanotubes and granular activated carbon: physicochemical properties and adsorption capacities," *Journal of Hazardous Materials*, vol. 302, pp. 362–374, 2016.
- [32] Ihsanullah, A. M. Al Amer, T. Laoui et al., "Fabrication and antifouling behaviour of a carbon nanotube membrane," *Materials and Design*, vol. 89, pp. 549–558, 2016.
- [33] Ihsanullah, T. Laoui, A. M. Al-Amer et al., "Novel anti-microbial membrane for desalination pretreatment: a silver nanoparticle-doped carbon nanotube membrane," *Desalination*, vol. 376, pp. 82–93, 2015.
- [34] K. S. W. Sing, D. H. Everett, R. A. W. Haul et al., "Reporting physisorption data for gas/solid systems with special reference to the determination of surface area and porosity," *Pure and Applied Chemistry*, vol. 57, no. 4, pp. 603–619, 1985.
- [35] C. Lu, F. Su, and S. Hu, "Surface modification of carbon nanotubes for enhancing BTEX adsorption from aqueous solutions," *Applied Surface Science*, vol. 254, no. 21, pp. 7035–7041, 2008.
- [36] Z. Yang, J. Liu, X. Yao, Z. Rui, and H. Ji, "Efficient removal of BTEX from aqueous solution by β -cyclodextrin modified poly(butyl methacrylate) resin," *Separation and Purification Technology*, vol. 158, pp. 417–421, 2016.
- [37] H. Shakeri, M. Arshadi, and J. W. L. Salvacion, "Removal of BTEX by using a surfactant—bio originated composite," *Journal of Colloid and Interface Science*, vol. 466, pp. 186–197, 2016.
- [38] F. Wang, W. Sun, W. Pan, and N. Xu, "Adsorption of sulfamethoxazole and 17 β -estradiol by carbon nanotubes/CoFe₂O₄ composites," *Chemical Engineering Journal*, vol. 274, pp. 17–29, 2015.
- [39] H. Ding, X. Li, J. Wang, X. Zhang, and C. Chen, "Adsorption of chlorophenols from aqueous solutions by pristine and surface functionalized single-walled carbon nanotubes," *Journal of Environmental Sciences*, vol. 43, pp. 187–198, 2016.

Review Article

Hazardous Effects of Titanium Dioxide Nanoparticles in Ecosystem

Syed Niaz Ali Shah,^{1,2} Zahir Shah,^{3,4} Muzammal Hussain,³ and Muzaffar Khan⁴

¹Department of Chemistry, Quaid-i-Azam University, Islamabad, Pakistan

²Department of Chemistry, Tsinghua University, Beijing 100084, China

³Guangzhou Institutes of Biomedicine and Health, Chinese Academy of Sciences, 190 Kaiyuan Avenue, Science Park, Guangzhou 510530, China

⁴Department of Biochemistry, Faculty of Biological Sciences, Quaid-i-Azam University, Islamabad, Pakistan

Correspondence should be addressed to Syed Niaz Ali Shah; niazalianalyst@gmail.com and Zahir Shah; zahir@gibh.ac.cn

Received 23 December 2016; Accepted 8 February 2017; Published 8 March 2017

Academic Editor: Muataz A. Atieh

Copyright © 2017 Syed Niaz Ali Shah et al. This is an open access article distributed under the Creative Commons Attribution License, which permits unrestricted use, distribution, and reproduction in any medium, provided the original work is properly cited.

Although nanoparticles (NPs) have made incredible progress in the field of nanotechnology and biomedical research and their applications are demanded throughout industrial world particularly over the past decades, little is known about the fate of nanoparticles in ecosystem. Concerning the biosafety of nanotechnology, nanotoxicity is going to be the second most priority of nanotechnology that needs to be properly addressed. This review covers the chemical as well as the biological concerns about nanoparticles particularly titanium dioxide (TiO₂) NPs and emphasizes the toxicological profile of TiO₂ at the molecular level in both in vitro and in vivo systems. In addition, the challenges and future prospects of nanotoxicology are discussed that may provide better understanding and new insights into ongoing and future research in this field.

1. Introduction

In the last decade, nanoscience has flourished a lot with rapidly advancing nanotechnology and its wider applications [1]. Nanomaterials (NMs) are being and have been exclusively developed and extensively used in a wide variety of products, including medicine, industry, personal care products [2, 3], cosmetics [4], sunscreens [5], toothpastes [6], paints, optics and electronics [7, 8], photocatalysts, antiultraviolet light agents [9], food packaging, medical devices, bandages, clothing, dental restoration material and water treatment facilities [10, 11], antibacterial agents [12], drug delivery systems, artificial organ, and tissue adhesives [13], and for cancer cells apoptosis under UV irradiations (Figure 1) [14]. Moreover, the nanoparticles (NPs) are eminent candidates to overcome drug resistance posed by microorganisms, a major challenge to scientific community [15]. Currently, more than 1000 products or product lines in market contain NPs [16, 17], and it has been estimated that the engineered NMs had reached 2.5 trillion US\$ annual profit by 2015 [17]. Nevertheless, the

consequently increasing interactions of NPs with biological, chemical, and ecosystems have raised concerns regarding their general and occupational health and safety profiles. The NPs enter the environment and affect both biotic and abiotic components of the ecosystem [18], including human beings [19]. The aquatic ecosystem has also been contaminated with NPs and their negative impacts suppress the immune system of fish and invertebrates [10].

Among the NPs, titanium dioxide NPs (TiO₂ NPs) are one of the most highly manufactured and widely used in the world [20]. TiO₂ is a well-known semiconductor and a versatile compound that exists in three crystalline forms, anatase, rutile, and brookite [14, 21], which can only be activated with UV light due to its high band gap energy (3.0 eV for rutile phase and 3.2 eV for anatase phase). The anatase and rutile forms have natural and industrial importance, while the brookite is rarely used. Generally, anatase is more toxic than rutile and, unfortunately, being used abundantly [21, 22]. Many researchers have contributed to the use of TiO₂ NPs in in vitro and in vivo systems. However,

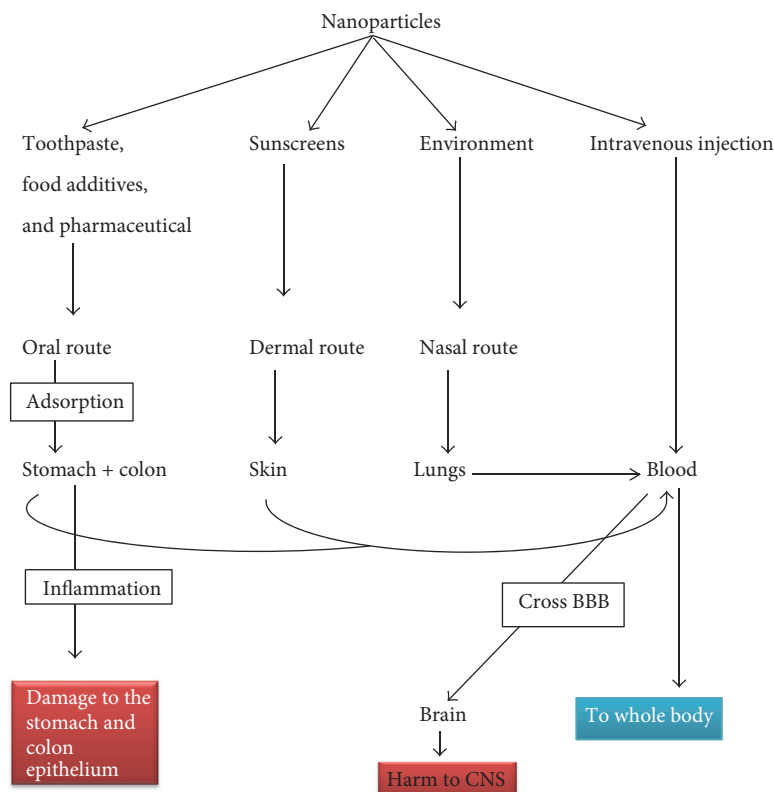


FIGURE 1: Nanoparticles containing products and their entrance ways into the biological system.

there is a lack of an overall evaluation of their toxicological effects in terms of harmful interactions with the biological and chemical systems and the environment. This review, therefore, specifically intends to provide a brief insight into the toxicological profile of TiO_2 NPs with respect to biological and ecosystems.

2. Confliction about the Toxicological Impacts of TiO_2 NPs

TiO_2 is known for long time as “the environmental white knight” due to its limited toxicity [23], inertness, and biocompatibility [8, 24]. The lethal dose at 50% concentration (LD_{50}) of TiO_2 is greater than 10 g/kg [25], and it has been approved as a food additive since 1996 by the Food and Drug Administration (FDA). The FDA and Environmental Protection Agency (EPA) have specified 50 $\mu\text{g}/\text{kg}$ body weight/day of nano- TiO_2 (nTiO_2) as safe dose for humans (Title 21, volume 1, revised as of April 1, 2014). Moreover, the European Commission’s Scientific Committee on Food (SCF), the Joint Expert Committee on Food Additives of the Food and Agriculture Organization/World Health Organization (JECFA), and the European Food Safety Authority (EFSA)’s Scientific Panel on Food Additives, Flavorings, Processing Aids and Materials in Contact with Food have also approved the daily intake of nano- TiO_2 in general food stuff. Looking from the perspective of potential adverse health effects, several experimental and epidemiological data have demonstrated that TiO_2 is biologically inactive and physiologically inert,

exhibiting relatively low toxicity, thus posing low risk to humans [26]. For example, in a study of chronic toxicity and carcinogenicity, a total of Fischer 344 rats and B6C3F1 mice at concentration of 0, 25000, and 50000 mg TiO_2/kg diet for 103 weeks (2 years) showed no significant toxicity. In the same study, TiO_2 coated mica at 0, 1, 2, and 5% in Fischer 344 rats for 130 weeks (2 and half years) had no toxicological or carcinogenic effects [27]. Furthermore, the intraperitoneal injections (IP) of TiO_2 NPs (5 mg/kg) for 14 days caused no significant adverse effects on mouse kidney [28]. Similarly, both the JECFA and EFSA evaluations of TiO_2 showed that there is no absorption or tissue storage of TiO_2 , as well as no health hazard effects for occupational workers and public health by Material Safety Data Sheets (MSDS) [8]. In addition, the World Health Organization (WHO)’s Environmental Health states that “titanium compounds are poorly absorbed from the gastrointestinal tract, which is the main route of exposure for the general population” (WHO 1982), and they pose low hazard potential in mammals or aquatic species (*Daphnia magna*, *Oncorhynchus mykiss*) [29]. Keeping in view the above-mentioned data, it is obvious to accept that the TiO_2 NPs are health friendly and nontoxic to biological environment.

Contrarily, the Scientific Committee on Consumer Safety (SCCS) has described the genotoxic, carcinogenic, and photosensitization behavior of TiO_2 NPs (SCCS/1516/13), and several in vitro and in vivo studies have shown the adverse effects of TiO_2 NPs in biological systems [30, 31]. Recently, Yin et al. [8] have shown that all the molecular sizes

and crystal forms (anatase and rutile) of nTiO₂ may cause phototoxicity [mainly caused by reactive oxygen species (ROS)] under UV irradiations [8] and exert acute toxicity in mice at different dosages of 0, 324, 648, 972, 1296, 1944, or 2592 mg/kg body weight [32]. ROS may further upregulate the inflammatory cytokines and apoptosis-related genes [24, 33, 34], inhibit the heat shock proteins (HSP) [24, 35], and cause neuroinflammation (Figure 4) [36]. The small size (10–20 nm) TiO₂ NPs may induce oxidative DNA damage, lipid peroxidation, and increased hydrogen peroxide (H₂O₂) and nitric oxide production in BEAS-2B cells (human bronchial epithelial cell line) without photoactivation [35, 37]. Collectively, on the basis of above-described data, it seems that there is no clear-cut evidence regarding the safe dose of TiO₂ NPs and great attention is needed while dealing with these nanomaterials.

3. Biological Perspective

NPs, being the advent of nanotechnology, have great impact on the environment. Their production and consumption are increasing day by day, which ultimately has increased the contact chances of NPs with the environment. How do these NPs enter the biological system? What mechanism do they follow? And what are the consequences to the cell viability? To answer these questions, one needs to look very carefully while dealing with NPs in in vivo or in vitro studies as discussed in detail in the next sections.

3.1. Biological Uptake of TiO₂ NPs and Their Entry into the Human Cells. The cellular responses toward NPs depend not only on the properties of NPs, but also on the genetic, transcriptomic, and proteomic landscape of the target cells, imparting different cytotoxic and genotoxic outcomes in various cell types [38]. TiO₂ NPs enter the human body through several ways, including inhalation, ingestion (food stuffs and daily use materials), skin uptake (through skin lesions), and medical injections [39], and may be distributed to different body organs through circulatory system (Figure 1). After internalization, the TiO₂ NPs interact with cytoplasmic proteome and bring posttranslational modifications, such as acetylation (A549 cells), by oxidative stress and other mechanisms (Figure 3) [39, 40]. They reach the periregion of nucleus, impede the function of endoplasmic reticulum, and block the nuclear pore or enter the nucleus. Inside the nucleus, they interact with DNA [35] and cause the upregulation of cytokines-, oxidative stress-, and apoptosis-related genes [23, 24, 37]. Meanwhile, the defense system of the cell responds in such a way that the first-line defense is provided by superoxide dismutase (SOD) and catalase (CAT) against oxygen toxicity (ROS), and neutrophils participate against foreign particles (discussed in NETosis pathway in Section 3.2). The transformation of oxy-radicals occurs, such that superoxide radical $\cdot\text{O}_2^-$ is dismutated to O₂ and H₂O₂ by catalytic activity of SOD enzyme and, then, CAT converts the H₂O₂ into water and oxygen. Oxidative stress (ROS) pathway is one of the mechanisms through which TiO₂ and Ag NPs exert their toxic effects and disturb the life cycle of

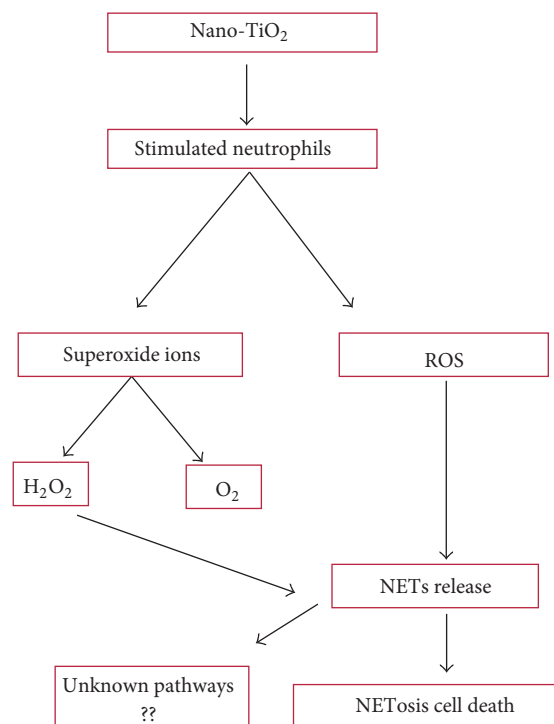


FIGURE 2: Nano-TiO₂-induced NETosis cell death pathway.

Drosophila via enhanced ROS generation and DNA damage that lead to related adverse consequences (Figure 3) [7, 41]. In sertoli cells (testicular), the exposure of TiO₂ NPs (2.5, 5, or 10 mg/kg body weight) may cause severe testicular oxidative damage, apoptosis, ROS generation, and lipid peroxidation. TiO₂ NPs may also cause suppression of SOD, CAT, glutathione peroxidase (GPx), glutathione S epoxide transferase (GST), glutathione reductase (GR), Cytochrome P450, Family 1, Subfamily B, Polypeptide 1 (Cyp1b1), carbonic anhydrase III (Car3), Bcl-2, acetyl-coenzyme A acyltransferase 2 (Acaa2), and Axin upregulated 1 (Axud1) in mouse testis, while enhancing the expression of apoptotic genes in mouse testis [42]. Moreover, the reverse correlation between ROS generation and reduction of glutathione (GSH) in human hepatocellular carcinoma cell line (SMMC-7721), rat hepatocarcinoma cell line (CBRH-7919), human liver cell line (HL-7702), and rat liver cell line (BRL-3A) has shown the toxicity of TiO₂ NPs [13].

3.2. NETosis Pathway. Neutrophils, the first line of immune defense, have the ability to extrude their DNA (either mitochondrial or nuclear) along with bactericidal, fungal, and protozoal pathogen molecules, thus creating neutrophils extracellular traps (NETs) and releasing them to the extracellular environment. The NETosis pathway is elicited by respiratory burst and ROS generation, causing release of NETs due to formation of superoxide ions. The H₂O₂ in phagosome consequently leads to NETs release and NETosis via triggering of the downstream signaling pathways (Figure 2). Exposure of neutrophils to nTiO₂ may lead to an increased oxidative burst that coincides with NETs release

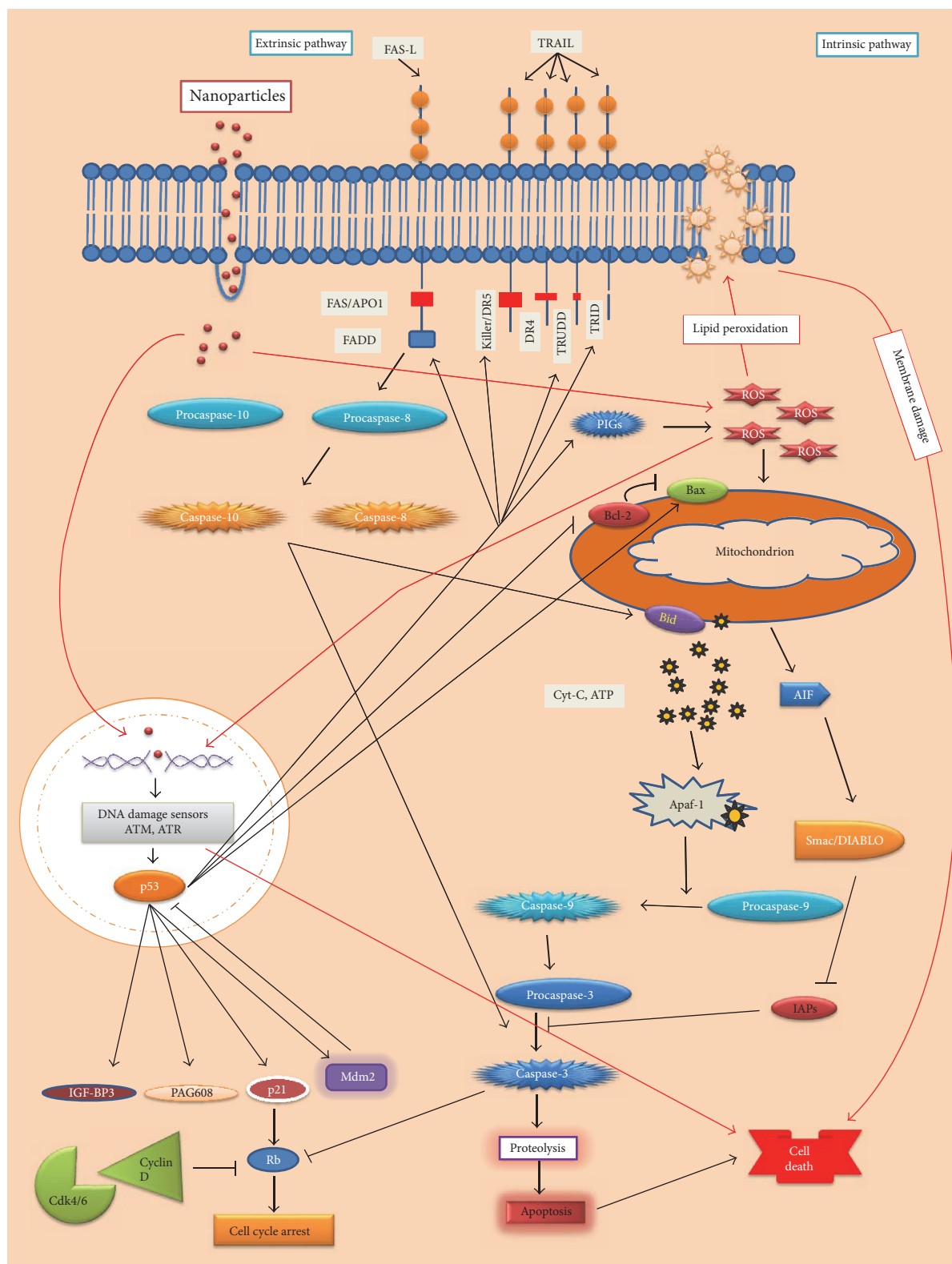


FIGURE 3: The apoptosis induced by TiO_2 NPs. The TiO_2 NPs-induced apoptosis mostly follows the intrinsic pathway. TiO_2 NPs enter the cell, induce ROS generation, and then enter the nucleus causing DNA damage. The DNA damage is sensed by sensor proteins (ATM/ATR) as a consequence of which p53 is upregulated, which further activates Bax (promoter of apoptosis) and inhibits Bcl2 (inhibitor of Bax).

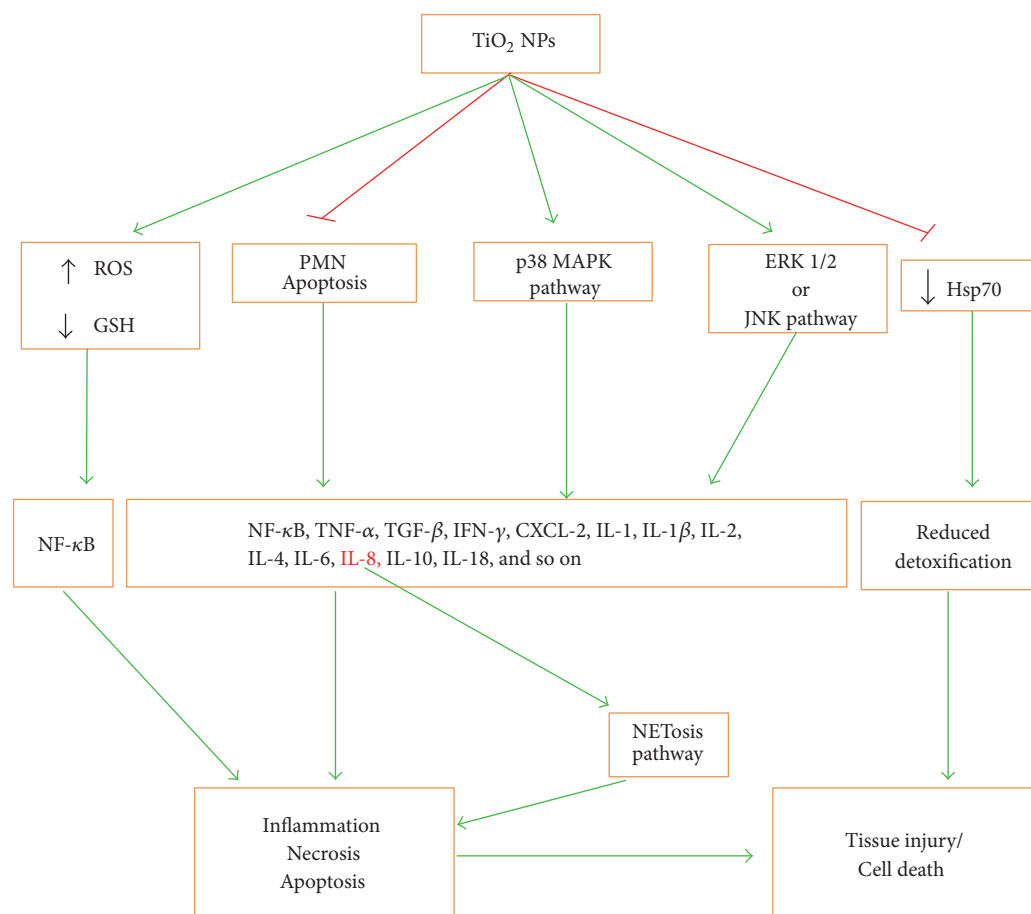


FIGURE 4: Nano-TiO₂-induced tissue injury and inflammation. These NPs cause elevation of ROS, decline of GSH levels, inhibition of PMN apoptosis, and tyrosine phosphorylation of p38MAPK and ERK1/2 or JNK. All these induce the production of different inflammatory cytokines that in turn lead to inflammation and consequent necrosis or apoptosis mechanism of cell death. Decreased detoxification due to CYP1A and HSP70 decline also leads to tissue injury or cell death.

[43]. The NETosis is often accompanied by cell death in order to control and limit extracellular infections, which may otherwise cause complicated human diseases, including sepsis and autoimmune disorders [44, 45].

3.3. Apoptosis Mediated by TiO₂ NPs. Generally, cells remain under constant threats from the cytotoxic and mutagenic effects of DNA damaging agents comprising endogenous (e.g., ROS) and exogenous (such as UV light, ionizing radiations, and other agents like chemicals in foodstuffs, water, or air) or both. Upon DNA damage, the cells undergo either DNA repair or cell cycle arrest leading to apoptosis [46]. Apoptosis is the best described mechanism through which NPs may exert their toxic effects inducing (a) an intrinsic pathway, mediated by mitochondria, or (b) an extrinsic pathway, mediated by death receptors.

TiO₂ NPs have been shown to induce apoptosis via intrinsic pathway in human bronchial epithelial cell line (BEAS-2B), independent of caspase 8/t-Bid (involved in extrinsic pathway), by enhancing ROS level and proinflammatory responses [28, 33]. During this pathway mitochondrial membrane permeability is enhanced because of caspase-3 release

and subsequent PARP cleavage and release of cytochrome C, followed by induction of caspase-9 and caspase-3 (effector caspases) of apoptosis-inducing factor. The genotoxic effect of TiO₂ NPs upregulates p53 gene that promotes the expression of Bax genes by suppressing Bcl-2 family regulator proteins, thus making an ease for opening the mitochondrial channels and release of cytochrome C (Figure 3) [7, 37, 47]. The accumulation of TiO₂ NPs in mouse neurons manifests the apoptotic markers such as nuclear shrinkage and chromatin condensation [47]. Furthermore, TiO₂ NPs may cause the upregulation of oxidative-stress-related genes, including heme oxygenase-1, thioredoxin reductase, glutathione-S-transferase, and cytokines such as interleukin-(IL-) 1, IL-2, IL-4, IL-5, IL-6, IL-8, IL-10, IL-12, IL-18, and IL-1β, transforming growth factor- (TGF-) β, tumor necrosis factor- (TNF-) α, and interferon- (IFN-) γ (Figure 4), which may cause inhibition of HSP70. The IL-8 gene expression is induced via p38 mitogen-activated protein kinase (MAPK) pathway and/or extracellular signal (ERK) pathway [24, 35]. Similarly, the intragastric exposure of TiO₂ (2.5, 5, and 10 mg/kg) in mouse may lead to their accumulation

in kidneys, inducing necrosis and inflammatory responses (Figure 3) [24].

3.4. Phototoxicity and Genotoxicity. TiO₂ NPs induce phototoxicity upon UV irradiations. They have been shown to induce apoptosis by activating apoptosis-inducing factor (AIF) in human keratinocyte cells [48], as well as in retinal pigment epithelial cells (Figure 3) [2]. Moreover, TiO₂ NPs have been demonstrated to cause pericardial oedema and premature hatch of *Japanese medaka* (*Oryzias latipes*) embryos when treated with aqueous suspensions at 0 and 14 µg/mL [49].

The genotoxicity of TiO₂ NPs attributes to ROS generation and oxidative stress in human epidermal cells, which elicits signal transduction pathways leading to apoptosis or cellular death [33]. They have been shown to induce DNA double-strand breakage in bone marrow and human amnion epithelial (WISH) cells, as well as in mice in a dose-dependent manner, leading to cell cycle arrest [50–52]. The induction of ROS may reduce NADH levels, impairing mitochondrial membrane potential ($\Delta\Psi_m$) and causing mitochondrial dysfunction [53]. The exposure of TiO₂ and Al₂O₃ NPs may also cause genotoxic effects in Chinese hamster ovary after 24 h treatment [54]. The genotoxicity, apoptosis, and mitotic arrest are caused by both nano- and microparticles of TiO₂ in various tissues of mice [4], as mentioned by SCCS in 2013 (SCCS/1516/13) (discussed in Section 2).

In human lymphocytes, TiO₂ NPs have been found genotoxic at a dose of 0.25 mM probably by the lipid peroxidation mechanism and at 4 mM to *Allium cepa* [55]. The viability of human epidermal cells was significantly decreased due to DNA damage, micronucleus formation, and reduction in glutathione [14]. They were readily uptaken by A549 cells (carcinomic human alveolar basal epithelial cells) in vitro. However, such rapid uptake was in contrast with a very low oral absorption in a differentiated Caco-2 monolayer system (human epithelial colorectal adenocarcinoma cells) and after oral gavage administration to rats [56]. The calculation of uptake, dispersion, and biological effects of ingested NMs is complicated in vivo due to interindividual differences in the composition, pH, thickness of the mucus layer, gastrointestinal flora, and gastrointestinal passage time [57]. The in vitro studies of NPs interactions are unrealistic and may not indicate the actual fate of NPs, while in in vivo studies, the biological molecules are absorbed on the surface of NPs, changing their biokinetics and the consequent fate of the biomolecules in natural environment [58].

3.5. Neurotoxicity. Brain tissues are more susceptible to oxidative stress-induced damage because of high metabolic rate, cellular content of lipids, proteins, and extensive axonal and dendritic networks, and low levels of endogenous scavengers. After exposure of TiO₂ NPs, the integrity of blood brain barrier (BBB) is badly affected due to persistence of NPs in endothelial cells or via infiltration of immune cells, resulting in breakdown of BBB. In an experimental study, the TiO₂ NPs have been demonstrated to cause injury to neurons via JNK/p53-mediated-apoptosis and ROS generation, which activated downstream p53/p21 pathway, causing G2/M arrest

in in vitro model of dopaminergic neurons (PC12 cell) (Figure 3) [21, 59]. In another study, the TiO₂ NPs were found to enter the brain via olfactory bulb and reside in the hippocampus region, damaging mitochondria and inducing oxidative stress in rat and human glial cell lines [60]. The anatase nano-TiO₂ are more toxic to neuronal cells than rutile [21]. Whether these findings have definite neurotoxic implications needs further investigations.

3.6. Respiratory Toxicity. The exposures of NMs via inhalation (occupational and/or environmental) may affect the respiratory tract, resulting in an increased risk of lung cancer, fibrosis, blockage of interalveolar areas, and presence of inflammatory cells [17, 61]. The natural and engineered NPs penetrate the lungs through inhalation, reach different body organs via the blood circulatory system [51], and upregulate the inflammatory proteins (MIP and MCP) and genes of MHC class I via Th2-mediated pathway [62]. The IFN- γ is preferably released from Th1 cells and induces NP-triggered cellular immune response along with ROS production in macrophages. They also elicit the expression of GTP-cyclohydrolase I (GCH-I) enzymes, which lead to formation of neopterin, and of indoleamine 2,3-dioxygenase (IDO) (first step is catalyzing enzyme in tryptophan breakdown by kynurenine pathway). The intratracheal exposure of TiO₂ NPs in mouse may result in their substantial accumulation in lungs, causing bleeding and inflammation [34, 63]. The mutagenic potential of TiO₂ NPs has been revealed by the treatment of pUC19/lacZ⁻ plasmid with different concentrations of TiO₂ NPs (average size 30.6 nm) and subsequent transfection of CaCl₂-induced competent DH5 α cells, which showed loss of transfection efficacy of the plasmid in comparison to untreated ones [64].

In a cytoplasmic proteome study involving human monocyte-derived macrophages, the abundancies of chloride intracellular channel protein 1, cathepsin D, and lysine acetylation were observed after exposure to nTiO₂ [40]. Recently, Sheng et al. [65] have demonstrated the significant alterations in the expressions of 1041 genes involved in different types of processes, including immune/inflammatory responses, apoptosis, oxidative stress, stress responses, metabolic processes, ion transport, signal transduction, and cell proliferation/division and translation, in mice spleen [65].

TiO₂ also caused lung cancer in rats after oral administration of 160 and 33 nm particles at doses of 40, 200, and 1000 mg/kg body weight [4]. The ultrafine TiO₂ (UF-TiO₂), less than 100 nm in diameter, induced pulmonary fibrosis, lung tumor, and genotoxicity in rats [66, 67]. Similarly, the NMs may also cause damage to liver cells during cleansing of toxins and pollutants in body. Furthermore, the TiO₂ NPs may cause hepatotoxicity in human hepatocellular carcinoma cell line (SMMC-7721), human liver cell line (HL-7702), rat hepatocarcinoma cell line (CBRH-7919), and rat liver cell line (BRL-3A), which may be associated with changes in cell morphology, increased intercellular ROS production, and decreased GSH levels at 0.1–100 µg/mL [13].

3.7. Aquatic Nanotoxicity. The in vitro studies have raised concerns about the toxicity of TiO₂ NPs in mammalian, but

there are limited data on ecotoxicity to aquatic organisms. The heaping of NPs to sewage increases due to their excessive use in industry and commerce [68]. The engineered nanoparticles (ENPs) intermingle with various toxins, including metals in sediments and water phase, making agglomerates and residues [69], and causing damage to aquatic organisms [55]. The exposure of adult zebra fish to 1.0 mg/L TiO₂ (both NP and bulk) for 21 days has been shown to lower the number of viable embryos [70] and inhibit the growth of goldfish (*Carassius auratus*) [71]. Similarly, the exposure of nTiO₂ suspensions (100 and 200 mg/L) to carp (*Cyprinus carpio*) may cause a decrease in SOD, CAT, and POD, while inducing a significant increase in LPO levels in the liver [72]. The combined exposure of anatase and rutile NPs to freshwater microalgae, *Chlorella* sp., at 0.25, 0.5, and 1 mg/L under UV irradiations has been demonstrated to reduce the cell viability and chlorophyll content [22]. TiO₂ has also adverse impacts on the survival, growth, and reproduction of *D. magna*. It has been determined that exposure of anatase (21 nm) particles is more toxic to *D. magna* as compared to anatase (250 nm) and rutile (500 nm) particles [73]. Therefore, the study of adverse effects of various NMs on aquatic species is necessary to assess their potential environmental hazardous effects.

4. Interactions of NPs in Ecosystem

The clean air is not only of scientific, environmental, and physiological importance but a basic need for living a healthy life. The chemicals and biological attacks may pose risk to human health and environment [74]. In this regard, the dangers of NPs to human health and environment have increased due to the prompt growth in nanotechnology. The adsorption of noxious pollutants on NPs has been extensively studied. In environment, the NPs always amalgamate with other pollutants. The interactions between conventional pollutants with NPs and their impact on environmental components are little considered. The heaping of NPs to sewage increases due to their excessive use in industry and commerce [68]. The chance of association of organic materials, including toxicants, increases with the aggregation of NPs in water. Hence, the bioavailability of these materials is altered. Thus, extra toxicological concerns are needed in presence of NPs [75].

The workers involved in the production of TiO₂ NPs may have significant risk on cytotoxicity response at relatively high airborne concentrations of anatase TiO₂ NPs [76]. Widespread use of nTiO₂ may intensify the threat of combined exposure of nTiO₂ with other environmental pollutants. The mixing of different compounds may bring astonishing toxic effects, even if the toxicities of the individual compounds are well known. For example, when bisphenol A (BPA) combines with nTiO₂, it facilitates the movement of nTiO₂ into exposed cells, causing synergistic toxicity by oxidative stress, inducing DNA double-strand breaks and micronuclei formation [77]. The growth inhibition of fresh water algae (*Pseudokirchneriella subcapitata*) was increased by the interaction of Cd(II) species with TiO₂ [78]. Similarly, the adsorption of Cd(II) onto nTiO₂ was enhanced by coating humic acid (HA) on nTiO₂ [79]. The anatase NPs are superior sorbents than activated carbon and other metal oxide NPs

[80]. The TiO₂ and Al₂O₃ NPs enter the Chinese hamster ovary (CHO-K1) cells through endocytosis and attack on lysosomal and mitochondrial activities, thus causing cytotoxicity and genotoxicity as well as a decrease in cell viability [54].

The hydroxylated fullerenes/C60 (OH) 24 exert synergistic stimulative effect on genes related to circadian rhythm, vesicular transport, kinases, and immune responses in zebrafish embryos [81], while the presence of nitrite with TiO₂ enhances the induction of apoptosis-related genes via NO signaling pathway [48].

5. Chemical Perspective

From chemical perspective, TiO₂ NPs show phototoxic effects upon UVA irradiations. Upon photon energy absorption, the electrons of the NPs jump from valence band to the conduction band, leaving the valence band holes. Hydroxyl radicals (*OH) are produced when valence band holes take electrons from water or hydroxyl ions and other ROS such as singlet oxygen (¹O₂) and superoxide (*O₂⁻) are also produced by different mechanisms. Free radicals (*OH and carbon centered free radicals) are also generated in dark. The generated ROS may be genotoxic or cytotoxic, affecting cell viability (Figure 3). Hence, TiO₂ NPs are toxic to living system both in the presence and absence of light via generation of free radicals [2].

6. Effect of Exposure Time and Dose on Toxicity of TiO₂ NPs

The primary particle size (the size of particle at the time of injection) of TiO₂ NPs is not as important as that of secondary particle size (the size of particle after agglomeration) for in vivo toxicity. Likewise, the physicochemical characteristics and time of exposure of NPs before the toxicological study are important [82]. The dietary exposure of nTiO₂ for 3 or 14 days may cause hazards to the terrestrial invertebrates [83]. Intratracheal instillation to rats with 0.5, 5, or 50 mg/kg of 5, 21, and 50 nm TiO₂ primary particles, respectively, has been demonstrated to exhibit dose-dependent toxic responses. In the same way, intraperitoneal injection of TiO₂ NPs (5 mg/kg) for 14 days did not have considerable effect on mouse kidney and the nephric dysfunction; however at doses of 50, 100, and 150 mg/kg body weight, it significantly induced inflammatory response and abnormal functions of kidney in mice.

Short-term exposure of TiO₂ NPs may have low-to-medium ecological hazards on zebrafish [23]. Nano-TiO₂ exposure for 3 h causes highest production of ROS in cytoplasm while at 24 h exposure ROS is only produced in perinuclear region due to aggregation [35].

Nano-TiO₂ accumulation occurs around the nucleus for up to 25 days in retinal pigment epithelial cells after a single low-level long-term exposure [2]. The cytotoxicity in normal liver and carcinomatous liver cells of either rat or human increases as the time of exposure increases, even a low concentration of nTiO₂ may induce higher toxicity with increase in time of exposure [13]. In long-term exposure, TiO₂ NPs

may cause pronounced adverse effect (growth inhibition and loss in liver weight) on zebrafish in time- and dose-dependent manner *in vivo*. It has also been shown that TiO₂ NPs exposure for 6 months to zebrafish may elicit pronounced toxic consequences like organ injury, behavior alterations, mortality, and organ distribution at higher concentration [23]. Furthermore, at long-term exposure, TiO₂ accumulates in the cell and causes toxic effects which are not evident at short-term exposure [84]. Several cell lines exposed to higher concentrations (100 µg/mL of TiO₂) may exhibit morphological changes such as cell shrinkage or nuclear condensation [35]. The exposure of differentiated murine J774.2 macrophages to 1 µg/mL concentration may have no considerable effects on cell proliferation, while at concentration 10 µg/mL it may exhibit significant cytotoxic effects [12]. Unnithan and colleagues have shown that fine nano-TiO₂ (~20 nm) at 40 mg/kg cause biochemical perturbations in Wistar rats [85]. Conclusively, the NPs even at their non-cytotoxic doses may have pathophysiological concerns [28].

7. Effect of Size and Shape on Toxicity of TiO₂ NPs

The major physicochemical properties to evaluate the toxicity are size, shape, surface area, phase, composition, coating, nature of surface, and agglomeration of NPs [16, 86]. The size and surface area of NPs may be responsible for their toxicity, but most of the studies do not reveal the relationship between physiochemical characteristics of NPs and their toxicity [82]. For example, 25 nm anatase and 31 nm anatase/rutile show greater phototoxicity than 142 nm anatase and 214 nm rutile NPs [2]. All the sizes and crystal forms (anatase and rutile) of TiO₂ NPs exert toxic (phototoxic) effects on human skin keratinocytes under UVA irradiations in a dose-dependent way. The smaller size nTiO₂ may cause greater cytotoxicity than larger size NPs, and anatase form may show more phototoxicity than rutile [8, 84]. Furthermore, the NPs (rod and sphere) of smaller size show higher toxicity than larger particles. Moreover, the nanorods exhibit more toxicity than spherical particles having the same size and surface area, showing the contribution of shape toward cytotoxicity [16]. The Ag (20 and 200 nm) and TiO₂ (21 nm) NPs are significantly taken up by human epithelial, hepatic, and undifferentiated monocyte cells, resulting in decline of metabolic activation and cell death enhancement [87].

8. Conclusion and Future Perspectives

Concerning the biosafety of nanotechnology, nanotoxicity is going to be the second most priority of nanotechnology. The different responses toward the NPs in ecosystem may be very complex and diverse, involving a variety of parameters, demonstrating their difficult environmental fate [88]. In addition, the environmental hazards of ENPs can be documented by knowing their behavior and fate in the natural aquatic system [89].

To date no product (medicinal or food stuff) is available with 100 percent purity and efficiency, but for the safer use of

nanosized particles with no or minimal hazardous effects on environment, the detailed understanding about their sources, interactions with environment, biodegradability, and possible risk assessment are utmost requirement prior to use. In addition, the interactions of NPs with biological molecules and their adverse effects need to be fully understood prior to their approval in clinical trials.

The cellular responses and toxicity produced by TiO₂ NPs depend on the surface/mass ratio, purity, crystallinity, surface reactivity, adsorbed groups, coatings, solubility, shape, size [7, 54], zeta potential, and dispersion or propensity to agglomerate or aggregate in different media [90]. These parameters need to be considered for the safer use of NMs. The undefined health and environmental features of TiO₂ NPs due to its widespread use are necessary to be managed by a systematic, coherent, and tested foundation. Therefore, the regulatory health risk assessment of such particles may be mandatory for the safe use of NMs in consumer products and medicines, including the potential effects on reproduction and fertility.

Abbreviations

NMs:	Nanomaterials
NPs:	Nanoparticles
TiO ₂ NPs:	Titanium dioxide NPs
LD ₅₀ :	Lethal dose at 50% concentration
FDA:	Food and Drug Administration
EPA:	Environmental Protection Agency
nTiO ₂ :	Nano-TiO ₂
SCF:	European Commission's Scientific Committee on Food
JECFA:	Joint Expert Committee on Food Additives of the Food and Agriculture Organization/World Health Organization
EFSA:	European Food Safety Authority
MSDS:	Material Safety Data Sheets
WHO:	World Health Organization
SCCS:	Scientific Committee on Consumer Safety
ROS:	Reactive oxygen species
HSP:	Heat shock proteins
H ₂ O ₂ :	Hydrogen peroxide
SOD:	Superoxide dismutase
CAT:	Catalase
GPx:	Glutathione peroxidase
GST:	Glutathione S epoxide transferase
GR:	Glutathione reductase
NETs:	Neutrophils extracellular traps
TGF-β:	Transforming growth factor-β
TNF-α:	Tumor necrosis factor-α
IFN-γ:	Interferon-γ
MAPK:	Mitogen-activated protein kinase
AIF:	Apoptosis-inducing factor
BBB:	Blood brain barrier
IDO:	Indoleamine 2,3-dioxygenase
UF-TiO ₂ :	Ultrafine TiO ₂
ENPs:	Engineered nanoparticles
BPA:	Bisphenol A
HA:	Humic acid
CHO-K1:	Chinese hamster ovary

- OH: Hydroxyl radicals
- ¹O₂: Singlet oxygen
- O₂⁻: Superoxide.

Competing Interests

The authors declare no competing financial interests.

Acknowledgments

The authors thank all the researchers who contributed to their current understanding of hazardous effects of TiO₂ NPs.

References

- [1] D. M. Gonçalves and D. Girard, "Titanium dioxide (TiO₂) nanoparticles induce neutrophil influx and local production of several pro-inflammatory mediators in vivo," *International Immunopharmacology*, vol. 11, no. 8, pp. 1109–1115, 2011.
- [2] K. Sanders, L. L. Degen, W. R. Mundy et al., "In vitro phototoxicity and hazard identification of nano-scale titanium dioxide," *Toxicology and Applied Pharmacology*, vol. 258, no. 2, pp. 226–236, 2012.
- [3] K. Khosravi, M. E. Hoque, B. Dimock, H. Hintelmann, and C. D. Metcalfe, "A novel approach for determining total titanium from titanium dioxide nanoparticles suspended in water and biosolids by digestion with ammonium persulfate," *Analytica Chimica Acta*, vol. 713, pp. 86–91, 2012.
- [4] L. P. Sycheva, V. S. Zhurkov, V. V. Iurchenko et al., "Investigation of genotoxic and cytotoxic effects of micro- and nanosized titanium dioxide in six organs of mice in vivo," *Mutation Research/Genetic Toxicology and Environmental Mutagenesis*, vol. 726, no. 1, pp. 8–14, 2011.
- [5] D. M. Gonçalves, S. Chiasson, and D. Girard, "Activation of human neutrophils by titanium dioxide (TiO₂) nanoparticles," *Toxicology in Vitro*, vol. 24, no. 3, pp. 1002–1008, 2010.
- [6] B. Li, R. Hu, Z. Cheng et al., "Titanium dioxide nanoparticles relieve biochemical dysfunctions of fifth-instar larvae of silkworms following exposure to phoxim insecticide," *Chemosphere*, vol. 89, no. 5, pp. 609–614, 2012.
- [7] S. J. Kang, B. M. Kim, Y. J. Lee, S. H. Hong, and H. W. Chung, "Titanium dioxide nanoparticles induce apoptosis through the JNK/p38-caspase-8-Bid pathway in phytohemagglutinin-stimulated human lymphocytes," *Biochemical and Biophysical Research Communications*, vol. 386, no. 4, pp. 682–687, 2009.
- [8] J.-J. Yin, J. Liu, M. Ehrenshaft et al., "Phototoxicity of nano titanium dioxides in HaCaT keratinocytes—generation of reactive oxygen species and cell damage," *Toxicology and Applied Pharmacology*, vol. 263, no. 1, pp. 81–88, 2012.
- [9] R. Zhang, Y. Niu, Y. Li et al., "Acute toxicity study of the interaction between titanium dioxide nanoparticles and lead acetate in mice," *Environmental Toxicology and Pharmacology*, vol. 30, no. 1, pp. 52–60, 2010.
- [10] B. Jovanović and D. Palić, "Immunotoxicology of non-functionalized engineered nanoparticles in aquatic organisms with special emphasis on fish—review of current knowledge, gap identification, and call for further research," *Aquatic Toxicology*, vol. 118–119, pp. 141–151, 2012.
- [11] N. A. Philbrook, L. M. Winn, A. R. M. N. Afroz, N. B. Saleh, and V. K. Walker, "The effect of TiO₂ and Ag nanoparticles on reproduction and development of *Drosophila melanogaster* and CD-1 mice," *Toxicology and Applied Pharmacology*, vol. 257, no. 3, pp. 429–436, 2011.
- [12] F. Martínez-Gutiérrez, E. P. Thi, J. M. Silverman et al., "Antibacterial activity, inflammatory response, coagulation and cytotoxicity effects of silver nanoparticles," *Nanomedicine: Nanotechnology, Biology, and Medicine*, vol. 8, no. 3, pp. 328–336, 2012.
- [13] B. Sha, W. Gao, S. Wang, F. Xu, and T. Lu, "Cytotoxicity of titanium dioxide nanoparticles differs in four liver cells from human and rat," *Composites Part B: Engineering*, vol. 42, no. 8, pp. 2136–2144, 2011.
- [14] A. Markowska-Szczupak, K. Ulfig, and A. W. Morawski, "The application of titanium dioxide for deactivation of bioparticulates: an overview," *Catalysis Today*, vol. 169, no. 1, pp. 249–257, 2011.
- [15] S. Mohanty, S. Mishra, P. Jena, B. Jacob, B. Sarkar, and A. Sonawane, "An investigation on the antibacterial, cytotoxic, and antibiofilm efficacy of starch-stabilized silver nanoparticles," *Nanomedicine: Nanotechnology, Biology, and Medicine*, vol. 8, no. 6, pp. 916–924, 2012.
- [16] I.-L. Hsiao and Y.-J. Huang, "Effects of various physicochemical characteristics on the toxicities of ZnO and TiO₂ nanoparticles toward human lung epithelial cells," *Science of the Total Environment*, vol. 409, no. 7, pp. 1219–1228, 2011.
- [17] M. A. Oosthuizen, H. M. Oberholzer, M. R. Scriba, W. J. van der Spuy, and E. Pretorius, "Evaluation of the morphological changes in the lungs of BALB/c mice after inhalation of spherical and rod-shaped titanium nanoparticles," *Micron*, vol. 43, no. 8, pp. 863–869, 2012.
- [18] I. Bhatt and B. N. Tripathi, "Interaction of engineered nanoparticles with various components of the environment and possible strategies for their risk assessment," *Chemosphere*, vol. 82, no. 3, pp. 308–317, 2011.
- [19] Y. Gao, N. V. Gopee, P. C. Howard, and L.-R. Yu, "Proteomic analysis of early response lymph node proteins in mice treated with titanium dioxide nanoparticles," *Journal of Proteomics*, vol. 74, no. 12, pp. 2745–2759, 2011.
- [20] S. Jomini, H. Clivot, P. Bauda, and C. Pagnout, "Impact of manufactured TiO₂ nanoparticles on planktonic and sessile bacterial communities," *Environmental Pollution*, vol. 202, pp. 196–204, 2015.
- [21] J. Wu, J. Sun, and Y. Xue, "Involvement of JNK and P53 activation in G2/M cell cycle arrest and apoptosis induced by titanium dioxide nanoparticles in neuron cells," *Toxicology Letters*, vol. 199, no. 3, pp. 269–276, 2010.
- [22] V. Iswarya, M. Bhuvaneshwari, S. A. Alex et al., "Combined toxicity of two crystalline phases (anatase and rutile) of Titania nanoparticles towards freshwater microalgae: *Chlorella* sp," *Aquatic Toxicology*, vol. 161, pp. 154–169, 2015.
- [23] J. Chen, X. Dong, Y. Xin, and M. Zhao, "Effects of titanium dioxide nanoparticles on growth and some histological parameters of zebrafish (*Danio rerio*) after a long-term exposure," *Aquatic Toxicology*, vol. 101, no. 3–4, pp. 493–499, 2011.
- [24] S. Gui, Z. Zhang, L. Zheng et al., "Molecular mechanism of kidney injury of mice caused by exposure to titanium dioxide nanoparticles," *Journal of Hazardous Materials*, vol. 195, pp. 365–370, 2011.
- [25] J. Wang, G. Zhou, C. Chen et al., "Acute toxicity and biodistribution of different sized titanium dioxide particles in mice after oral administration," *Toxicology Letters*, vol. 168, no. 2, pp. 176–185, 2007.

- [26] Y. C. Hong, C. U. Bang, D. H. Shin, and H. S. Uhm, "Band gap narrowing of TiO₂ by nitrogen doping in atmospheric microwave plasma," *Chemical Physics Letters*, vol. 413, no. 4–6, pp. 454–457, 2005.
- [27] B. K. Bernard, M. R. Osheroff, A. Hofmann, and J. H. Mennear, "Toxicology and carcinogenesis studies of dietary titanium dioxide-coated mica in male and female Fischer 344 rats," *Journal of Toxicology and Environmental Health*, vol. 29, no. 4, pp. 417–429, 1990.
- [28] S. Hussain, S. Boland, A. Baeza-Squiban et al., "Oxidative stress and proinflammatory effects of carbon black and titanium dioxide nanoparticles: role of particle surface area and internalized amount," *Toxicology*, vol. 260, no. 1–3, pp. 142–149, 2009.
- [29] D. B. Warheit, R. A. Hoke, C. Finlay, E. M. Donner, K. L. Reed, and C. M. Sayes, "Development of a base set of toxicity tests using ultrafine TiO₂ particles as a component of nanoparticle risk management," *Toxicology Letters*, vol. 171, no. 3, pp. 99–110, 2007.
- [30] I. Iavicoli, V. Leso, L. Fontana, and A. Bergamaschi, "Toxicological effects of titanium dioxide nanoparticles: a review of in vitro mammalian studies," *European Review for Medical and Pharmacological Sciences*, vol. 15, no. 5, pp. 481–508, 2011.
- [31] I. Iavicoli, V. Leso, and A. Bergamaschi, "Toxicological effects of titanium dioxide nanoparticles: a review of in vivo studies," *Journal of Nanomaterials*, vol. 2012, Article ID 964381, 36 pages, 2012.
- [32] J. Chen, X. Dong, J. Zhao, and G. Tang, "In vivo acute toxicity of titanium dioxide nanoparticles to mice after intraperitoneal injection," *Journal of Applied Toxicology*, vol. 29, no. 4, pp. 330–337, 2009.
- [33] R. K. Shukla, V. Sharma, A. K. Pandey, S. Singh, S. Sultana, and A. Dhawan, "ROS-mediated genotoxicity induced by titanium dioxide nanoparticles in human epidermal cells," *Toxicology in Vitro*, vol. 25, no. 1, pp. 231–241, 2011.
- [34] Q. Sun, D. Tan, Y. Ze et al., "Pulmototoxicological effects caused by long-term titanium dioxide nanoparticles exposure in mice," *Journal of Hazardous Materials*, vol. 235–236, pp. 47–53, 2012.
- [35] E.-J. Park, J. Yi, K.-H. Chung, D.-Y. Ryu, J. Choi, and K. Park, "Oxidative stress and apoptosis induced by titanium dioxide nanoparticles in cultured BEAS-2B cells," *Toxicology Letters*, vol. 180, no. 3, pp. 222–229, 2008.
- [36] Y. Ze, L. Sheng, X. Zhao et al., "TiO₂ nanoparticles induced hippocampal neuroinflammation in mice," *PLoS One*, vol. 9, no. 3, Article ID e92230, 2014.
- [37] Y. Shi, F. Wang, J. He, S. Yadav, and H. Wang, "Titanium dioxide nanoparticles cause apoptosis in BEAS-2B cells through the caspase 8/t-Bid-independent mitochondrial pathway," *Toxicology Letters*, vol. 196, no. 1, pp. 21–27, 2010.
- [38] K. W. Ng, S. P. K. Khoo, B. C. Heng et al., "The role of the tumor suppressor p53 pathway in the cellular DNA damage response to zinc oxide nanoparticles," *Biomaterials*, vol. 32, no. 32, pp. 8218–8225, 2011.
- [39] C. Migdal, R. Rahal, A. Rubod et al., "Internalisation of hybrid titanium dioxide/para-amino benzoic acid nanoparticles in human dendritic cells did not induce toxicity and changes in their functions," *Toxicology Letters*, vol. 199, no. 1, pp. 34–42, 2010.
- [40] J. Sund, J. Palomäki, N. Ahonen, K. Savolainen, H. Alenius, and A. Puustinen, "Phagocytosis of nano-sized titanium dioxide triggers changes in protein acetylation," *Journal of Proteomics*, vol. 108, pp. 469–483, 2014.
- [41] A. Zhu, K. Sun, and H. R. Petty, "Titanium doping reduces superoxide dismutase activity, but not oxidase activity, of catalytic CeO₂ nanoparticles," *Inorganic Chemistry Communications*, vol. 15, pp. 235–237, 2012.
- [42] X. Zhao, L. Sheng, L. Wang et al., "Mechanisms of nanosized titanium dioxide-induced testicular oxidative stress and apoptosis in male mice," *Particle and Fibre Toxicology*, vol. 11, article 47, 2014.
- [43] B. Jovanović, L. Anastasova, E. W. Rowe, Y. Zhang, A. R. Clapp, and D. Palić, "Effects of nanosized titanium dioxide on innate immune system of fathead minnow (*Pimephales promelas* Rafinesque, 1820)," *Ecotoxicology and Environmental Safety*, vol. 74, no. 4, pp. 675–683, 2011.
- [44] Q. Remijsen, T. W. Kuijpers, E. Wirawan, S. Lippens, P. Vandenaabee, and T. Vanden Berghe, "Dying for a cause: NETosis, mechanisms behind an antimicrobial cell death modality," *Cell Death and Differentiation*, vol. 18, no. 4, pp. 581–588, 2011.
- [45] M. A. Mesa and G. Vasquez, "NETosis," *Autoimmune Diseases*, vol. 2013, Article ID 651497, 7 pages, 2013.
- [46] ChemIDplus, *ChemIDplus Advanced*, Search Terms: Titanium Dioxide; CAS Reg. No. 13463-67-7, U.S. National Library of Medicine, National Institutes of Health, Department of Health and Human Services, 2005, <http://chem.sis.nlm.nih.gov/chemidplus/>.
- [47] R. Hu, L. Zheng, T. Zhang et al., "Molecular mechanism of hippocampal apoptosis of mice following exposure to titanium dioxide nanoparticles," *Journal of Hazardous Materials*, vol. 191, no. 1–3, pp. 32–40, 2011.
- [48] M. Tu, Y. Huang, H.-L. Li, and Z.-H. Gao, "The stress caused by nitrite with titanium dioxide nanoparticles under UVA irradiation in human keratinocyte cell," *Toxicology*, vol. 299, no. 1, pp. 60–68, 2012.
- [49] G. Paterson, J. M. Ataria, M. E. Hoque, D. C. Burns, and C. D. Metcalfe, "The toxicity of titanium dioxide nanopowder to early life stages of the Japanese medaka (*Oryzias latipes*)," *Chemosphere*, vol. 82, no. 7, pp. 1002–1009, 2011.
- [50] Z. Chen, Y. Wang, T. Ba et al., "Genotoxic evaluation of titanium dioxide nanoparticles in vivo and in vitro," *Toxicology Letters*, vol. 226, no. 3, pp. 314–319, 2014.
- [51] Q. Saquib, A. A. Al-Khedhairi, M. A. Siddiqui, F. M. Abou-Tarboush, A. Azam, and J. Musarrat, "Titanium dioxide nanoparticles induced cytotoxicity, oxidative stress and DNA damage in human amnion epithelial (WISH) cells," *Toxicology in Vitro*, vol. 26, no. 2, pp. 351–361, 2012.
- [52] B. Trouiller, R. Reliene, A. Westbrook, P. Solaimani, and R. H. Schiestl, "Titanium dioxide nanoparticles induce DNA damage and genetic instability in vivo in mice," *Cancer Research*, vol. 69, no. 22, pp. 8784–8789, 2009.
- [53] V. Freyre-Fonseca, N. L. Delgado-Buenrostro, E. B. Gutiérrez-Cirlos et al., "Titanium dioxide nanoparticles impair lung mitochondrial function," *Toxicology Letters*, vol. 202, no. 2, pp. 111–119, 2011.
- [54] A. L. Di Virgilio, M. Reigosa, P. M. Arnal, and M. Fernández Lorenzo de Mele, "Comparative study of the cytotoxic and genotoxic effects of titanium oxide and aluminium oxide nanoparticles in Chinese hamster ovary (CHO-K1) cells," *Journal of Hazardous Materials*, vol. 177, no. 1–3, pp. 711–718, 2010.
- [55] M. Ghosh, M. Bandyopadhyay, and A. Mukherjee, "Genotoxicity of titanium dioxide (TiO₂) nanoparticles at two trophic levels: plant and human lymphocytes," *Chemosphere*, vol. 81, no. 10, pp. 1253–1262, 2010.

- [56] G. Janer, E. Mas del Molino, E. Fernández-Rosas, A. Fernández, and S. Vázquez-Campos, "Cell uptake and oral absorption of titanium dioxide nanoparticles," *Toxicology Letters*, vol. 228, no. 2, pp. 103–110, 2014.
- [57] E. Fröhlich and E. Roblegg, "Models for oral uptake of nanoparticles in consumer products," *Toxicology*, vol. 291, no. 1–3, pp. 10–17, 2012.
- [58] J. Valant, D. Drobne, and S. Novak, "Effect of ingested titanium dioxide nanoparticles on the digestive gland cell membrane of terrestrial isopods," *Chemosphere*, vol. 87, no. 1, pp. 19–25, 2012.
- [59] E. Brun, M. Carrière, and A. Mabondzo, "In vitro evidence of dysregulation of blood-brain barrier function after acute and repeated/long-term exposure to TiO₂ nanoparticles," *Biomaterials*, vol. 33, no. 3, pp. 886–896, 2012.
- [60] E. Huerta-García, J. A. Pérez-Arizti, S. G. Márquez-Ramírez et al., "Titanium dioxide nanoparticles induce strong oxidative stress and mitochondrial damage in glial cells," *Free Radical Biology and Medicine*, vol. 73, pp. 84–94, 2014.
- [61] M. Naya, N. Kobayashi, M. Ema et al., "In vivo genotoxicity study of titanium dioxide nanoparticles using comet assay following intratracheal instillation in rats," *Regulatory Toxicology and Pharmacology*, vol. 62, no. 1, pp. 1–6, 2012.
- [62] E.-J. Park, J. Yoon, K. Choi, J. Yi, and K. Park, "Induction of chronic inflammation in mice treated with titanium dioxide nanoparticles by intratracheal instillation," *Toxicology*, vol. 260, no. 1–3, pp. 37–46, 2009.
- [63] S. Makumire, V. S. K. Chakravadhanula, G. Köllisch, E. Redel, and A. Shonhai, "Immunomodulatory activity of zinc peroxide (ZnO₂) and titanium dioxide (TiO₂) nanoparticles and their effects on DNA and protein integrity," *Toxicology Letters*, vol. 227, no. 1, pp. 56–64, 2014.
- [64] J. Ahmad, S. Dwivedi, S. Alarifi, A. A. Al-Khedhairi, and J. Musarrat, "Use of β -galactosidase (lacZ) gene α -complementation as a novel approach for assessment of titanium oxide nanoparticles induced mutagenesis," *Mutation Research/Genetic Toxicology and Environmental Mutagenesis*, vol. 747, no. 2, pp. 246–252, 2012.
- [65] L. Sheng, L. Wang, X. Sang et al., "Nano-sized titanium dioxide-induced splenic toxicity: a biological pathway explored using microarray technology," *Journal of Hazardous Materials*, vol. 278, pp. 180–188, 2014.
- [66] J. J. Wang, B. J. S. Sanderson, and H. Wang, "Cyto- and genotoxicity of ultrafine TiO₂ particles in cultured human lymphoblastoid cells," *Mutation Research/Genetic Toxicology and Environmental Mutagenesis*, vol. 628, no. 2, pp. 99–106, 2007.
- [67] D. B. Warheit, C. M. Sayes, K. L. Reed, and K. A. Swain, "Health effects related to nanoparticle exposures: environmental, health and safety considerations for assessing hazards and risks," *Pharmacology and Therapeutics*, vol. 120, no. 1, pp. 35–42, 2008.
- [68] Y. Wang, P. Westerhoff, and K. D. Hristovski, "Fate and biological effects of silver, titanium dioxide, and C₆₀ (fullerene) nanomaterials during simulated wastewater treatment processes," *Journal of Hazardous Materials*, vol. 201–202, pp. 16–22, 2012.
- [69] N. B. Hartmann, S. Legros, F. Von der Kammer, T. Hofmann, and A. Baun, "The potential of TiO₂ nanoparticles as carriers for cadmium uptake in *Lumbriculus variegatus* and *Daphnia magna*," *Aquatic Toxicology*, vol. 118–119, pp. 1–8, 2012.
- [70] C. S. Ramsden, T. B. Henry, and R. D. Handy, "Sub-lethal effects of titanium dioxide nanoparticles on the physiology and reproduction of zebrafish," *Aquatic Toxicology*, vol. 126, pp. 404–413, 2013.
- [71] M. Ates, V. Demir, R. Adiguzel, and Z. Arslan, "Bioaccumulation, subacute toxicity, and tissue distribution of engineered titanium dioxide nanoparticles in goldfish (*Carassius auratus*)," *Journal of Nanomaterials*, vol. 2013, Article ID 460518, 6 pages, 2013.
- [72] L. Hao, Z. Wang, and B. Xing, "Effect of sub-acute exposure to TiO₂ nanoparticles on oxidative stress and histopathological changes in Juvenile Carp (*Cyprinus carpio*)," *Journal of Environmental Sciences*, vol. 21, no. 10, pp. 1459–1466, 2009.
- [73] S. H. Bang, T.-H. Le, S. K. Lee, P. Kim, J. S. Kim, and J. Min, "Toxicity assessment of titanium (IV) oxide nanoparticles using *Daphnia magna* (Water Flea)," *Environmental Health and Toxicology*, vol. 26, Article ID e2011002, 2011.
- [74] C. Srisitthirathkul, V. Pongsorrarith, and N. Intasanta, "The potential use of nanosilver-decorated titanium dioxide nanofibers for toxin decomposition with antimicrobial and self-cleaning properties," *Applied Surface Science*, vol. 257, no. 21, pp. 8850–8856, 2011.
- [75] R. Govindasamy and A. A. Rahuman, "Histopathological studies and oxidative stress of synthesized silver nanoparticles in Mozambique tilapia (*Oreochromis mossambicus*)," *Journal of Environmental Sciences (China)*, vol. 24, no. 6, pp. 1091–1098, 2012.
- [76] C.-M. Liao, Y.-H. Chiang, and C.-P. Chio, "Assessing the airborne titanium dioxide nanoparticle-related exposure hazard at workplace," *Journal of Hazardous Materials*, vol. 162, pp. 57–65, 2009.
- [77] D. Zheng, N. Wang, X. Wang et al., "Effects of the interaction of TiO₂ nanoparticles with bisphenol A on their physicochemical properties and in vitro toxicity," *Journal of Hazardous Materials*, vol. 199–200, pp. 426–432, 2012.
- [78] N. B. Hartmann, F. Von der Kammer, T. Hofmann, M. Baalousha, S. Ottofuelling, and A. Baun, "Algal testing of titanium dioxide nanoparticles—testing considerations, inhibitory effects and modification of cadmium bioavailability," *Toxicology*, vol. 269, no. 2–3, pp. 190–197, 2010.
- [79] Q. Chen, D. Yin, S. Zhu, and X. Hu, "Adsorption of cadmium(II) on humic acid coated titanium dioxide," *Journal of Colloid and Interface Science*, vol. 367, no. 1, pp. 241–248, 2012.
- [80] J. Hu and H. J. Shipley, "Evaluation of desorption of Pb (II), Cu (II) and Zn (II) from titanium dioxide nanoparticles," *Science of the Total Environment*, vol. 431, pp. 209–220, 2012.
- [81] B. Jovanović, T. Ji, and D. Palić, "Gene expression of zebrafish embryos exposed to titanium dioxide nanoparticles and hydroxylated fullerenes," *Ecotoxicology and Environmental Safety*, vol. 74, no. 6, pp. 1518–1525, 2011.
- [82] A. Menard, D. Drobne, and A. Jemec, "Ecotoxicity of nanosized TiO₂. Review of in vivo data," *Environmental Pollution*, vol. 159, no. 3, pp. 677–684, 2011.
- [83] D. Drobne, A. Jemec, and Ž. Pipan Tkalec, "In vivo screening to determine hazards of nanoparticles: nanosized TiO₂," *Environmental Pollution*, vol. 157, no. 4, pp. 1157–1164, 2009.
- [84] G. Federici, B. J. Shaw, and R. D. Handy, "Toxicity of titanium dioxide nanoparticles to rainbow trout (*Oncorhynchus mykiss*): gill injury, oxidative stress, and other physiological effects," *Aquatic Toxicology*, vol. 84, no. 4, pp. 415–430, 2007.
- [85] J. Unnithan, M. U. Rehman, F. J. Ahmad, and M. Samim, "Concentration dependent toxicity of ~20 nm anatase titanium dioxide nanoparticles—an in vivo study on wistar rats," *Journal of Biomedical Nanotechnology*, vol. 7, no. 1, pp. 207–208, 2011.
- [86] R. Posgai, C. B. Cipolla-McCulloch, K. R. Murphy, S. M. Hussain, J. J. Rowe, and M. G. Nielsen, "Differential toxicity

- of silver and titanium dioxide nanoparticles on *Drosophila melanogaster* development, reproductive effort, and viability: size, coatings and antioxidants matter," *Chemosphere*, vol. 85, no. 1, pp. 34–42, 2011.
- [87] A. Lankoff, W. J. Sandberg, A. Wegierek-Ciuk et al., "The effect of agglomeration state of silver and titanium dioxide nanoparticles on cellular response of HepG2, A549 and THP-1 cells," *Toxicology Letters*, vol. 208, no. 3, pp. 197–213, 2012.
- [88] A. García, R. Espinosa, L. Delgado et al., "Acute toxicity of cerium oxide, titanium oxide and iron oxide nanoparticles using standardized tests," *Desalination*, vol. 269, no. 1–3, pp. 136–141, 2011.
- [89] F. von der Kammer, S. Ottofuelling, and T. Hofmann, "Assessment of the physico-chemical behavior of titanium dioxide nanoparticles in aquatic environments using multi-dimensional parameter testing," *Environmental Pollution*, vol. 158, no. 12, pp. 3472–3481, 2010.
- [90] N. Asare, C. Instanes, W. J. Sandberg et al., "Cytotoxic and genotoxic effects of silver nanoparticles in testicular cells," *Toxicology*, vol. 291, no. 1–3, pp. 65–72, 2012.